

COMENIUS UNIVERSITY IN BRATISLAVA  
FACULTY OF MATHEMATICS, PHYSICS AND INFORMATICS

**VISUALIZATION OF COMPLEX FUNCTION  
USING RIEMANN SURFACES**

DISSERTATION THESIS

BRATISLAVA 2014

RNDR. MIROSLAVA VALÍKOVÁ



COMENIUS UNIVERSITY IN BRATISLAVA  
FACULTY OF MATHEMATICS, PHYSICS  
AND INFORMATICS



# VISUALIZATION OF COMPLEX FUNCTION USING RIEMANN SURFACES

Dissertation Thesis

Branch of study: Geometry and Topology  
Study programme: 9.1.7. Geometry and Topology  
Department: Department of Algebra, Geometry  
and Didactics of Mathematics  
Supervisor: Doc. RNDr. Pavel Chalmovianský, PhD.



## ZADANIE ZÁVEREČNEJ PRÁCE

- Meno a priezvisko študenta:** RNDr. Miroslava Valíková  
**Študijný program:** geometria a topológia (Jednoodborové štúdium, doktorandské III. st., denná forma)  
**Študijný odbor:** 9.1.7. geometria a topológia  
**Typ záverečnej práce:** dizertačná  
**Jazyk záverečnej práce:** anglický  
**Sekundárny jazyk:** slovenský
- Názov:** Visualization of complex function using Riemann surfaces  
*Vizualizácia komplexných funkcií pomocou Riemannových plôch*
- Literatúra:** [1] T. Needham. Visual Complex Analysis. Oxford University Press Inc., New York, USA, 2000  
[2] G. A. Jones and D. Singerman. Complex functions: an algebraic and geometric viewpoint. Press Syndicate of the University of Cambridge, Great Britain, 1987  
[3] Otto Forster. Lectures on Riemann Surfaces (Graduate Texts in Mathematics). Springer, 1981
- Cieľ:** Cieľom práce je štúdium vlastností komplexných funkcií užitočných na vizualizáciu grafu takýchto funkcií. Použitím štruktúry singulárnych bodov sa vytvorí graf takejto funkcie pričom sa aplikujú poznatky z teórie Riemannových plôch. Rôzne existujúce aj nové metódy tvorby grafu sa porovnajú niekoľkými metrikami využívanými vo vizualizácii.
- Anotácia:** Práca sa zaoberá štúdiom vlastností grafov komplexných funkcií využiteľných pri vizualizácii takýchto funkcií. Naštudujeme pojem Riemannovej plochy a metódy vizualizácií mnoholístých funkcií. Poskytneme prehľad doterajších rozšírených techník používaných pri zobrazovaní mnoholístých funkcií. Opíšeme novú metódu vizualizácie viacerých typov jednohodnotových funkcií nad Riemannovou sférou, ktorú modifikujeme na zobrazovanie viachodnotových funkcií použitím vhodnej výškovej funkcie. Budeme sa zaoberať vylepšeniami algoritmu v podobe pridania vetviacej krivky do topológie mriežky a implementovania adaptívneho delenia. Získané prístupy a metódy porovnáme vo vhodných metrikách napr. pomocou maximálnej odchýlky, priemernej odchýlky a Hausdorffovej odchýlky grafu.
- Kľúčové slová:** Riemannove plochy, mnoholisté funkcie, vizualizácia, singulárne body
- Školiteľ:** doc. RNDr. Pavel Chalmovianský, PhD.  
**Katedra:** FMFI.KAGDM - Katedra algebry, geometrie a didaktiky matematiky  
**Vedúci katedry:** prof. RNDr. Pavol Zlatoš, PhD.
- Spôsob prístupnosti elektronickej verzie práce:**



85231370

Univerzita Komenského v Bratislave  
Fakulta matematiky, fyziky a informatiky

---

bez obmedzenia

**Dátum zadania:** 20.10.2010

**Dátum schválenia:** 20.10.2010

prof. RNDr. Július Korbaš, CSc.  
garant študijného programu

.....  
študent

.....  
školiť



## THESIS ASSIGNMENT

- Name and Surname:** RNDr. Miroslava Valíková  
**Study programme:** Geometry and Topology (Single degree study, Ph.D. III. deg., full time form)  
**Field of Study:** 9.1.7. Geometry And Topology  
**Type of Thesis:** Dissertation thesis  
**Language of Thesis:** English  
**Secondary language:** Slovak
- Title:** Visualization of complex function using Riemann surfaces
- Literature:** [1] T. Needham. Visual Complex Analysis. Oxford University Press Inc., New York, USA, 2000
- [2] G. A. Jones and D. Singerman. Complex functions: an algebraic and geometric viewpoint. Press Syndicate of the University of Cambridge, Great Britain, 1987
- [3] Otto Forster. Lectures on Riemann Surfaces (Graduate Texts in Mathematics). Springer, 1981
- Aim:** The goal is to study complex functions and their properties with respect to visualization of their graph. Using the structure of singular points a graph of the function is generated while the corresponding theory of Riemann surfaces is applied. Various up-to-date and novel methods are compared in several visualization oriented metrics.
- Annotation:** The work deals with properties of graphs of complex functions targeting on visualization of such functions. We study the notion of Riemann surface and methods of visualization of multi-valued function. We provide an up-to-date summary of techniques used to visualize multi-valued functions. We introduce a novel method of visualization of single-valued complex functions over Riemann sphere. A modification of this method is used to visualize a multi-valued functions using a well chosen height function. We improve the algorithm dealing with branch-cuts and an adaptive grid method. The gained results and methods are compared in appropriate metrics such as maximal error, average error and Hausdorff error.
- Keywords:** Riemann surfaces, multi-valued function, visualization, singular points
- Tutor:** doc. RNDr. Pavel Chalmovianský, PhD.  
**Department:** FMFI.KAGDM - Department of Algebra, Geometry and Didactics of Mathematics  
**Head of department:** prof. RNDr. Pavol Zlatoš, PhD.



Comenius University in Bratislava  
Faculty of Mathematics, Physics and Informatics

---

**Assigned:** 20.10.2010

**Approved:** 20.10.2010

prof. RNDr. Július Korbaš, CSc.  
Guarantor of Study Programme

.....  
Student

.....  
Tutor

## Acknowledgements

I would like to thank to doc. RNDr. Pavel Chalmovianský, PhD. for all his help and priceless advice he has given me throughout my studies, the research and also the writing period of this thesis.

Most of all I thank my husband and son for his support and patience.

RNDr. Miroslava Valíková

## Abstrakt

Práca sa zaoberá štúdiom grafov komplexných funkcií a ich vizualizáciou. Stručne opíšeme pojmy potrebné pri ďalšom štúdiu viacohodnotových funkcií. Podrobnejšie sa venujeme pojmu Riemannovej plochy a vizualizácie mnoholistej funkcie. Poskytneme prehľad rozšírených techník používaných pri zobrazovaní mnoholistých funkcií. Popíšeme nami navrhnutú metódu vizualizácie viacerých typov jednoduhodnotovej funkcie nad Riemannovou sférou, ktorá využíva absolútnu hodnotu funkcie na vyrátanie výškovej mapy a argument na priradenie farieb grafu. Túto metódu modifikujeme na zobrazovanie viacohodnotových funkcií využitím novej výškovej funkcie. Navrhujeme vylepšenie algoritmu v podobe pridania vetviacej krivky do topológie mriežky a implementovania adaptívneho delenia. Na záver porovnáme všetky metódy na základe maximálnej odchýlky, priemernej odchýlky a Hausdorffovej odchýlky grafu.

**Kľúčové slová:** Riemannove plochy, mnoholisté funkcie, vizualizácia, singulárne body.



## Abstract

The thesis is oriented on study of graphs of complex functions and their visualization. Basic notions and definitions on multi-valued function are described. To visualize a multi-valued function a notion of Riemann surface is often used. The thesis provides an summary of techniques used to visualize multi-valued functions. We give an overview of proposed method of visualizing chosen single-valued complex functions over Riemann sphere. The method uses the absolute value of a complex function to compute a height map and the argument to assign colors to the graph. This method is modified to visualize also multi-valued functions using a new height function. A branch-cut and an adaptive grid method were implemented to improve the visualization algorithm. The results were compared using maximal error, average error and Hausdorff error.

**Keywords:** Riemann surfaces, multi-valued function, visualization, singular points.

# Foreword

The thesis studies complex functions and methods of their visualizations, mainly the domain coloring and visualization using Riemann surfaces. Recent publications visualize the complex functions only on a part of their domain. Several published articles suggest an interest in solving the problem of visualizing of the complex function. Even though, there is still a space for development and improvement of existing methods.

The thesis is dedicated to a user interested in complex functions and their behaviors. The goal is to make it easier to understand the properties of the studied complex functions whose graph is natively placed in a four-dimensional space. This method is implemented in Blender, a modern graphical and visualization suite. Blender is an open-source, cross-platform software that allows a user to interact with created models. The visualization tool is written in Python, what gives to user the ability to adjust the proposed visualization method and add new features to it.

# Contents

<b>Foreword</b>	<b>iv</b>
<b>Introduction</b>	<b>1</b>
<b>1 Basic notions</b>	<b>4</b>
1.1 Complex numbers . . . . .	4
1.2 Möbius transformation . . . . .	6
1.3 Spherical splines . . . . .	11
<b>2 Riemann surfaces</b>	<b>16</b>
2.1 Definition of the Riemann surface . . . . .	16
2.2 Orientability of Riemann surfaces . . . . .	19
2.3 Meromorphic continuation and Riemann surfaces . . . . .	20
2.4 Examples . . . . .	25
2.5 The genus of a compact Riemann surface . . . . .	33
<b>3 Visualization methods</b>	<b>36</b>
3.1 Domain coloring . . . . .	36
3.2 Visualization of multi-valued functions . . . . .	50
3.3 Technical background of CoFiViS . . . . .	53
<b>4 Results</b>	<b>60</b>
4.1 CoFiViS . . . . .	60
4.2 Visualization of basic functions . . . . .	69
4.3 Other examined techniques of visualization . . . . .	80
4.4 Experimental results . . . . .	88
4.5 Visualization of the deformation of ADE singularities . . . . .	96

## CONTENTS

---

4.6 Discussion . . . . .	100
<b>Conclusion</b>	<b>103</b>
<b>References</b>	<b>105</b>

# List of Figures

1.1	Stereographic projection . . . . .	5
1.2	Example of Möbius transformation . . . . .	8
1.3	Complex inversion . . . . .	9
1.4	Classes of Möbius transformation . . . . .	10
1.5	Quadratic Bézier curve on sphere . . . . .	14
2.1	Biholomorphic map . . . . .	17
2.2	Sets of meromorphic continuation . . . . .	21
2.3	Meromorphic continuation along a path . . . . .	22
2.4	Homotopy . . . . .	23
2.5	The product of two paths . . . . .	24
2.6	The composition of two paths . . . . .	24
2.7	The half-planes used by the analytic continuation of logarithm . . . . .	26
2.8	Visualization of the copies of $E_n$ . . . . .	27
2.9	Example of the function element . . . . .	27
2.10	A cut-out of the Riemann surface of $\log z$ . . . . .	28
2.11	The Riemann surface of $f(z) = z^3$ . . . . .	29
2.12	The Riemann surface of $f(z) = \sqrt{z - a}$ . . . . .	30
2.13	The crossing of the layers of $f(z) = \sqrt{1 + \sqrt{z}}$ . . . . .	32
2.14	Image of the closed path $\gamma$ winding once around 0 transformed by $f(z) = \sqrt{1 + \sqrt{z}}$ . . . . .	32
2.15	Image of the closed path $\delta$ winding once around 1 but not around 0 transformed by $f(z) = \sqrt{1 + \sqrt{z}}$ . . . . .	33
2.16	Polygonal subdivision . . . . .	34

---

3.1	Exponential function . . . . .	37
3.2	The color scheme used by Farris . . . . .	37
3.3	Visualization of a polynomial function of degree six . . . . .	38
3.4	The visualization of a rational function . . . . .	39
3.5	The visualization of derivative of a rational function . . . . .	39
3.6	The domain coloring by Lundmark . . . . .	40
3.7	Monomial functions by Lundmark . . . . .	40
3.8	The visualization of a polynomial function . . . . .	41
3.9	Visualization of poles by Lundmark . . . . .	42
3.10	Möbius transformation by Lundmark . . . . .	43
3.11	Rational function . . . . .	43
3.12	The exponential function . . . . .	44
3.13	Logarithm function . . . . .	44
3.14	The complex sine function . . . . .	45
3.15	The domain coloring by [PP09] . . . . .	46
3.16	The coloring displayed on the Riemann sphere . . . . .	47
3.17	Visualization of the rational function . . . . .	48
3.18	Multiple zero and multiple pole . . . . .	49
3.19	Visualization of a polynomial function . . . . .	50
3.20	Multivalued functions . . . . .	51
3.21	Examples of the Riemann surfaces . . . . .	52
3.22	Riemann surface of $h(z) = \sqrt{z+1}\sqrt{z-1}$ . . . . .	52
3.23	Visualization of $f(z) = \arcsin(z)$ . . . . .	53
3.24	Star and chain of triangles . . . . .	54
3.25	Planar and non-planar tetragon . . . . .	55
3.26	Surface of revolution . . . . .	56
3.27	Interpolation of sphere using spherical coordinates . . . . .	56
3.28	RGB color space visualized on a cube. . . . .	57
3.29	HSV color space visualized on a cone. . . . .	57
4.1	Polyhedrons interpolating the sphere . . . . .	61
4.2	Material settings . . . . .	62

---

---

**LIST OF FIGURES**

4.3	Color scheme used to visualize the argument of the complex number $z$ . . . . .	63
4.4	Graph of $\arctan(z)$ . . . . .	64
4.5	The impact of the height function on the graph . . . . .	64
4.6	Graph of the root function without using Riemann surface . . . . .	65
4.7	Branch cut . . . . .	66
4.8	Visualization of identity . . . . .	70
4.9	Visualization of a monomial . . . . .	70
4.10	Visualization of $f(z) = (z - a)(z - b)$ . . . . .	72
4.11	Polynomial function . . . . .	73
4.12	Möbius transformation . . . . .	73
4.13	Trigonometric functions . . . . .	74
4.14	Visualization of $\sqrt{z}$ . . . . .	75
4.15	Visualization of $\sqrt{z^3}$ . . . . .	76
4.16	Visualization of $\sqrt{1 + \sqrt{z}}$ . . . . .	78
4.17	Visualization of complex logarithm . . . . .	79
4.18	Visualization of arcussinus function . . . . .	80
4.19	Texture used for the visualization . . . . .	81
4.20	Visualization of a polynomial function . . . . .	82
4.21	Color scheme . . . . .	83
4.22	Visualization of $\sqrt{z}$ . . . . .	83
4.23	Visualization of the multiple of roots . . . . .	84
4.24	Visualization of $\sqrt{z}$ . . . . .	86
4.25	Hermite polynomials used in the visualization . . . . .	86
4.26	Visualization of $f(z) = \sqrt{1 + \sqrt{z}}$ . . . . .	87
4.27	Visualization of $f(z) = (z - 0.5 + i)^2((0.5 - i)z - 1)$ . . . . .	88
4.28	Visualization of cube root . . . . .	91
4.29	Adaptive subdivision of the graph of $f(z) = z^{1/3}$ . . . . .	92
4.30	Deformation between $A_2$ and $A_1$ . . . . .	98
4.31	Deformation between $A_3$ and $A_2$ . . . . .	99
4.32	Deformation of complex function . . . . .	100

# List of Tables

4.1	Comparison of the errors of the graphs of the function $f(z) = (z - 0.5 + i)^2((0.5 - i)z - 1)$ . . . . .	89
4.2	Average, maximal and Hausdorff errors of the graph of the function $g(z) = \sqrt[3]{z + 0.6 + 0.4i}$ . . . . .	90
4.3	Average, maximal and Hausdorff errors of the graph of the function $h(z) = \sqrt{1 + \sqrt{z}}$ . . . . .	93
4.4	Comparison of the distribution of the errors of the graphs for non-adaptive subdivision . . . . .	94
4.5	Comparison of the distribution of the errors of the graphs for adaptive subdivision method . . . . .	95
4.6	Comparison of the Hausdorff error and the maximal error for different subdivision . . . . .	96
4.7	Position of the maximal error in graphs . . . . .	97



# Introduction

Complex analysis is the branch of mathematical analysis that investigates functions of complex numbers. A practical application can be found in various fields of mathematics, e.g. in applied mathematics, number theory, algebra, geometry and topology and also in physics.

Throughout the nineteenth century, the attention of the mathematical world was concentrated on complex function theory. Some of the greatest mathematicians of that period, including Gauss, Cauchy, Abel, Jacobi, Riemann, Weierstrass and others made substantial contributions to this theory. In the past, the main interest was concentrated on study of complex functions and their behaviors. Nowadays the main success is achieved in dynamic complex systems and visualization of fractals.

The visualization of a complex valued function is difficult, because of the real dimension of the ambient space in which its graph is naturally considered. To visualize a real function  $f: \mathbb{R} \rightarrow \mathbb{R}$ , we draw a graph  $y = f(x)$  in a two dimensional Cartesian coordinate system in  $\mathbb{R}^2$  via identifying one axis with the domain of the function and the other axis with its codomain. This method meets with some difficulties when we want to extend it to a complex function  $g: \mathbb{C} \rightarrow \mathbb{C}$ . The main problem arising is that  $\mathbb{C}$  has a real dimension two, thus we need a four-dimensional real space to depict the graph of a complex function  $w = g(z)$ . The most common method is to draw domain and codomain separately. One can also study separately the argument and the absolute value of the function. These methods does not describe the function as a whole part. Therefore the newest approach to visualize the complex function was developed and it is called the domain coloring. This technique uses color scheme to visualize the complex function.

The technique of domain coloring can not be applied directly to visualize multi-valued functions. To visualize such type of function, its Riemann surface is often used as an extended domain of the function. Bernhard Riemann introduced a notion of Riemann surfaces in 1851 in his dissertation thesis. Riemann surfaces originated in complex analysis to let us deal with the problem of multi-valued functions. Such functions occur because the analytical continuation of a given holomorphic function element along different paths with same end points may lead in complex plane to different values of the function in general. Such values form locally different branches of the function. The idea of Riemann surfaces is to replace the domain of the multi-valued function with a many sheeted covering of the complex plane [OoSU10]. If the covering is constructed so, that it has as many points lying over any given point in the plane, as there are function values at that point and satisfying certain smoothness conditions, then the analytical function might be single-valued on this so called “covering surface”.

For example, [YJG07] uses such an universal covering to compute the shortest cycles in each homotopy class of a given surface. The authors of [CL02] use Riemann surfaces to dissolve the problem of multiple bubbles. The surface parametrization method [KNP07] computes a 4-sheeted covering in order to represent the parameter function on higher genus surfaces. The notion of covering spaces provides a nice theoretical foundation of this parametrization approach. Riemann surfaces can also be used to visualize the deformation of ADE singularities [BVC13].

## Outline of the thesis:

**Chapter 1:** This chapter contains basic definitions and notions from the complex analysis. The definition of stereographic projection, which is used in the visualization algorithm, is also included. The chapter describes the Möbius transformation and its properties. In the end of the chapter, the spherical curves are described.

**Chapter 2:** This chapter is dedicated to the theory of Riemann surfaces. They are considered as the natural setting for studying multi-valued functions,

e.g. logarithm, root function, inverse goniometric functions etc. The holomorphic function  $f(z)$  is called a multi-valued, if different paths in the domain of the function in generality, lead to different values of the function  $f(z)$ . This fact lead Riemann to the idea of replacing the domain of the function by a multi-valued covering of the complex plane. This method converts a multi-valued function into a single-valued function.

**Chapter 3:** The chapter provides an overview of methods used to visualize complex functions. The most frequently used method is the domain coloring. This method uses color scheme to visualize the graph of the complex function. The chapter provides an overview of latest publications investigating the problem of visualizing a complex valued function. A problem arises, if the domain does not correspond with the topology of the complex plane. In this case, Riemann surface is considered as the domain of the function, extending the complex plane appropriately.

**Chapter 4:** The last chapter provides an overview of technology used in the implementation of the visualization of single- and multi-valued function. This chapter describes the CoFiViS algorithm for non-adaptive and adaptive single and multi-valued approach. Then, the description of visualizations of chosen single- and multi-valued functions created by this algorithm are provided. The results are compared by the maximal, average and Hausdorff error. In the end of the chapter, the latter examined approaches and the application in visualization of the ADE singularities are described.

# 1

## Basic notions

### 1.1 Complex numbers

In the following text, we use standard definition of the field of the complex numbers, see e.g. [Sha03].

**Definition 1.1.** Let us have a point  $\infty \notin \mathbb{C}$ , called the point at infinity. Let  $\Sigma = \mathbb{C} \cup \{\infty\}$  be the one-point compactification of the complex plane  $\mathbb{C}$ . Open sets of  $\Sigma$  are of two types: open sets in  $\mathbb{C}$  and sets of the form  $V \cup \{\infty\}$ , where  $V \subset \mathbb{C}$  is the complement of a compact set  $K \subset \mathbb{C}$ .

The system of  $\{U_\infty(r)\}_{r \geq 0}$ ,  $U_\infty(r) = \{z \in \mathbb{C}; |z| > r\} \cup \{\infty\}$ , where  $r \in \mathbb{R}$ ,  $r \geq 0$  forms basis of neighborhoods of  $\infty$  in  $\Sigma$ .

The extended complex plane  $\Sigma$ , also called Riemann sphere, can be visualized, if we represent the complex numbers as points on a two-dimensional sphere  $\mathbb{S}^2 \subseteq \mathbb{E}^3$  given as

$$\mathbb{S}^2 = \{(\xi, \eta, \zeta) \in \mathbb{R}^3 \mid \xi^2 + \eta^2 + \zeta^2 = 1\}. \quad (1.1)$$

Let us identify the complex plane  $\mathbb{C}$  with the plane  $\zeta = 0$  by identifying the complex number  $z = \xi + i\eta \in \mathbb{C}$  with the point  $(\xi, \eta, 0)$ , for all  $z \in \mathbb{C}$ . Let  $N = (0, 0, 1)$  be the 'north pole' of  $\mathbb{S}^2$ . Then the stereographic projection from  $N$  projects the points from complex plane  $\mathbb{C}$  on the sphere  $\mathbb{S}^2$ .

**Note 1.** We call the point  $S = (0, 0, -1)$  the south pole of the sphere  $\mathbb{S}^2$ . Then the sphere is divided into north and south hemisphere by the parallel contained in the plane  $\zeta = 0$  also called the "equator".

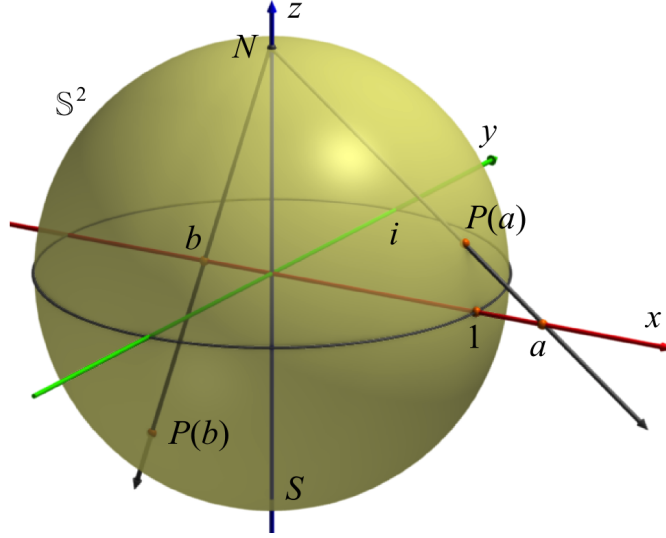


**Figure 1.1:** The figure depicts example of the points mapped by stereographic projection  $P$  onto sphere  $\mathbb{S}^2$ . Notice, that the point  $a$ , which is positioned outside the unit disc in the  $\xi\eta$  plane is projected on the north hemisphere. The point  $b$ , positioned inside the unit disc is projected on the south hemisphere. Points on the unit circle are fixed.

**Definition 1.2** (Stereographic projection). The function  $P: \mathbb{C} \rightarrow \mathbb{S}^2$ , which projects the point  $z = (\xi, \eta) \in \mathbb{C}$  onto point  $Z = (\xi, \eta, \zeta) \in \mathbb{S}^2$ , given by the formula

$$\xi = \frac{2\xi}{1 + |z|^2}, \quad \eta = \frac{2\eta}{1 + |z|^2}, \quad \zeta = \frac{|z|^2 - 1}{1 + |z|^2}, \quad (1.2)$$

is called stereographic projection. Samples of points projected by stereographic projection can be seen in Fig. 1.1.

Stereographic projection is a homeomorphism between  $\mathbb{S}^2 \setminus \{N\}$  and  $\mathbb{C}$ , which can be easily extended to bijection  $P: \mathbb{S}^2 \rightarrow \Sigma$  by defining  $P(\infty) = N$ .

**Note 2** (Riemann sphere). The extended complex plane  $\Sigma$  has same topological properties as a unit sphere  $\mathbb{S}^2$ , and it is often called Riemann sphere. The Riemann sphere  $\Sigma$  inherits geometric attributes and notions from the unit sphere  $\mathbb{S}^2$ .

**Definition 1.3** (Isolated singular point). A point  $a \in \Sigma$  is called an isolated singular point of a function  $f: \Sigma \rightarrow \Sigma$  iff there exists a punctured neighborhood  $O$  of  $a$ , i.e. a set containing the set  $O = \{z \in \Sigma: 0 < |z - a| < r\}$ ,  $r > 0$  for  $a \neq \infty$  and  $O = \{z \in \Sigma: R < |z| < \infty\}$ ,  $R > 0$  for  $a = \infty$ , where  $f$  is holomorphic and  $f$  is not holomorphic in the point  $a$ .

**Definition 1.4.** Singular point  $s$  of a function  $f$  can be categorized into 3 types:

1. removable singular point, if the limit of the function  $\lim_{z \rightarrow s} f(z)$  exists and is finite,
2. pole, if the limit of the function  $\lim_{z \rightarrow s} f(z)$  exists and is equal to  $\infty$ ,
3. essential singular point, if  $\lim_{z \rightarrow s} f(z)$  does not exist.

**Definition 1.5** (Single-valued function). We say the function  $f: M \rightarrow \mathbb{C}$ , where  $M \subseteq \mathbb{C}$ , is single-valued, if to each value  $z_1 \in M$  of the independent variable associates exactly one value  $f(z_1)$  of the dependable variable.

Later, we also work with multi-valued functions, which cannot in general be visualized in a similar way.

## 1.2 Möbius transformation

The concept of limit, derivative and other notions based on limit and derivative are straightforward generalization of analog notions from real analysis. Detail can be found in [Sha03], [Lan99].

To define Möbius transformation, we need definition of meromorphic function and its properties.

**Definition 1.6.** Let  $X$  be a Riemann surface and  $Y$  be an open subset of  $X$ . By a meromorphic function on  $Y$ , we mean a holomorphic function  $f: Y' \rightarrow \mathbb{C}$ , sphere  $Y' \subset Y$  is an open subset such that the following conditions hold.

- $Y \setminus Y'$  contains only isolated points.
- For every point  $p \in Y \setminus Y'$  has  $\lim_{x \rightarrow p} |f(x)| = \infty$ .

The points of  $Y \setminus Y'$  are called the poles of  $f$ .

Rational function is a fraction of two polynomial functions.

**Theorem 1.1.** A function  $f: \Sigma \rightarrow \Sigma$  is rational iff it is meromorphic on  $\Sigma$ , [JS87].

An automorphism of the Riemann sphere  $\Sigma$  is a meromorphic bijection  $L: \Sigma \rightarrow \Sigma$ . Denote the set of all automorphisms  $\Sigma$  by  $Aut(\Sigma)$ .

**Theorem 1.2.** The set of all automorphisms  $Aut(\Sigma)$  consists of functions

$$L(z) = \frac{az + b}{cz + d}, \text{ where } ad - bc \neq 0, \quad (1.3)$$

where the coefficients  $a, b, c, d \in \mathbb{C}$  and  $z$  is complex variable.

Such a transformation  $L(z)$  is called Möbius transformation.

The coefficients  $a, b, c, d$  in the transformation  $L(z)$  are not unique. If we take arbitrary  $\lambda \in \mathbb{C} \setminus 0$ , then  $\lambda a, \lambda b, \lambda c, \lambda d$  determine the same transformation  $L(z)$ .

We require condition  $ad - bc \neq 0$  to eliminate case  $L(z) = const$ . If  $c = 0$ , while  $d \neq 0$  the function  $L(z) = \frac{a}{d}z + \frac{b}{d}$  is linear.

If  $c \neq 0$ , the function  $L(z)$  given by the equation (1.3) is not defined for  $z = -\frac{d}{c}$  and  $z = \infty$ . If  $c = 0$ , the Möbius transformation is defined for every finite  $z \in \mathbb{C}$ . We define:

$$L(z) = \infty \text{ for } z = -\frac{d}{c} \quad (1.4)$$

and

$$L(z) = \frac{a}{c} \text{ for } z = \infty. \quad (1.5)$$

Then, the following theorem holds.

**Theorem 1.3.** The Möbius transformation (1.3) with defined values (1.4) and (1.5) is a homeomorphism from  $\Sigma$  on  $\Sigma$ .

The Möbius transformation is conformal (locally angle preserving) on a whole  $\Sigma$ .

Let us take a closer look on the geometric properties of the Möbius transformation.

**Theorem 1.4.** The Möbius transformation maps a circle in  $\Sigma$  onto a circle in  $\Sigma$ .

In Fig. 1.2, an example of circles transformed by Möbius transformation given by formula  $L(z) = \frac{z+i}{z-i}$  is depicted.

**Theorem 1.5.** If  $z_1, z_2, z_3 \in \Sigma$  are three mutually distinct elements, then there exists one and only one Möbius transformation  $L$ , which satisfies following equations:  $L(z_1) = 0, L(z_2) = 1, L(z_3) = \infty$ .

The following two corollaries follow from the Theorem 1.5.

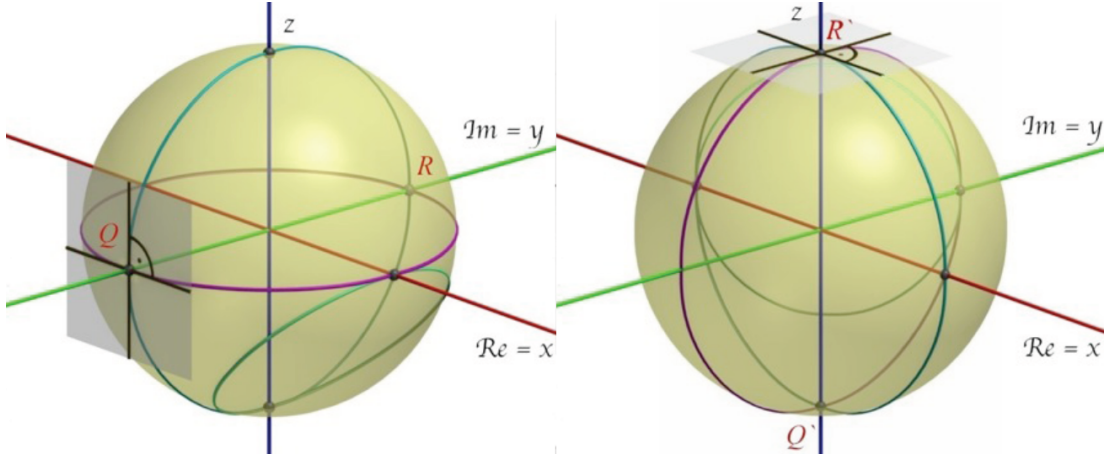


**Figure 1.2:** Example of Möbius transformation  $L(z) = \frac{z+i}{z-i}$ . Notice, that the transformation preserve angles between considered circles.

**Corollary 1.** For arbitrary two triplets of points  $z_1, z_2, z_3 \in \Sigma$  and  $w_1, w_2, w_3 \in \Sigma$ , where in each triplet the points are mutually distinct, exists one and only one Möbius transformation  $L$ , which satisfies  $L(z_i) = w_i, i = 1, 2, 3$ .

**Corollary 2.** If  $L: \Sigma \rightarrow \Sigma$  is a Möbius transformation and  $L$  has three mutually distinct fixed points from  $\Sigma$ , then  $L$  is an identical transformation on  $\Sigma$ . Therefore, nonidentical Möbius transformations have two or less fixed points.

It is useful to consider the following special types of Möbius transformation:

1.  $R_\Theta(z) = e^{i\Theta}z$ , where  $\Theta \in \mathbb{R}$ . This function defines a rotation of the Riemann sphere  $\Sigma$  by the angle  $\Theta$  around the vertical axis intersecting points  $0$  and  $\infty$ .
2.  $J(z) = 1/z$ , also called complex inversion, represents inversion composed with reflection with respect to real axis, see Fig. 1.3.
3.  $S_r(z) = rz$ , where  $r \in \mathbb{R}, r > 0$ . The transformation  $S_r$  fixes points  $0, \infty$  and acts on the the plane  $\mathbb{C}$  as a similarity transformation, expanding or contracting distances by a factor  $r$ .
4.  $T_t(z) = z + t$ , where  $t \in \mathbb{C}$  defines a translation of the complex plane  $\mathbb{C}$ . This transformation fixes the point  $\infty$ .



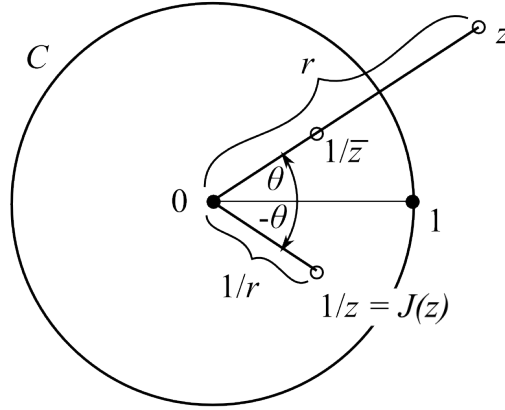


**Figure 1.3:** Point  $z$  mapped by the complex inversion  $J(z) = 1/z$  [Nee00].

**Theorem 1.6.** Every Möbius transformation is a composition of finitely many Möbius transformations of types 1, ..., 4.

If we work with a normalized Möbius transformation, that is  $ad - bc = 1$ , the fixed points  $\xi_+$  a  $\xi_-$  have form

$$\xi_{\pm} = \frac{(a - d) \pm \sqrt{(a + d)^2 - 4}}{2c}. \quad (1.6)$$

The normalized Möbius transformation  $L$  can be divided into 4 types according to the value of the term  $(a + d)^2$ :

- We say, that  $L(z)$  is elliptic iff  $(a + d)^2 \in \mathbb{R}$  and  $0 \leq (a + d)^2 < 4$ .
- $L(z)$  is called parabolic, iff  $(a + d)^2 = 4$ . In this case, the transformation has only one fixed point  $p = \xi_+ = \xi_-$ , which is double.
- $L(z)$  is hyperbolic transformation iff  $(a + d)^2 \in \mathbb{R}$  and  $(a + d)^2 > 4$ .
- Loxodromic transformation  $L(z)$  is Möbius transformation with  $(a + d)^2 \in \mathbb{R}$  and  $(a + d)^2 < 0$  or  $(a + d)^2 \notin \mathbb{R}$ .

Let us discuss the case, when  $c = 0$ , that is, at least one fixed point is at infinity. If  $c = 0$ , the Möbius transformation takes the form  $L(z) = Az + B$ . If we write  $A = re^{i\theta}$ , then this may be viewed as the composition of an origin-centered

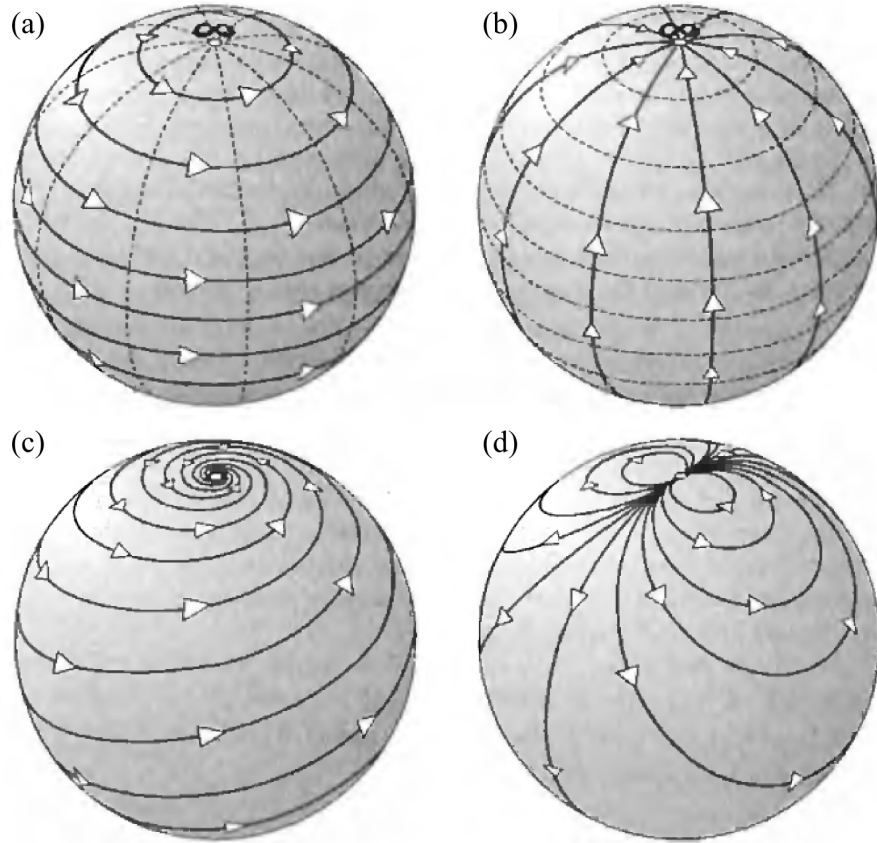


**Figure 1.4:** Möbius transformation can be divided into four types: (a) elliptic, (b) hyperbolic, (c) loxodromic and (d) parabolic [Nee00]

rotation of  $\Theta$ , an origin-centered expansion by  $r$  and finally a translation of  $B$ . Let us visualize each of these three transformation of the Riemann sphere.

For  $\Theta > 0$ , the Fig. 1.4 (a) illustrates the rotation  $R_\Theta(z) = e^{i\Theta}z$ .  $R_\Theta(z)$  fixes points  $0$  and  $\infty$ . Invariant curves are concentric circles with center in point  $0$ . The rotation is the simplest example of elliptic Möbius transformation. The scaling  $S_r(z) = rz$  is depicted in Fig. 1.4 (b). The invariant curves are circles intersecting points  $0$  and  $\infty$ . Again, the fixed points are  $0$  and  $\infty$ . This transformation is an example of hyperbolic Möbius transformation. The loxodromic transformation can be obtained by combination of rotation around the center of the coordination system and scaling, see Fig. 1.4 (c). Here, the invariant curves are the illustrated

”spirals”. Finally, Fig. 1.4 (d) illustrates a translation. Invariant curves are circles intersecting in point  $p$ , which have same tangent line in the point  $p$ . Since  $\infty$  is the only fixed point, the translation is an example of a parabolic Möbius transformation.

More details about Möbius transformation can be found e.g. in [Nee00], [Sha03] and [JS87].

### 1.3 Spherical splines

To highlight the behavior of the Riemann surface around a singular point, we can use spherical splines. Before defining the spherical splines, let us recall the definition of the projective space and the homogeneous coordinates.

**Definition 1.7.** Let  $E$  be a vector space. The projective space derived from  $E$ , denoted by  $P(E)$ , is the quotient of  $E \setminus 0$  by the equivalence relation  $\mathbf{x} \sim \mathbf{y}$  iff  $\mathbf{y} = \lambda \mathbf{x}$  for some  $\lambda \in \mathbb{K}$ . The dimension of  $P(E)$  is  $\dim(E) - 1$ . The canonical projection is  $p: E \setminus \{0\} \rightarrow P(E)$ ,  $\mathbf{x} \mapsto [\mathbf{x}]$ .

A projective space is called real, if  $K = \mathbb{R}$ , and complex if  $K = \mathbb{C}$ . Computations in  $P(E)$  are based on computations in underlying vector space  $E$ ,  $\dim E = n + 1 < \infty$ , where we pick a fixed basis  $\{\mathbf{e}_i\}_{i=0,\dots,n}$ . Every  $\mathbf{m} \in P(E)$  is of the form  $\mathbf{m} = p(\mathbf{x}) = p(x_0, x_1, \dots, x_n)$ , where  $\mathbf{x} = (x_0, x_1, \dots, x_n)$  in the basis being considered. We say that  $(x_0, x_1, \dots, x_n)$  is a set of homogeneous coordinates of  $\mathbf{x}$  with respect to the basis  $\{\mathbf{e}_i\}_{i=0,1,\dots,n}$ . The word ‘homogeneous’ comes from the fact that the sets of homogeneous coordinates of a point  $\mathbf{m} \in P(E)$  are all of form  $(\lambda x_0, \lambda x_1, \dots, \lambda x_n)$ , for all  $\lambda \in \mathbb{K} \setminus \{0\}$  and fixed  $x_0, x_1, \dots, x_n$ .

Take a basis  $\{\mathbf{e}_i\}_{i=0,1,\dots,n}$  of  $E$ , and define the hyperplanes  $H_i$  as  $H_i = x_i^{-1}(0)$ . The points from projective space  $P(E) \setminus P(H_i)$  are those whose homogeneous coordinates  $(x_0, x_1, \dots, x_n)$  satisfy  $x_i \neq 0$ .

By intersecting of hyperplanes, linear varieties of lower dimension can be defined.

In the following, we work in the 3-dimensional projective space, where points have homogenous coordinates of a form  $\mathbf{x} = (x_0, x_1, x_2, x_3)$ , where  $x_3 \neq 0$ . The points homogeneous coordinates  $\vec{\mathbf{x}} = (x_0/x_3, x_1/x_3, x_2/x_3, 0)$ , where  $x_i \neq 0$  for  $i \in \{0, 1, 2\}$  are the ideal points or the point at infinity in the direction of  $(x_0, x_1, x_2)$ .

---

## 1. BASIC NOTIONS

---

In projective space, if three points  $\mathbf{a}$ ,  $\mathbf{b}$  and  $\mathbf{x}$  lie on one line, then one of the points can be expressed as linear combination of other two points:  $\mathbf{x} = \alpha\mathbf{a} + \beta\mathbf{b}$ , where  $\alpha, \beta \in \mathbb{R}$ . We denote the couple  $[\alpha, \beta]$  as the projective coordinates of a point  $\mathbf{x}$  with respect of line defined by the points  $\mathbf{a}, \mathbf{b}$ .

We can pass over on the unit sphere, situated in the beginning of the coordinate system without loss of generality. Our aim is to find all rational splines with suitable degree on the surface of the sphere. We use stereographic projection to solve this problem, see definition 1.2.

It is well known, that the coordinates of every point  $\mathbf{x} = (x, y, z, w)$ , that is lying on the unit sphere satisfies equation  $x^2 + y^2 + z^2 = w^2$ . If the point  $\mathbf{x}$  lies on a polynomial curve  $\mathbf{x}(t)$ , then it satisfies the equation

$$x^2(t) + y^2(t) + z^2(t) = w^2(t). \quad (1.7)$$

The polynomials  $x(t)$ ,  $y(z)$ ,  $z(t)$  and  $w(t)$  satisfying the equation (1.7) have to be such that

$$\begin{aligned} x &= p_0^2 + p_1^2 + p_2^2 + p_3^2 & \text{or} & & x &= -p_0^2 - p_1^2 - p_2^2 - p_3^2, \\ y &= 2p_0p_1 - 2p_2p_3, \\ z &= 2p_2p_3 + 2p_0p_2, \\ w &= p_1^2 + p_2^2 - p_0^2 - p_3^2, \end{aligned} \quad (1.8)$$

where  $p_i = p_i(t)$  are polynomials [Far99]. It is clear from (1.8), that the polynomial curve lying on the unit sphere must have even degree. We can get the formula of the curve by the stereographic projection. By the projection, every point from the plane  $\langle O, x, y \rangle$  is mapped on the unit sphere. The mapping is given by the following formula in homogeneous coordinates

$$P^2(\mathbb{C}) \ni \begin{pmatrix} x \\ y \\ w \end{pmatrix} \mapsto \begin{pmatrix} 2xw \\ 2yw \\ x^2 + y^2 - w^2 \\ x^2 + y^2 + w^2 \end{pmatrix} \in \mathbb{S}^2 \subseteq P^3(\mathbb{C}). \quad (1.9)$$

From the definition of the stereographic projection (1.2) it follows that the points

$$\begin{pmatrix} 0 \\ 0 \\ 1 \\ 1 \end{pmatrix}, \begin{pmatrix} 2xw \\ 2yw \\ x^2 + y^2 - w^2 \\ x^2 + y^2 + w^2 \end{pmatrix}, \begin{pmatrix} x \\ y \\ 0 \\ w \end{pmatrix} \quad (1.10)$$

are collinear.

If the points  $[x(t), y(t), 0, w(t)]^\top$  are from Bézier curve then (1.9) can be used to compute the Bézier control points of the curve [Far99].

Another approach of determining quadratic curves on the sphere is by using Bézier curves of second degree. These curves match to the circles on the sphere, that are images of circles or lines projected by stereographic projection on the sphere. Such a curve is given by the formula

$$X(t) = \frac{\mathbf{b}_0 B_0^2(t) + \mathbf{b}_1 \omega B_1^2(t) + \mathbf{b}_2 B_2^2(t)}{B_0^2(t) + \omega B_1^2(t) + B_2^2(t)}, t \in \langle 0, 1 \rangle, \quad (1.11)$$

where the control points  $\mathbf{b}_i$  must satisfy the circle condition  $|\mathbf{b}_0 \mathbf{b}_1| = |\mathbf{b}_1 \mathbf{b}_2|$ . The quadratic Bernstein polynomials are given as  $B_i^2(t) = \binom{2}{i} t^i (1-t)^{2-i}$ ,  $i = 0, 1, 2$  and  $\omega$  is the weight. The weights  $w_0 = w_2 = 1$ . Suppose, that  $\mathbf{b}_0$  and  $\mathbf{b}_2$  lie on unit sphere with center in point  $O = (0, 0, 0)$ . Then the angle  $2\phi = \angle \mathbf{b}_0 O \mathbf{b}_2$  can be determined by

$$2 \cos \phi = |\mathbf{b}_0 + \mathbf{b}_2|. \quad (1.12)$$

Because of the circle condition,  $\mathbf{b}_1$  must lie on a plane bisecting the angle  $\angle \mathbf{b}_0 O \mathbf{b}_2$  and perpendicular to the plane determined by  $\langle O, \mathbf{b}_0, \mathbf{b}_2 \rangle$ . Additionally  $\mathbf{b}_1$  must lie in the tangent plane to the sphere at  $\mathbf{b}_0$  and in the tangent plane to the sphere at  $\mathbf{b}_2$ . Thus  $\mathbf{b}_1$  can have the representation

$$\mathbf{b}_1 = \frac{\mathbf{b}_0 + \mathbf{b}_2}{2 \cos^2 \phi} + \lambda \frac{\mathbf{b}_0 \times \mathbf{b}_2}{\sin 2\phi}, \quad (1.13)$$

where the parameter  $\lambda$  describes the distance of  $\mathbf{b}_1$  from the plane determined by  $\langle O, \mathbf{b}_0, \mathbf{b}_2 \rangle$ , see Fig. 1.5. The term  $\mathbf{x} \times \mathbf{y}$  denotes the vector product, which is defined by

$$\mathbf{x} \times \mathbf{y} = \left[ \left[ \begin{array}{cc|c} x_2 & y_2 & 1 \\ x_3 & y_3 & 0 \end{array} \right], - \left[ \begin{array}{cc|c} x_1 & y_1 & 1 \\ x_3 & y_3 & 0 \end{array} \right], \left[ \begin{array}{cc|c} x_1 & y_1 & 1 \\ x_2 & y_2 & 0 \end{array} \right] \right]. \quad (1.14)$$

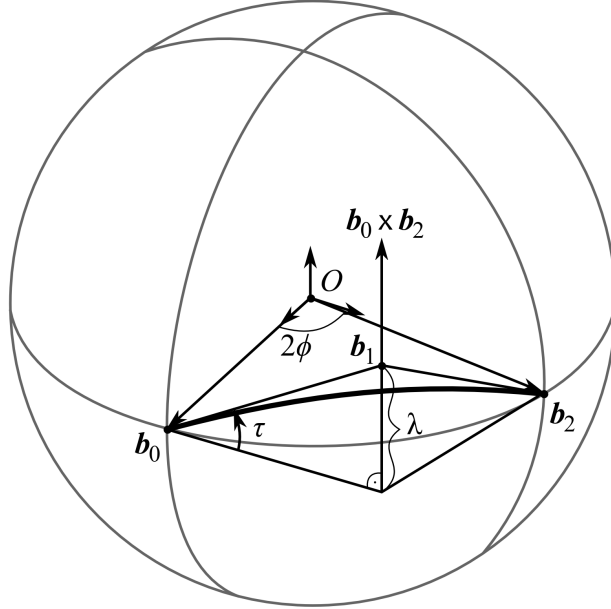


**Figure 1.5:** Representation of a circle on the sphere. Notice the parameters  $\tau$  and  $\lambda$ , which affect the position of the point  $\mathbf{b}_1$  [HS92].

If  $\lambda = 0$ , the equation (1.11) gives a parametric representation of a spherical great circle, for  $\lambda \neq 0$  we get small circles on the sphere. Additionally the weight  $\omega$  must be adapted: if (1.11) satisfies the circle equation, we get

$$\omega = \frac{\sin \phi}{\sqrt{\lambda^2 + \tan^2 \phi}}. \quad (1.15)$$

Instead of the parameter  $\lambda$  we can also introduce the angle  $\tau$  between the plane  $\langle O, \mathbf{b}_0, \mathbf{b}_2 \rangle$  and the Bézier polygon as measure for the deviation of a small circle from the great circle. For a great circle we have  $|\mathbf{b}_0 \mathbf{b}_1| = \tan \phi$ , thus we obtain the equation

$$\tan \tau \tan \phi = \lambda \quad (1.16)$$

and for the weight  $\omega$  with (1.15)

$$\omega = \cos \phi \cos \tau. \quad (1.17)$$

For  $\tau = \frac{\pi}{2}$ , the circular arc is a half circle, while in this case  $\omega = 0$  and the control point  $\mathbf{b}_1$  moves to infinity. Therefore, we have to split the parametric

---

## 1. BASIC NOTIONS

---

representation (1.11) of the circular arc to

$$X(t) = \frac{\mathbf{b}_0 B_0^2(t) + \mathbf{b}_2 B_2^2(t)}{B_0^2(t) + B_2^2(t)} + \frac{\vec{\mathbf{b}}_1 B_1^2(t)}{B_0^2(t) + B_2^2(t)}, \quad (1.18)$$

where  $\vec{\mathbf{b}}_1$  is the direction which points to the position of  $\mathbf{b}_1$  at infinity. From equations (1.11), (1.13) and (1.16) we get

$$\vec{\mathbf{b}}_1 = \frac{\mathbf{b}_0 \times \mathbf{b}_2}{2 \cos^2 \phi} \sin \tau. \quad (1.19)$$

For  $\tau = \pi$ , we get the complement arc of the circular arc which we would obtain for  $\tau = 0$ .

Now, we connect circular arcs to circular  $C^1$  spherical spline curves. The  $i$ -th spline segment may have the representation

$$\mathbf{X}_i(t) = \frac{\mathbf{b}_{2i} B_0^2(t) + \mathbf{b}_{2i+1} \omega_i B_1^2(t) + \mathbf{b}_{2i+2} B_2^2(t)}{B_0^2(t) + \omega_i B_1^2(t) + B_2^2(t)}, i = 0 \dots n - 1, \quad (1.20)$$

with  $B_k^2(t)$ ,  $k = 0, 1, 2$  as Bernstein polynomials over the interval  $t \in \langle 0, \mu_i \rangle$  and  $\mu_i$  as the length of the parameter interval of the segment  $\mathbf{X}_i$ . Two neighboring spline segments are  $C^1$ -continuous iff the first derivatives in two corresponding boundary points are equal. Thus, we get the condition

$$\omega_{i+1} \mu_i (\mathbf{b}_{2(i+1)+1} - \mathbf{b}_{2(i+1)}) = \omega_i \mu_{i+1} (\mathbf{b}_{2(i+1)} - \mathbf{b}_{2i+1}). \quad (1.21)$$

If we insert (1.13), (1.16) and (1.17) to the equation (1.21) this condition reduces to

$$\mu_i \sin \phi_{i+1} = \mu_{i+1} \sin \phi_i. \quad (1.22)$$

Additionally from (1.21) follows that three neighboring Bézier points  $\mathbf{b}_{2i+1}$ ,  $\mathbf{b}_{2i+2}$  and  $\mathbf{b}_{2(i+1)+1}$  are collinear [HS92].

## 2

# Riemann surfaces

The concept of Riemann surfaces is fundamental in modern complex analysis, topology and algebraic geometry. Moreover, such surfaces are utilized also in several methods in computer graphics. For example, [YJG07] uses the universal covering to compute the shortest cycles in each homotopy class of given surface.

Riemann surfaces were first studied by Bernhard Riemann. They are considered the natural setting for studying multi-valued functions, e.g. logarithm, root function, inverse goniometric functions etc. The holomorphic function  $f(z)$  is called multi-valued, if different paths in generality, lead to different branches of the function  $f(z)$ . This fact led Riemann to an idea to replace the domain of the function by multi-valued covering of the complex plane. This method converts the multi-valued function into the single-valued function. The information about the topic is considered in more detail and the proofs can be found, e.g. in [For81, JS87, Spr57, Fre11, Coh67, WM13].

## 2.1 Definition of the Riemann surface

**Definition 2.1.** An  $n$ -dimensional manifold is a Hausdorff, second countable topological space  $X$  such that every point  $a \in X$  has an open neighborhood which is homeomorphic to an open subset of  $\mathbb{R}^n$ .

A topological space  $X$  is a Hausdorff space, if for any two distinct points  $a, b \in X$  there exist a neighborhood  $U$  of  $a$  and a neighborhood  $V$  of  $b$  such that  $U$  and  $V$  are disjoint in  $X$ .



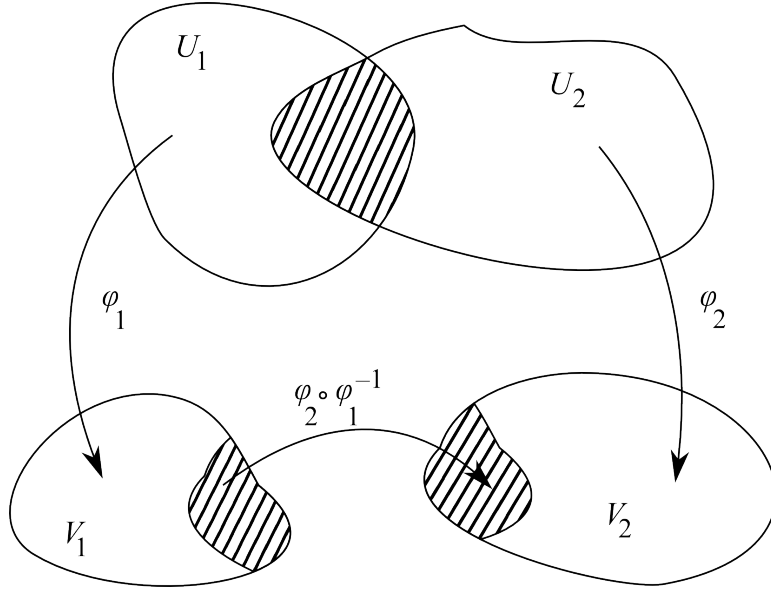


**Figure 2.1:** Two complex charts  $\phi_i: U_i \rightarrow V_i$ ,  $i = 1, 2$  are said to be *holomorphically compatible* if the map  $\phi_2 \circ \phi_1^{-1}$  is biholomorphic [For81].

**Definition 2.2.** Let  $X$  be a two-dimensional manifold. A *complex chart* on  $X$  is a pair  $(U, \phi)$ , where  $\phi: U \rightarrow V$  is a homeomorphism and  $U \subset X$  and  $V \subset \mathbb{C}$  are open subsets. Two complex charts  $\phi_i: U_i \rightarrow V_i$ ,  $i = 1, 2$  are said to be *holomorphically compatible* if the map

$$\phi_2 \circ \phi_1^{-1}: \phi_1(U_1 \cap U_2) \rightarrow \phi_2(U_1 \cap U_2) \quad (2.1)$$

is biholomorphic (bijective holomorphic function whose inverse is also holomorphic), see Fig. 2.1.

If  $s \in U$ , we call  $(U, \phi)$  a chart at  $s$  and  $z = \phi(s)$  a local coordinate for  $s$ . The function  $\phi_2 \circ \phi_1^{-1}$  is called the coordinate transition function and is defined whenever  $U_1 \cap U_2 \neq \emptyset$ .

A *complex atlas* on  $X$  is a system of complex charts  $\mathcal{U} = \{(U_i, \phi_i): U_i \subset X, \phi_i: U_i \rightarrow V_i, i \in I\}$ , which are holomorphically compatible and form a cover of  $X$ , i.e.  $\bigcup_{i \in I} U_i = X$ . Two complex atlases  $\mathcal{U}$  and  $\mathcal{U}'$  on  $X$  are *analytically equivalent*, if every chart of  $\mathcal{U}$  is holomorphically compatible with every chart of  $\mathcal{U}'$ . An atlas  $\mathcal{U}$  on  $X$  is called *analytic*, if all its coordinate transition functions are analytic.

---

## 2. RIEMANN SURFACES

---

**Definition 2.3.** An equivalence class of analytically equivalent atlases on  $X$  is called a *complex structure* on a 2-dimensional manifold  $X$ .

Thus a complex structure on  $X$  can be given by a choice of the complex atlas. Every complex structure  $\Sigma$  on  $X$  contains a unique maximal atlas  $\mathcal{U}^*$ . If  $\mathcal{U}$  is an arbitrary atlas in  $\Sigma$ , then  $\mathcal{U}^*$  consists of all complex charts  $\mathcal{U}$  on  $X$  which are holomorphically compatible with every chart of  $\mathcal{U}$ .

**Definition 2.4.** A *Riemann surface* is a pair  $(X, \mathcal{S})$ ,  $X$  being a connected 2-dimensional manifold and  $\mathcal{S}$  a complex structure on  $X$ .

One usually writes  $X$  instead of  $(X, \mathcal{S})$ , whenever it is clear which complex structure  $\mathcal{S}$  is considered.

**Example 2.1.** The complex plane  $\mathbb{C}$ . Its complex structure is defined by the atlas whose only chart is the identity map  $f: \mathbb{C} \rightarrow \mathbb{C}$ .

**Example 2.2.** The Riemann sphere  $\Sigma$ . Let  $\Sigma = \mathbb{C} \cup \{\infty\}$  from Definition 1.1. With defined topology  $\Sigma$  is a compact Hausdorff topological space, homeomorphic to the 2-sphere  $\mathbb{S}^2$ . Set

$$U_1 = \Sigma \setminus \{\infty\} = \mathbb{C}, \tag{2.2}$$

$$U_2 = \Sigma \setminus \{0\}. \tag{2.3}$$

Define maps  $\phi_i: U_i \rightarrow \mathbb{C}$ ,  $i = 1, 2$  as follows. Let  $\phi_1$  be the identity map and

$$\phi_2(z) = \begin{cases} 1/z & \text{for } z \in \mathbb{C} \setminus 0 \\ 0 & \text{for } z = \infty. \end{cases} \tag{2.4}$$

The maps  $\phi_i$ ,  $i = 1, 2$  are homeomorphisms and thus  $\Sigma$  is a two-dimensional manifold. Since the sets  $U_1$  and  $U_2$  are connected and they have non-empty intersection,  $\Sigma$  is also connected.

The complex structure on  $\Sigma$  is defined by the atlas consisting of the charts  $\phi_i: U_i \rightarrow \mathbb{C}$ ,  $i = 1, 2$ . We must show that the two charts are holomorphically compatible. But  $\phi_1(U_1 \cap U_2) = \phi_2(U_1 \cap U_2) = \mathbb{C} \setminus 0$  and  $\phi_2 \circ \phi_1^{-1}: \mathbb{C} \setminus 0 \rightarrow \mathbb{C} \setminus 0$ ,  $z \mapsto 1/z$ , is biholomorphic.

Suppose  $X$  and  $Y$  are topological spaces. A mapping  $p: Y \rightarrow X$  is called a covering map, if every point  $x \in X$  has an open neighborhood  $U$  such that its pre-image  $p^{-1}(U)$  can be represented as  $p^{-1}(U) = \bigcup_{j \in J} V_j$ , where the  $V_j$ ,  $j \in J$ , are disjoint open subsets of  $Y$ , and all the mappings  $p|_{V_j}: V_j \rightarrow U$  are homeomorphisms [Lan99].

**Definition 2.5.** A path  $\gamma$  is a continuous function  $\gamma: I \rightarrow \Sigma$ , where  $I$  is the closed unit interval  $[0, 1] = \{s \in \mathbb{R} \mid 0 \leq s \leq 1\}$ . Since  $\gamma$  is continuous and  $I$  is compact and connected, the image  $\gamma(I)$  is also compact and connected.

**Theorem 2.1.** Suppose  $X, Y$  are Hausdorff spaces with  $X$  path-wise connected and  $p: Y \rightarrow X$  is a covering map. Then for any two points  $x_0, x_1 \in X$ , the sets  $p^{-1}(x_0)$  and  $p^{-1}(x_1)$  have the same cardinality. In particular, if  $Y$  is non-empty, then  $p$  is surjective.

The cardinality of  $p^{-1}(x)$  for  $x \in X$  is called the *number of sheets* of the covering and may be either finite or infinite.

**Definition 2.6.** Assume that  $X$  and  $Y$  are Riemann surfaces and  $p: X \rightarrow Y$  is a non-constant holomorphic map. A point  $y \in Y$  is called a *branch point* or a *ramification* of  $p$ , if there is no neighborhood  $V$  of  $y$  such that  $p|_V$  is injective. The map  $p$  is called an *unbranched holomorphic map* if it has no branch points.

A *branch cut*  $L$  is a simple path joining two branch points in the complex plane. If we cut  $\Sigma$  along simple mutually disjoint paths between pairs of branch points of the function  $f$ , we get a simply connected region on which we can define a single-valued meromorphic branch of the multi-valued function.

## 2.2 Orientability of Riemann surfaces

Our aim in this section is to sketch that all Riemann surfaces are orientable.

By identifying each  $z = x + iy \in \mathbb{C}$  with  $(x, y) \in \mathbb{R}^2$ , we can regard the local coordinates of any surface as lying in  $\mathbb{R}^2$ . We say, that an atlas of charts is smooth (or  $C^\infty$ ) if all its coordinate transition functions  $f$  are smooth. As with analytic atlases, two smooth atlases  $\mathcal{A}$  and  $\mathcal{B}$  are called compatible if the atlas  $\mathcal{A} \cup \mathcal{B}$  is smooth. Compatibility between smooth atlases is an equivalence relation, and an equivalence class of smooth atlases is called a smooth structure. Finally a smooth surfaces is a surface with smooth structure. Since every analytic function is smooth, it is clear that every Riemann surface is a smooth surface.

If  $U$  and  $V$  are open subsets of  $\mathbb{R}^2$  and  $f: (x, y) \mapsto (u, v)$  is a smooth function  $U \rightarrow V$ , then the Jacobian of  $f$  is

$$J_f = \frac{\partial u}{\partial x} \frac{\partial v}{\partial y} - \frac{\partial u}{\partial y} \frac{\partial v}{\partial x}. \quad (2.5)$$

If  $J_f > 0$  at all points of  $U$  then  $f$  is said to be orientation-preserving.

**Theorem 2.2.** Every analytic atlas is orientable [JS87].

Compatibility of orientable atlases is defined in the same way as the compatibility of analytic atlases and it is an equivalence relation. An equivalence class of orientable atlases is called an orientation. It can be shown, that every orientable surface  $S$  has just two orientations, described as follows. If  $\mathcal{A} = \{(U_i, \phi_i)\}$  is an orientable atlas for  $S$ , we define  $\bar{\mathcal{A}} = \{(U_i, \bar{\phi}_i)\}$  where  $\bar{\phi}_i(s) = (x, -y)$  whenever  $\phi_i(s) = (x, y) \in \mathbb{R}^2$ . In complex coordinates, this is just a complex conjugation. Then  $\bar{\mathcal{A}}$  is easily seen to be an orientable atlas for  $S$  which is not compatible with  $\mathcal{A}$ . The equivalence class containing  $\mathcal{A}$  and  $\bar{\mathcal{A}}$  give the two orientations for  $S$ .

### 2.3 Meromorphic continuation and Riemann surfaces

Now, we have the definition of Riemann surfaces and the application of Riemann surfaces. In the following text, we explain the theory needed to construct the Riemann surfaces of a chosen function  $f(z)$ .

**Definition 2.7.** We define the function element to be a pair  $(D, f)$ , where  $D$  is a region (recall that a region is a non-empty, path-connected, open set) and  $f: D \rightarrow \Sigma$  is a single-valued meromorphic function on  $D$ . If  $f$  is an analytic function, we shall call  $(D, f)$  an analytic function element.

For example if  $f$  is any rational function then  $(\Sigma, f)$  is a functional element. The domain  $D = \Sigma$  was chosen to be the largest on which  $f$  is meromorphic.

**Lemma 2.1.** Let  $(D, f)$  and  $(D, g)$  be function elements on the same region  $D$ . If  $f \equiv g$  on some non-empty open subset  $U \subset D$ , then  $f \equiv g$  on  $D$ .

**Corollary 3.** If  $(D_1, f_1)$  is a function element and  $D_2 \subseteq \mathbb{C}$  is a region with  $D_1 \cap D_2 \neq \emptyset$ , then there is at most one meromorphic function  $f_2: D_2 \rightarrow \mathbb{C}$  on  $D_2$  that  $f_1 \equiv f_2$  on  $D_1 \cap D_2$ .

When such a function  $f_2$  exists, we call the function element  $(D_2, f_2)$  a direct meromorphic continuation on  $(D_1, f_1)$ , or a direct analytic continuation if  $f_2$  is analytic. In either case, we write  $(D_1, f_1) \sim (D_2, f_2)$ , meaning that  $D_1 \cap D_2 \neq \emptyset$  and  $f_1 \equiv f_2$  on  $D_1 \cap D_2$ . We then have a function element  $(D, f)$ , where  $D =$

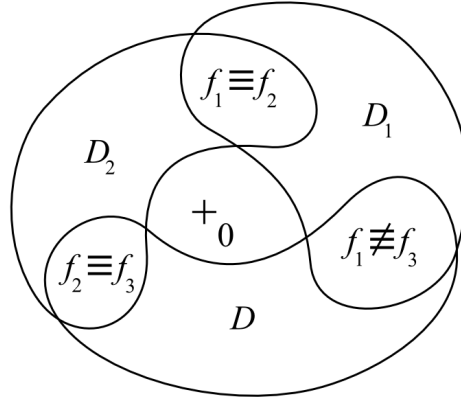


**Figure 2.2:** The figure depicts an example of regions used by creation of the direct meromorphic continuation of  $\log(z)$ . Notice, that we have direct analytic continuations  $(D_1, f_1) \sim (D_2, f_2) \sim (D_3, f_3)$  but  $(D_3, f_3)$  is not analytic continuation of  $(D_1, f_1)$  [JS87].

$D_1 \cup D_2$  and  $f(z) = f_j(z)$  for  $z \in D_j$ . The relation  $\sim$  between function elements is reflexive and symmetric, but not transitive. Therefore, the relation is not a relation of equivalence.

**Example 2.3.** Let us show an example of a meromorphic continuation for the function  $\log(z)$ . Fig. 2.2 illustrates the regions  $D_1, D_2, D_3$  in  $\mathbb{C} \setminus \{0\}$  encircling the origin. If  $f_1$  is a single-valued analytic branch of the many-valued function  $\log(z)$  on  $D_1$ , then we have direct analytic continuations  $(D_1, f_1) \sim (D_2, f_2) \sim (D_3, f_3)$ . It can be shown, that  $f_1(z) \equiv f_2(z)$  on a region  $D_1 \cap D_2$  and  $f_2 \equiv f_3$  on a region  $D_2 \cap D_3$  but we find, that  $f_3 \equiv f_1 + 2\pi i$  on  $D_1 \cap D_3$ , so that  $(D_3, f_3)$  is not analytic continuation of  $(D_1, f_1)$ . This example shows, that the relation  $\sim$  is not a relation of equivalence.

**Definition 2.8.** If  $(D, f)$  is a function element then a point  $c$  on the boundary  $\partial D$  of  $D$  is called a regular point for  $(D, f)$ , if there is a direct meromorphic continuation  $(E, g) \sim (D, f)$  with  $c \in E$ . If there is no such direct meromorphic continuation, then  $c$  is called a singular point for function element  $(D, f)$ . If all points  $c \in \partial D$  are singular, then  $\partial D$  is called the natural boundary of  $(D, f)$ .

**Lemma 2.2.** Let  $(D, f)$  be a function element with  $c \in \partial D$ . If  $c$  is regular for  $(D, f)$ , then the limit  $\lim_{z \rightarrow c} f(z) = \alpha$ ,  $\alpha \in \Sigma$ , where  $z \in D$  exists.

It is important to note, that whether or not a point  $c$  is regular for  $(D, f)$  depends on  $D$  as well as on  $f$ . To deal with the problems of non-uniqueness of

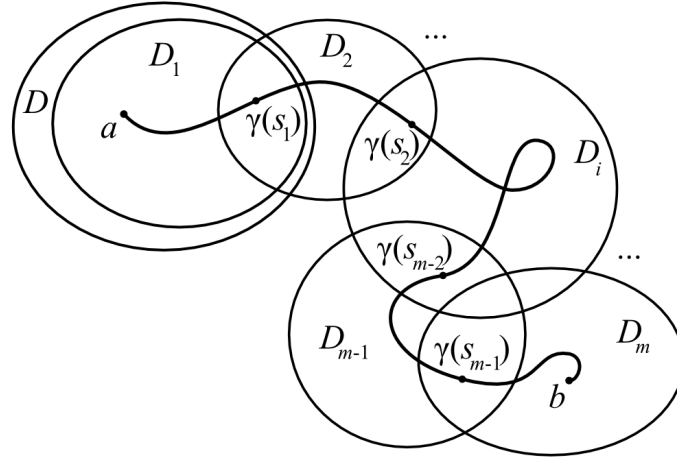


**Figure 2.3:** Figure shows the selection of sets  $D_i$  and subdivision of a path  $\gamma$  for a meromorphic continuation along the path  $\gamma$  [JS87].

meromorphic continuations, we introduce the concept of meromorphic continuation along a path.

If  $a = \gamma(0)$  and  $b = \gamma(1)$ , then we say that  $\gamma$  is a path 'from  $a$  to  $b$ '. The path  $\gamma$  is a closed path, if  $a = b$  and  $\gamma$  is a simple path if  $\gamma(s) = \gamma(s')$  implies either  $s = s'$  or else  $s = 0, s' = 1$ .

**Definition 2.9.** Let  $(D, f)$  be a function element, let  $a \in D$  and let  $\gamma$  be a path in  $\Sigma$  from  $a$  to some point  $b \in \Sigma$ . Then a meromorphic continuation of  $(D, f)$  along the path  $\gamma$  is a finite sequence of direct meromorphic continuations  $(D, f) \sim (D_1, f_1) \sim \dots \sim (D_m, f_m)$  such that:

1. each region  $D_i$  is an open disc in  $\Sigma$ , with  $a \in D_1 \subseteq D$ ,
2. there exists a subdivision  $0 = s_0 < s_1 < \dots < s_m = 1$  of the interval  $I$  such that  $\gamma([s_{i-1}, s_i]) \subseteq D_i$  for  $i = 1, \dots, m$ , see Fig. 2.3.

**Theorem 2.3.** Let  $(D, f) \sim (D_1, f_1) \sim \dots \sim (D_m, f_m)$  and  $(D, f) \sim (E_1, g_1) \sim \dots \sim (E_n, g_n)$  be meromorphic continuation of  $(D, f)$  along a path  $\gamma$  from  $a$  to  $b$  and let  $0 = s_0 < s_1 < \dots < s_m = 1, 0 = t_0 < t_1 < \dots < t_n = 1$  be the corresponding subdivisions of  $I$ . Then  $(D_i, f_i) \sim (E_j, g_j)$  whenever  $[s_{i-1}, s_i] \cap [t_{j-1}, t_j] \neq \emptyset$ , and in particular  $f_m(b) = g_n(b)$ .

If a function element  $(D, f)$  can be continued meromorphically along a path  $\gamma$  from  $a$  to  $b$ , then by Theorem 2.3 the value  $f_\gamma(b)$  of the resulting continuation at

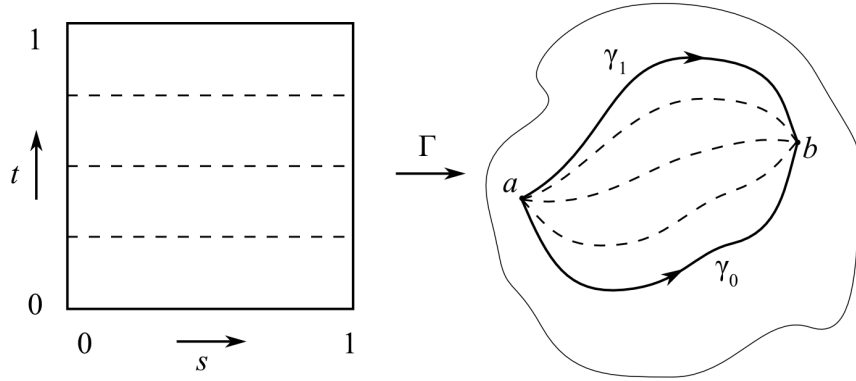


**Figure 2.4:** The figure shows an example of homotopy between two paths  $\gamma_0$  and  $\gamma_1$  [JS87].

$b$  is independent of the method of continuation along  $\gamma$ . However, different paths  $\gamma_0$  and  $\gamma_1$  from  $a$  to  $b$  may give different value of  $f$  at  $b$ . The following definition shows terms for paths  $\gamma_0$  and  $\gamma_1$ , that provide the equation  $f_{\gamma_0}(b) = f_{\gamma_1}(b)$  to be satisfied.

**Definition 2.10.** If  $\gamma_0$  and  $\gamma_1$  are paths from  $a$  to  $b$  in a topological space  $X$ , then  $\gamma_0$  and  $\gamma_1$  are homotopic in  $X$  (written  $\gamma_0 \simeq \gamma_1$ ), if there is a continuous function  $\Gamma: I^2 \rightarrow X$  such that

$$\Gamma(s, 0) = \gamma_0(s), \tag{2.6}$$

$$\Gamma(s, 1) = \gamma_1(s), \tag{2.7}$$

$$\Gamma(0, t) = a \text{ and} \tag{2.8}$$

$$\Gamma(1, t) = b \tag{2.9}$$

for all  $s, t \in I$ . The relation  $\simeq$  is an equivalence relation and the equivalence classes are called homotopy classes.

Thus, for each  $t \in I$  we have a path  $\gamma_t$  from  $a$  to  $b$  in  $X$  given by  $\gamma_t(s) = \Gamma(s, t)$ . As  $t$  increases from 0 to 1,  $\gamma_t$  is continuously deformed within  $X$  from  $\gamma_0$  to  $\gamma_1$ , keeping the end-points fixed at  $a$  and  $b$ , as shown in Fig. 2.4.

**Theorem 2.4.** Let  $X \subseteq \Sigma$ ,  $a, b \in X$  and let  $\Gamma$  be a homotopy in  $X$  between two paths  $\gamma_0$  and  $\gamma_1$  from  $a$  to  $b$  in  $X$ . If  $(D, f)$  is a function element which can be continued meromorphically along each path  $\gamma_t: s \mapsto \Gamma(s, t)$ , then the meromorphic functions at  $b$ , resulting from the continuations along  $\gamma_0$  and  $\gamma_1$ , are identically equal in some neighborhood of  $b$ , and in particular  $f_{\gamma_0}(b) = f_{\gamma_1}(b)$ .

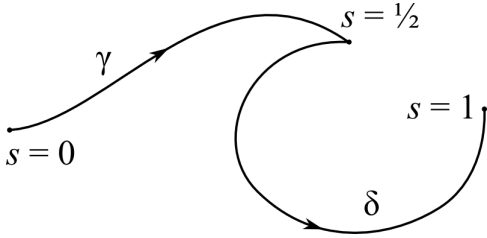


**Figure 2.5:** The figure depicts product  $\gamma\delta$  of paths  $\gamma$  and  $\delta$  [JS87].

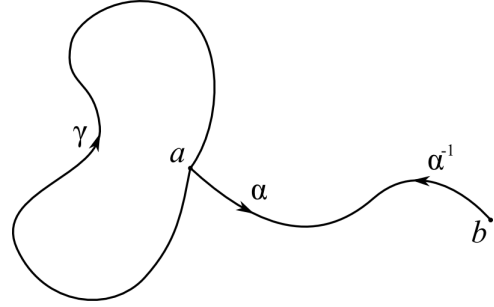


**Figure 2.6:** Example of a composition of two paths  $\alpha^{-1}\gamma\alpha$  with start and end at the point  $b$  [JS87].

**Definition 2.11** (Null homotopy). For each  $a \in X$  let  $\gamma_{(a)}$  denote the constant path  $\gamma_{(a)}(s) = a$  for all  $s \in I$ . Then, a closed path  $\gamma$  from  $a$  to  $a$  in  $X$  is said to be null-homotopic if  $\gamma \simeq \gamma_{(a)}$ .

The topology space  $X$  is said to be simply connected, if it is path-connected and all closed paths in  $X$  are null-homotopic. For example,  $\mathbb{C}$  is simply connected. Indeed, if  $\gamma$  is any closed path from  $a$  to  $a$  in  $\mathbb{C}$ , then there is a homotopy  $\Gamma: \gamma \simeq \gamma_{(a)}$  given by  $\Gamma(s, t) = \gamma(s) + t(a - \gamma(s))$ . On the other hand,  $\mathbb{C} \setminus \{0\}$  is not simply connected.

**Theorem 2.5.** A topological space  $X$  is simply connected iff for each pair of points  $a, b \in X$  there is a single homotopy class of paths from  $a$  to  $b$  in  $X$ .

**Theorem 2.6** (The monodromy theorem). Let  $E \subseteq \Sigma$  be a simply connected region, and let  $(D, f)$  be a function element with  $D \subseteq E$ . If  $(D, f)$  can be continued meromorphically along all paths in  $E$  starting at some point  $a \in D$ , then there is a direct meromorphic continuation  $(E, g) \sim (D, f)$ .

Using homotopy, we can associate to each path-connected space  $X$  a group  $\pi_1(X)$ , the fundamental group of  $X$ . The following text leads us to the definition of the fundamental group.

**Definition 2.12.** If  $\gamma$  and  $\delta$  are paths in a topological space  $X$  with  $\gamma(1) = \delta(0)$ , then the product  $\gamma\delta$  of  $\gamma$  and  $\delta$  is the path

$$(\gamma\delta)(s) = \begin{cases} \gamma(2s) & \text{for } 0 \leq s \leq 1/2 \\ \delta(2s - 1) & \text{for } 1/2 \leq s \leq 1, \end{cases} \quad (2.10)$$

shown in Fig. 2.5.



**Definition 2.13.** The inverse path of  $\gamma$  is path  $\gamma^{-1}(s) = \gamma(1-s)$ , where  $s \in [0, 1]$ .

The homotopy classes  $[\gamma]$  of closed paths  $\gamma$  from a given point  $a \in X$  to itself form a group  $\pi_1(X, a)$ . The product  $[\gamma][\delta]$  of two classes is the class  $[\gamma\delta]$ , the identity element is the class containing the constant path  $\gamma_{(a)}(s) = a$  for all  $s \in [0, 1]$ , and the inverse of  $[\gamma]$  is  $[\gamma^{-1}]$ . These definitions of group operations are independent of the choice of representatives  $\gamma, \delta$ .

If  $X$  is path-connected, then there is a path  $\alpha$  from any point  $a \in X$  to any point  $b \in X$ , see Fig. 2.6. The map  $[\gamma] \rightarrow [\alpha^{-1}\gamma\alpha]$  is an isomorphism  $\pi_1(X, a) \cong \pi_1(X, b)$ . Thus as an abstract group,  $\pi_1(X, a)$  is independent of the choice of  $a \in X$ , so we denote this group  $\pi_1(X)$ , the fundamental group of  $X$ .

For example,  $X$  is simply connected iff the fundamental group  $\pi_1(X)$  is the trivial group. An important example of a space which is not simply connected is the punctured plane, i.e. plane without single point.

**Theorem 2.7.** The fundamental group  $\pi_1(\mathbb{C} \setminus \{0\})$  is an infinite cyclic group, generated by  $[\gamma]$ , where  $\gamma$  is the unit circle parametrised by  $\gamma(s) = e^{2\pi is}$ ,  $s \in [0, 1]$ .

More generally, if  $a \in \mathbb{C}$ , then  $\pi_1(\mathbb{C} \setminus \{a\})$  is infinite cyclic, generated by  $[\gamma + a]$ , where  $\gamma + a$  is the closed path  $(\gamma + a)(s) = e^{2\pi is} + a$ .

We define the winding number  $n_a(\delta)$  of a closed path  $\delta$  around  $a$  to be the unique integer  $n \in \mathbb{Z}$  such that  $\delta \simeq (\gamma + a)^n$  in  $\mathbb{C} \setminus \{a\}$ , where  $\gamma$  is the path from the Theorem 2.7.

## 2.4 Examples

**Example 2.4** (The Riemann surface of  $f(z) = \log(z)$ ). The function  $\log(z)$  belongs to the family of multi-valued functions. Therefore a problem arises, if we want to use such simple statement as  $\log(ab) = \log(a) + \log(b)$ . The solution was to restrict attention to the principal value of  $\log(z)$ , denoted as

$$\text{Log}(z) = \ln(|z|) + i \arg(z) \tag{2.11}$$

for each  $z \neq 0$ , where  $-\pi < \arg(z) \leq \pi$  and  $\ln(|z|)$  is the unique real value of  $\log(|z|)$ . This is not completely satisfactory, since  $\text{Log}(z)$  is not continuous when

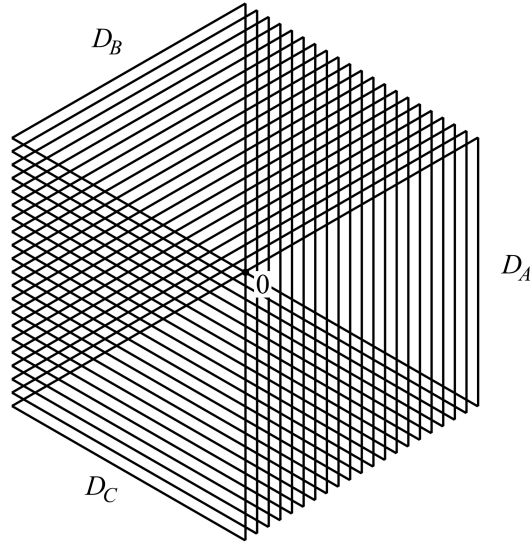


**Figure 2.7:** Half-planes in  $\mathbb{C}$  used by the analytic continuation of logarithm induced by intervals  $A = (-\pi/2, \pi/2)$ ,  $B = (\pi/6, 7\pi/6)$  and  $C = (5\pi/6, 11\pi/6)$  [JS87]. Another example of regions used by creation of the direct meromorphic continuation can be found in Fig. 2.2.

$z \in \mathbb{R} \ z < 0$ , and we still cannot assume that  $\text{Log}(ab) = \text{Log}(a) + \text{Log}(b)$  for all  $a, b \neq 0$ , since the two sides may differ by  $\pm 2\pi i$ . However, as  $e^{2\pi i} = 1$  we have

$$ab = e^{\text{Log}(ab)} = e^{\text{Log}(a) + \text{Log}(b)} \quad (2.12)$$

for all  $a, b \neq 0$ .

A better solution, which applies to many-valued functions in general, is due to Riemann: instead of restricting the values of the function, we extend its domain. Specifically, we construct a surface  $S$ , a covering map  $\psi: S \rightarrow \mathbb{C} \setminus \{0\}$  and a function  $\phi: S \rightarrow \mathbb{C}$  such that for each  $z \in \mathbb{C} \setminus \{0\}$  the elements of  $\psi^{-1}(z)$  are mapped bijectively by  $\phi$  onto the different values of  $\log(z)$ , so that  $e^z \circ \phi = \psi: S \rightarrow \mathbb{C} \setminus \{0\}$ . Thus each sheet of  $S$  corresponds to a particular branch of  $\log(z)$  represented by the restriction of  $\phi$  to the sheet. We may regard  $\phi$  as composition of all the different branches of  $\log(z)$ .

Let  $J$  be an open interval  $J = (\alpha, \beta) = \{\theta \in \mathbb{R} \mid \alpha < \theta < \beta\}$ , where  $\alpha < \beta \leq \alpha + 2\pi$ , let  $D_J = \{z = re^{i\theta} \mid r > 0 \text{ and } \theta \in J\}$ , and for each such  $z \in D_J$ , let  $f_J(z) = \ln(r) + i\theta$ . Since  $J$  has length at most  $2\pi$ , each  $z \in D_J$  determines a unique  $\theta = \arg(z) \in J$ , so  $f_J$  is single-valued on  $D_J$ .

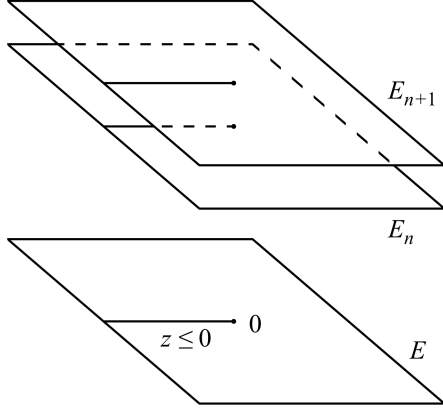


**Figure 2.8:** Visualization of the copies of  $E_n$ , which represent the domains of the branches of the function  $f_n$  [JS87].

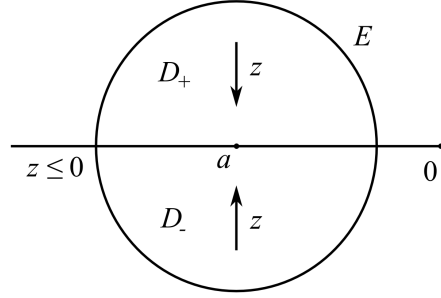


**Figure 2.9:** An example of function element  $(D, f)$ , containing the point  $a$  on the half-line  $z \leq 0$ ,  $z \in \mathbb{R}$ , is depicted [JS87].

The surface  $S$ , known as the Riemann surface of  $\log(z)$ , can be constructed from the sequence of direct analytic continuations

$$\dots \sim L_{(\Theta_C(-2\pi))} \sim L_A \sim L_B \sim L_C \sim L_{(\Theta_A(2\pi))} \sim \dots, \quad (2.13)$$

where  $L_J = (D_J, f_J)$ ,  $J \in \{A, B, C\}$  is the function element that represents one branch of the function  $\log(z)$  on the region  $D_J$ ,  $J \in \{A, B, C\}$  and  $\Theta_J(s): (\alpha, \beta) \mapsto (\alpha + s, \beta + s)$ . Let  $D_A, D_B, D_C$  be the open half-planes corresponding to the intervals  $A = (-\pi/2, \pi/2)$ ,  $B = (\pi/6, 7\pi/6)$  and  $C = (5\pi/6, 11\pi/6)$ , see Fig. 2.7. Let  $L_A, L_B$  and  $L_C$  be the corresponding branches of  $\log(z)$ . Now  $D_A \cap D_B \neq \emptyset$ , and for  $z = re^{i\theta} \in D_A \cap D_B$ , we have  $\theta \in A \cap B = (\pi/6, \pi/2)$ , so  $f_A(z) = \ln(r) + i\theta = f_B(z)$  and hence  $L_A \sim L_B$ . A similar argument shows that  $L_B \sim L_C$ . Although  $D_A \cap D_C \neq \emptyset$  we do not have  $L_A \sim L_C$ . The elements of  $D_A \cap D_C$  are of the form  $z = re^{i\theta}$  with  $\theta \in e^{i(\theta+2\pi)}$  with  $\theta + 2\pi \in (3\pi/2, 11\pi/6) \subset C$ , so  $f_C(z) = \ln(r) + i(\theta + 2\pi) = f_A(z) + 2\pi i$ . Thus, analytic continuation of  $f_C$  onto half-plane  $D_A$  produces the function element  $(D_A, f_A + 2\pi) = L_{(\Theta_A(2\pi))}$ , where  $(\Theta_A(2\pi i))$  is the interval shift  $\{\theta + 2\pi \mid \theta \in A\} = (3\pi/2, 5\pi/2)$ .

The surface  $S$ , known as the Riemann surfaces of  $\log(z)$ , can be constructed from the sequence of direct analytic continuations  $\dots \sim L_{(\Theta_C(-2\pi))} \sim L_A \sim L_B \sim L_C \sim L_{(\Theta_A(2\pi))} \sim \dots$ . The general idea is to regard the underlying regions of these function elements as being disjoint, and then to glue them together wherever they carry identical equal values of  $\log(z)$ . The resulting surface  $S$  is the domain of a single-valued function  $\phi$ , which is locally equal to a branch of  $\log(z)$ .

Let us show second, equivalent way of constructing  $S$  which can be adapted to other functions as well. If we cut  $\Sigma$  along the line  $z \leq 0$  from 0 to  $\infty$ , then the

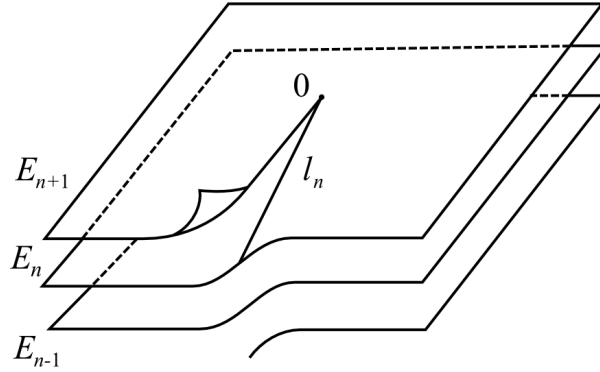


**Figure 2.10:** A cut-out of the Riemann surface of the function  $\log z$ . The surface was created by the union of the sheets  $E_n$  and the open half-lines  $l_n$  [JS87].

remaining region  $E = \mathbb{C} \setminus \{z \in \mathbb{R} \mid z \leq 0\}$  is simply connected and is the domain of branches  $f_n(z)$  of  $\log(z)$  satisfying  $f_n(1) = 2n\pi i$ , for each  $n \in \mathbb{Z}$ . We take disjoint copies  $E_n$  of  $E$ , each the domain of  $f_n$ . We can think of these surfaces  $E_n$  as lying one above the other over  $E \subset \mathbb{C}$ , see Fig. 2.8.

Now let  $(D, f)$  be a function element representing a branch of  $\log(z)$  on some disc  $D$  containing a point  $a \in \mathbb{R}$ ,  $a < 0$ , see Fig. 2.9. On the region  $D_+ = \{z \in D \mid \Im(z) > 0\}$ , we have  $f \equiv f_n$  for some  $n \in \mathbb{Z}$ , and on the region  $D_- = \{z \in D \mid \Im(z) < 0\}$ , we have  $f \equiv f_m$  for some  $m \in \mathbb{Z}$ . As  $z \rightarrow a$  with  $z \in D_+$ , we have

$$f(z) = f_n(z) \rightarrow \ln(|a|) + (2n + 1)\pi i \quad (2.14)$$

while as  $z \rightarrow a$  with  $z \in D_-$ , we have

$$f(z) = f_m(z) \rightarrow \ln(|a|) + (2m - 1)\pi i. \quad (2.15)$$

Since  $f$  is analytic at  $a$ ,  $f(z)$  has a unique limit as  $z \rightarrow a$ , so  $m = n + 1$ . As we cross the cut  $z \leq 0$  at any point  $a < 0$ , passing from  $D_+$  to  $D_-$ , the analytic continuation takes us from  $f_n$  on  $D_+$  to  $f_m = f_{n+1}$  on  $D_-$ . We therefore join the edge  $\Im(z) > 0$ ,  $z \in \mathbb{R}$  of  $E_n$  to the edge  $\Im(z) < 0$ ,  $z \in \mathbb{R}$  of  $E_{n+1}$  along a half-line  $l_n$  from 0 to  $\infty$ , but not including 0 or  $\infty$ , because they are the singular points of the function  $\log(z)$  (if we move along a circle with center in 0 and radius  $r \in \mathbb{R}$ , the value of  $\log(z)$  goes from 0 to  $2\pi i$ ). We now define the surface  $S$  to be the union of all these sheets  $E_n$  and half-lines  $l_n$ , for  $n \in \mathbb{Z}$ , see Fig. 2.10.

**Example 2.5** (The Riemann surface of  $f(z) = z^{1/q}$ ,  $q \in \mathbb{N}$ ). We can adapt the method of construction of the Riemann surface of  $\log(z)$  to obtain the Riemann surface of  $z^{1/q}$ . Recall, that the function  $f_n$  match the branch of the function  $\log(z)$  from the Example 2.4. Let  $E = \mathbb{C} \setminus \{z \in \mathbb{R} \mid z \leq 0\}$ . This simply

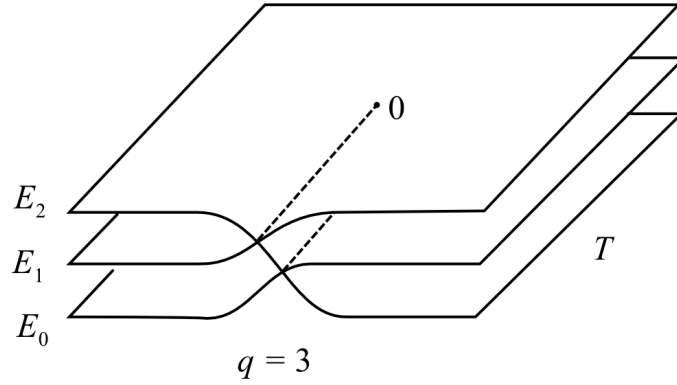


**Figure 2.11:** Riemann surface of  $f(z) = z^{1/3}$ . Notice the self-intersection caused by the connection of  $E_2$  and  $E_0$  [JS87].

connected region is the domain of the branches  $g_n = e^{q^{-1}f_n}$  of  $z^{1/q}$  satisfying  $g_n(1) = \epsilon^n$ , where  $\epsilon = e^{2\pi i/q}$  and  $n \in \mathbb{N}$ . We have  $g_m = g_n$  iff  $m \equiv n \pmod{q}$ , so there are  $q$  distinct branches  $g_0, g_1, \dots, g_{q-1}$  and we therefore take  $q$  disjoint copies  $E_0, E_1, \dots, E_{q-1}$  of  $E$  lying at different levels above  $E$ , with each  $E_n$  the domain of  $g_n$ ,  $n = 0, 1, \dots, q - 1$ .

As we continue analytically across the line  $z \leq 0$  with  $\Im(z)$  decreasing, we pass from  $g_0$  to  $g_1$ , so we join the edge  $\Im(z) > 0$  of  $E_0$  to the edge  $\Im(z) < 0$  of  $E_1$  along a line  $l_0$  from 0 to  $\infty$ . Similarly, we join  $E_1$  to  $E_2$  along  $l_1$  and so on until  $E_{q-2}$  is joined to  $E_{q-1}$  along  $l_{q-2}$ . The process so far, giving us a spiral-shaped surface with  $q$  sheets, is easily visualized. In the last step, we join the edge  $\Im(z) > 0$  of  $E_{q-1}$  to the edge  $\Im(z) < 0$  of  $E_0$  along a line  $l_{q-1}$ , which cannot be done without self-intersection in  $\mathbb{R}^3$ . Example for  $q = 3$  can be seen in Fig. 2.11.

**Example 2.6** (The Riemann surface of  $f(z) = \sqrt{z - a}$ ). Let  $p(z) = z - a$ . This is the general case in which  $p$  has degree 1 and we have already considered the special case  $a = 0$  in the previous example. Since the substitution  $z \mapsto z - a$  is an automorphism of  $\Sigma$ , we must expect the general case to resemble the special case.

If we cut  $\Sigma$  along a closed half-line  $l$  from  $a$  to  $\infty$ , then the resulting region  $E = \Sigma \setminus l$  is simply connected and it contains no zeros of  $p(z) = z - a$ , so by the monodromy Theorem 2.6, we have single-valued analytic branches  $f_1, f_2$  of  $\sqrt{p}$  on  $E$ , satisfying  $f_1 \equiv -f_2$ . We therefore take two copies  $E_1, E_2$  of  $E$ , the domains of  $f_1$  and  $f_2$  respectively. If we continue  $f_1$  analytically across  $l$ , then we obtain  $f_2$ , so we join the two edges of  $E_1$  to the opposite edges of  $E_2$  along lines  $l_1$  and  $l_2$ , lying above  $l$  see Fig. 2.12. Finally, we include branch-points  $s_a, s_\infty$  lying above  $a, \infty$  to obtain a two-sheeted branched covering surface  $S = T \cup \{s_a, s_\infty\}$  of  $\Sigma$

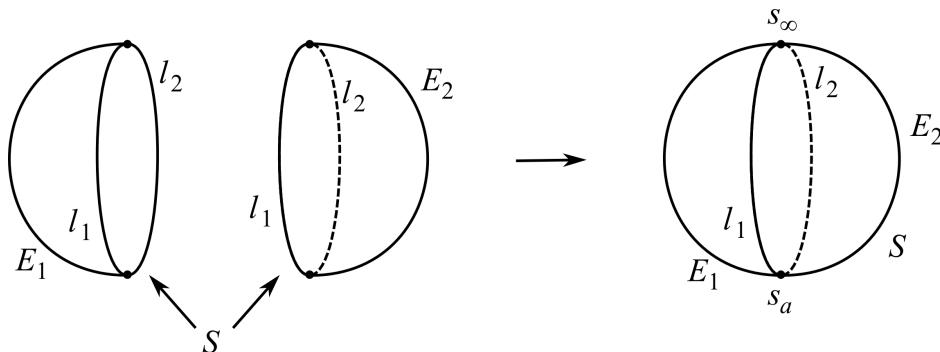


**Figure 2.12:** The Riemann surface of  $f(z) = \sqrt{z-a}$  [JS87].

**Example 2.7** (The Riemann surface of  $f(z) = \sqrt{(z-a)(z-b)}$ ,  $a \neq b$ ). If we cut  $\Sigma$  along a closed line segment  $l$  from  $a$  to  $b$ , then the resulting region  $E = \Sigma \setminus l$  is simply connected. We can continue  $\sqrt{p}$  meromorphically along all paths in  $E$ . Analytic continuation in  $E \cap \mathbb{C}$  is straightforward, and if  $\infty \in E$ , then each branch of  $\sqrt{p}$  is meromorphic at  $\infty$  since each branch of  $z\sqrt{(p(1/z))} = \sqrt{((1-az)(1-bz))}$  is analytic and non-zero at 0. As before, we may therefore use the monodromy theorem to show that there are two single-valued meromorphic branches  $f_1$  and  $f_2$  of  $f(z) = \sqrt{(z-a)(z-b)}$  on  $E$ , each having a simple pole at  $\infty$ . We therefore take two copies  $E_1$  and  $E_2$  of  $E$ , with  $E_n$  lying above  $E$ , and regard  $E_n$  as the domain of  $f_n$ ,  $n = 1, 2$ . By crossing  $l$  in either direction, we pass from one branch to the other, so we join  $E_1$  and  $E_2$  together along lines  $l_1, l_2$ , lying above  $l$ , to obtain a two-sheeted unbranched covering surface  $T = E_1 \cup E_2 \cup l_1 \cup l_2$  of  $\Sigma \setminus \{a, b\}$ . Finally, we include branch-points  $s_a, s_b$  lying above  $a, b$  to obtain a two-sheeted branched covering surface  $S = T \cup \{s_a, s_b\}$  of  $\Sigma$ . As in example 2.6, the Riemann surface  $S$  is homeomorphic to a sphere.

**Example 2.8** (Riemann surface of  $f(z) = \sqrt{p(z)}$ ,  $p$  is a polynomial). In general case, we can visualize Riemann surfaces  $\mathcal{S}$  of  $\sqrt{p(z)}$ , where  $p(z) = \prod_{j=1}^m (z-a_j)^{b_j}$  is a polynomial and  $a_1, \dots, a_m$  are all distinct. If the multiplicities  $b_j$  of the roots  $a_j$  of  $p$  are all even, there are two single-valued meromorphic branches  $f_1(z) = \prod_{j=1}^m (z-a_j)^{b_j/2}$  and  $f_2(z) = -f_1(z)$  of  $\sqrt{p}$ , so the Riemann surface  $\mathcal{S}$  of  $\sqrt{p}$  is a disjoint union of two spheres, each being a domain of the branch  $f_i$ ,  $i = 1, 2$ . The Riemann surface  $\mathcal{S}$  of  $\sqrt{p}$  consists of two sheets  $E_1$  and  $E_2$ , the domains of  $f_1, f_2$  respectively. Since we cannot pass from one branch to another by a meromorphic continuation of  $\sqrt{p}$ , we do not join  $E_1$  and  $E_2$ , but instead, we regard the surface  $\mathcal{S}$  as a 2-sheeted unbranched covering surface of  $\Sigma$  consisting of two disjoint spheres.

---

## 2. RIEMANN SURFACES

Hence, we assume that the multiplicity  $b_j$  of some root  $a_j$  of  $p$  is odd. We write  $\sqrt{p} = q\sqrt{r}$ , where  $q$  and  $r$  are polynomials, and  $r$  is non-constant and square-free. Since  $q$  is a single-valued and meromorphic on  $\Sigma$ , the construction of the Riemann surface of  $\sqrt{p}$  is homeomorphic to that of  $\sqrt{r}$ . That means, the crossing of the layers and the position of branch points are topologically same. Replacing  $p$  by  $r$ , we may assume that  $p$  has distinct roots and it is not constant, i.e.  $m \geq 1$  and each  $b_j = 1$ .

If  $m$  is even ( $m = 2k$ ),  $a_1, \dots, a_m$  are the only branch points, but if  $m$  is odd ( $m = 2k - 1$ ), there is a branch point lying over  $a_{2k} = \infty$ . In either case, there is an even number of branch points over  $a_1, \dots, a_{2k}$ , so we cut  $\Sigma = \mathbb{C} \cup \{\infty\}$  along simple mutually disjoint paths from  $a_1$  to  $a_2$ ,  $a_3$  to  $a_4, \dots, a_{2k-1}$  to  $a_{2k}$  and one gets a region  $E$ . The Riemann surface  $\mathcal{S}$  can be formed by taking  $E_1, E_2$ , each being a domain of a meromorphic branch of  $\sqrt{p}$ , and joining  $E_1$  to  $E_2$  along lines lying above the  $k$  cuts in  $\Sigma$ . This gives a 2-sheeted surface  $\mathcal{S}$  of  $\Sigma$ , homeomorphic to a sphere with  $k - 1$  handles attached [JS87].

The function  $\sqrt{p(z)}$  has two branches, as the polynomial  $p(z)$  is a single-valued function and the second root is a 2-valued function. In the first step, we created two approximations of the unit sphere with center at the origin  $(0, 0, 0)$  parameterized as  $\mathbb{S}^2 = \{(\cos(t)\cos(u), \cos(t)\sin(u), \sin(t)) \mid t \in [-\frac{\pi}{2}, \frac{\pi}{2}], u \in [0, 2\pi]\}$ .

**Example 2.9** (Riemann surface of  $f(z) = \sqrt{(1 + \sqrt{z})}$ ). In the previous example, all the sheets come together at each branch-point of the Riemann surface. Let us see another example, that shows a different situation.

The four-valued function  $f(z) = \sqrt{1 + \sqrt{z}}$ ,  $z \in \mathbb{C}$ . This function has four analytical branches on  $E = \Sigma \setminus \{0, 1, \infty\}$ . For each  $z \in \mathbb{C} \setminus 0$ , there are two distinct values  $\zeta = \sqrt{z}$  and each such value determines two values for  $f(z) = \sqrt{1 + \zeta}$ . If one chooses  $\alpha$  to be the positive value  $+\sqrt{1/2}$  of  $\sqrt{1/2}$ , then one can label the branches  $f_1, \dots, f_4$  of  $f$  near  $z = 1/2$  and the branches take the distinct values  $+\sqrt{1 + \alpha}$ ,  $+\sqrt{1 - \alpha}$ ,  $-\sqrt{1 + \alpha}$  and  $-\sqrt{1 - \alpha}$  respectively at  $z = 1/2$ .

If one extends  $f_1$  analytically along a closed path  $\gamma$  containing  $1/2$  with the value  $n_\gamma(0) = 1$  and  $n_\gamma(1) = 0$  (say  $\gamma(s) = 1/2e^{2\pi is}$ ,  $s \in [0, 1]$ ), then the value  $1 + \zeta$  is transformed from the point  $+\sqrt{1 + \alpha} = f_1(1/2)$  to  $+\sqrt{1 - \alpha} = f_2(1/2)$ , see Fig. 2.14. Thus the analytical continuation around 0 transforms  $f_1$  to  $f_2$ , and similarly  $f_2$  to  $f_1$ ,  $f_3$  to  $f_4$ , and  $f_4$  to  $f_3$ . So, these four branches are permuted using two disjoint inversions. Therefore, we join the corresponding sheets  $E_1$  to  $E_2$ , and  $E_3$  to  $E_4$  at two branch points above 0, so that  $z \in \Sigma$  rotating once around 0, each point  $s \in \psi^{-1}(z)$  above  $z$  moves from  $E_1$  to  $E_2$ , or  $E_2$  to  $E_1$ , etc. (see Fig. 2.13(a)). Thus  $\psi^{-1}(0)$  consists of two points, each branch point of order 1 since it joins two sheets.

2. RIEMANN SURFACES

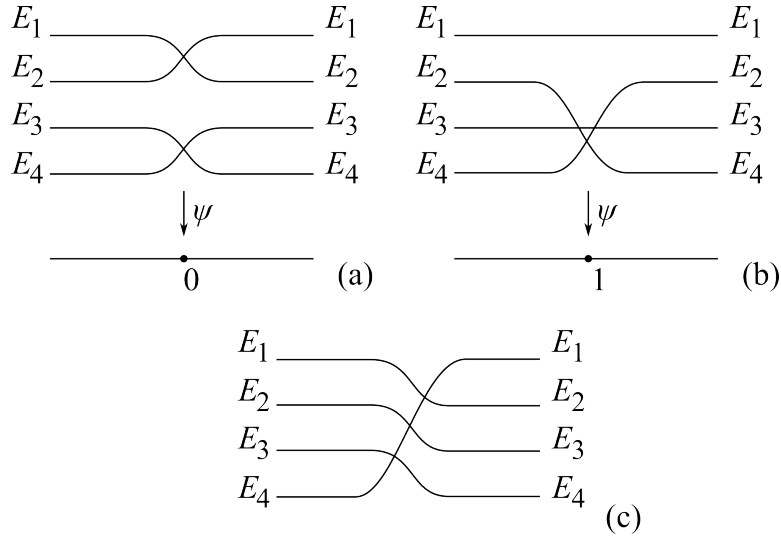


**Figure 2.13:** The crossing of the layers of the function  $f(z) = \sqrt{1 + \sqrt{z}}$  in the neighborhood of the point (a) 0 (b) 1 (c)  $\infty$  [JS87].

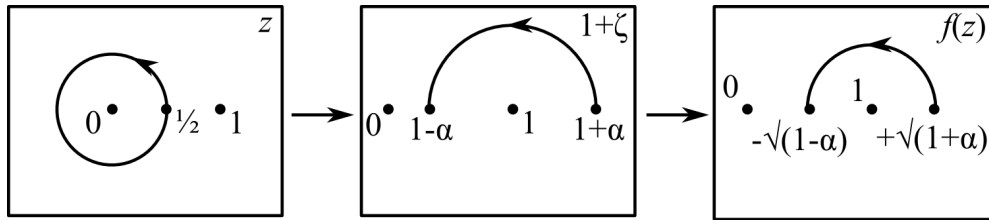


**Figure 2.14:** Image of the closed path  $\gamma$  winding once around 0 transformed by the function  $f(z) = \sqrt{1 + \sqrt{z}}$  [JS87].

On the other hand, if one proceeds analytically along a closed path  $\delta$  winding once around 1 but not around 0 (say  $\gamma(s) = 1/2e^{2\pi is} + 1, s \in [0, 1]$ ), then  $1 + \zeta$  is transformed from  $1 + \alpha$  to  $1 + \alpha$  along a path which does not wind around 0, so  $f_1$  and  $f_3$  (the branches of  $\sqrt{1 + \zeta}$ ) are invariant, however,  $1 - \zeta$  winds once around 0 from  $1 - \alpha$  back to  $1 - \alpha$ , so  $f_2$  and  $f_4$  (the branches of  $\sqrt{1 - \zeta}$ ) are interchanged, see Fig. 2.15. Hence, the sheets  $E_2$  and  $E_4$  are joined at a branch point of order 1 over  $z = 1$ , while the sheets  $E_1$  and  $E_3$ , which carry analytical branches at  $z = 1$ , are unbranched. In this case,  $\psi^{-1}(1)$  consists of three points: one branch point, where  $E_2$  and  $E_4$  meet, and two points on  $E_1$  and  $E_3$  where  $S$  is not branched, see Fig. 2.13(b).

Finally, suppose that we continue analytically along a closed path  $\epsilon$  winding once around  $\infty$  in  $\Sigma$ . As a path in  $\mathbb{C}$ ,  $\epsilon$  winds once around both 0 and 1. Both paths,  $\gamma$  and  $\delta$ , follow the positive orientation of  $\mathbb{C}$ , and by stereographic projection this induces orientation of  $\mathbb{S}^2$  and hence of  $\Sigma$ . For  $\epsilon$  to be consistent



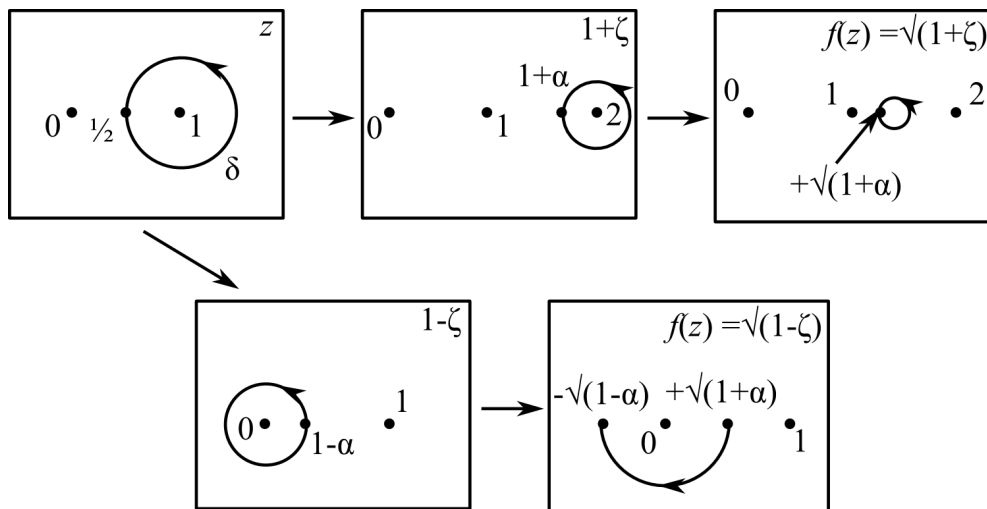


**Figure 2.15:** Image of the closed path  $\delta$  winding once around 1 but not around 0 transformed by function  $f(z) = \sqrt{1 + \sqrt{z}}$  [JS87].

with this orientation of  $\Sigma$  at  $\infty$ , we need its projection  $\pi^{-1}(\epsilon)$  to be consistent with the orientation of  $\mathbb{S}^2$  at  $N = (0, 0, 1)$ , so  $\epsilon$  must follow the negative orientation of  $\mathbb{C}$ . For example, if we take path in  $E = \Sigma \setminus \{0, 1, \infty\}$  homotopic to  $\delta^{-1}\gamma^{-1}$ , the permutation of the branches induced by continuation around  $\infty$  is equal to the composition of the two permutations induced by continuation along  $\delta^{-1}$  and  $\gamma^{-1}$ , in this order. Thus, as shown in Fig. 2.13(c), the four sheets  $E_1, \dots, E_4$  are joined at a single branch point of order 3 over  $\infty$ , in the same way as the four sheets of the Riemann surface of  $z^{1/4}$  are joined at  $\infty$ . This is because  $f(z) = \sqrt{1 + \sqrt{z}}$  behaves like  $z^{1/4}$  for large  $|z|$ .

## 2.5 The genus of a compact Riemann surface

If  $A(z, w) = 0$  is an irreducible algebraic equation, then its Riemann surface  $S = \mathcal{S}_A$  is a compact, connected and orientable surface. Such surfaces are classified topologically by the following result.

**Theorem 2.8.** Each compact, connected, orientable surface is homeomorphic to a surface  $S_g$  formed by attaching  $g$  handles to a sphere, for some unique integer  $g \geq 0$  [Mas67].

We call  $g$  the genus of the surface. In this section, we give a method for calculating  $g$ , using polygonal subdivisions. A polygonal subdivision  $M$  of a

---

## 2. RIEMANN SURFACES

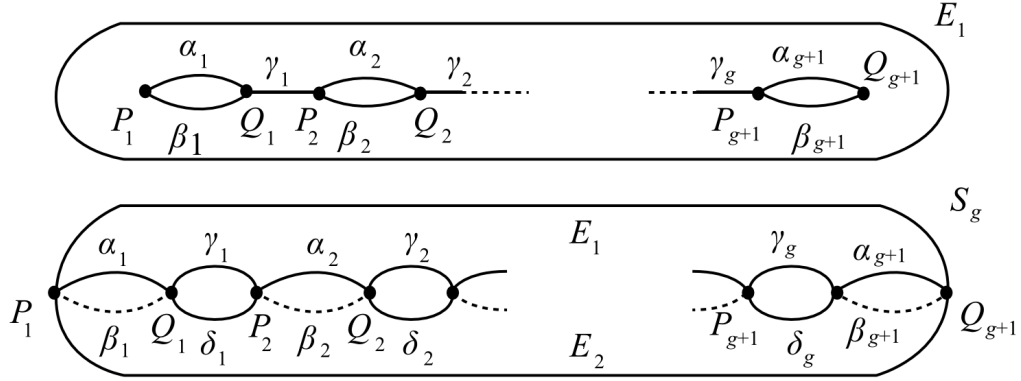


**Figure 2.16:** The construction of the Riemann surface  $S_g$  as the union of two cut spheres  $E_1$  and  $E_2$ . The cut sphere  $E_2$  looks analogue to the  $E_1$  [JS87].

surface  $S$  consists of a finite set of points of  $S$ , called vertices, and a finite set of simple paths on  $S$ , called edges, such that

1. every edge has two end-points, these points being vertices;
2. edges can intersect only at their end-points;
3. the union of the edges (which is denoted by  $M$ ) is connected;
4. the components of the complement  $S \setminus M$  are homeomorphic to open discs (the components are called faces).

It can be shown, that every compact, connected surface has a polygonal subdivision, proof can be found in [Spr57].

We define the Euler characteristic of a compact, connected surface  $S$  to be

$$\xi(S) = \xi(M) = V - E + F, \quad (2.16)$$

where  $M$  is a polygonal subdivision of  $S$  with  $V$  vertices,  $E$  edges and  $F$  faces. Homeomorphic surfaces have the same Euler characteristic, therefore we can show that  $\xi(S)$  is well defined, that is, independent of the choice of  $M$ .

We can now calculate the Euler characteristic  $\xi(S_g)$  of a compact, connected, orientable surface  $S_g$  of genus  $g$ . We do this by using a polygonal subdivision of  $S_g$  based on the construction of the Riemann surface  $S$ , as the union of two cut spheres  $E_1$  and  $E_2$ .

## 2. RIEMANN SURFACES

---

**Theorem 2.9.** The Euler characteristic of a compact, connected, orientable surface  $S_g$  of genus  $g$  is given by  $\xi(S_g) = 2 - 2g$ .

*Proof.* We take  $g + 1$  cuts  $P_1Q_1, \dots, P_{g+1}Q_{g+1}$  on each of the two spheres, with edges labelled  $\alpha_1, \beta_1, \dots, \alpha_{g+1}, \beta_{g+1}$  in each case. We connect the cuts by edges  $Q_1P_2, \dots, Q_gP_{g+1}$  labelled  $\gamma_1, \dots, \gamma_g$  on  $E_1$  and  $\delta_1, \dots, \delta_g$  on  $E_2$ , and then join  $E_1$  and  $E_2$  along the edges  $\alpha_i$  and  $\beta_i$  to give a surface  $S_g$  of genus  $g$ , see Fig. 2.16. The vertices  $P_1, Q_1, \dots, P_{g+1}, Q_{g+1}$  and the edges  $\alpha_1, \dots, \alpha_{g+1}, \beta_1, \dots, \beta_{g+1}, \gamma_1, \dots, \gamma_g, \delta_1, \dots, \delta_g$  form a polygonal subdivision of  $S_g$  with two faces  $E_1$  and  $E_2$ , so  $V = 2g + 2$ ,  $E = 4g + 2$  and  $F = 2$ , giving  $\xi(S_g) = V - E + F = 2 - 2g$ .  $\square$

## 3

# Visualization methods

To visualize a real function  $f: \mathbb{R} \rightarrow \mathbb{R}$ , we draw a graph  $y = f(x)$  in a two dimensional Cartesian coordinate system in  $\mathbb{R}^2$  via identifying one axis with the domain of the function and the other axis with its codomain. This method meets with some difficulties when we want to extend it to a complex function  $g: \mathbb{C} \rightarrow \mathbb{C}$ . The main problem arising is that  $\mathbb{C}$  has real dimension 2, thus we need a 4-dimensional real space to depict the graph of a complex function  $w = g(z)$ .

One of the methods is to draw two copies of the complex plane  $\mathbb{C}$ . The plane  $z$  for the domain of the function  $f$  and the plane  $w$  for the codomain of the function  $f$ . Then in the plane  $w$  draw the images under  $f$  of various curves and regions in the  $z$  plane. The disadvantage of this method is, that it can be difficult to capture in a single image the behavior of the function  $f$ . For example see Fig. 3.1.

### 3.1 Domain coloring

This drawback can be at least partly overcome by a simple technique known as the *domain coloring*. This method was introduced by Frank A. Farris on his webpage [Far00]. Farris's method comprises of two main steps:

---

### 3. VISUALIZATION METHODS

---

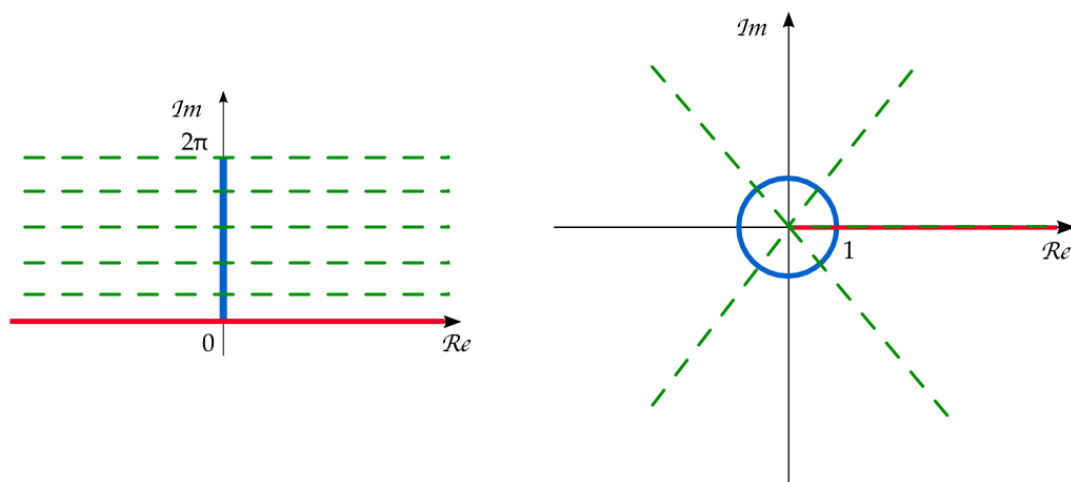


**Figure 3.1:** Visualization of the exponential function by drawing the domain (left) and the codomain (right) of the function.

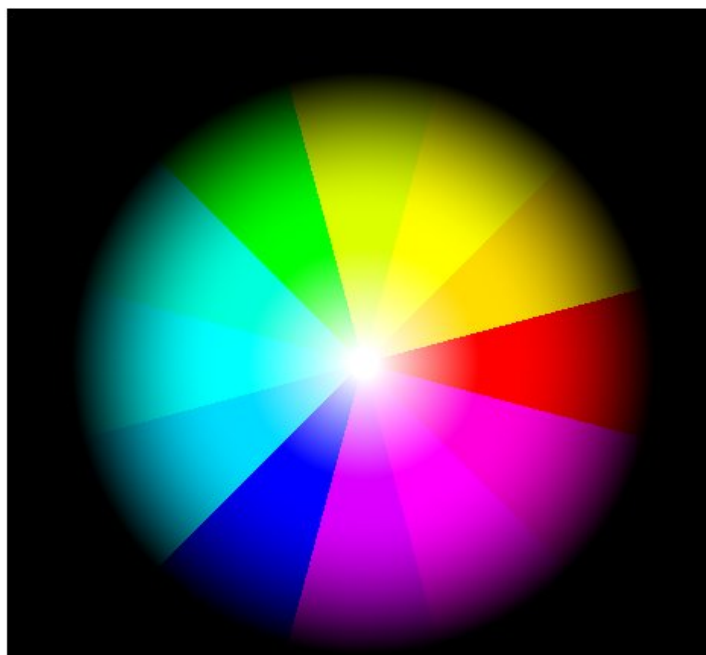


**Figure 3.2:** The figure displays color scheme used by Farris in the domain coloring method [Far00].

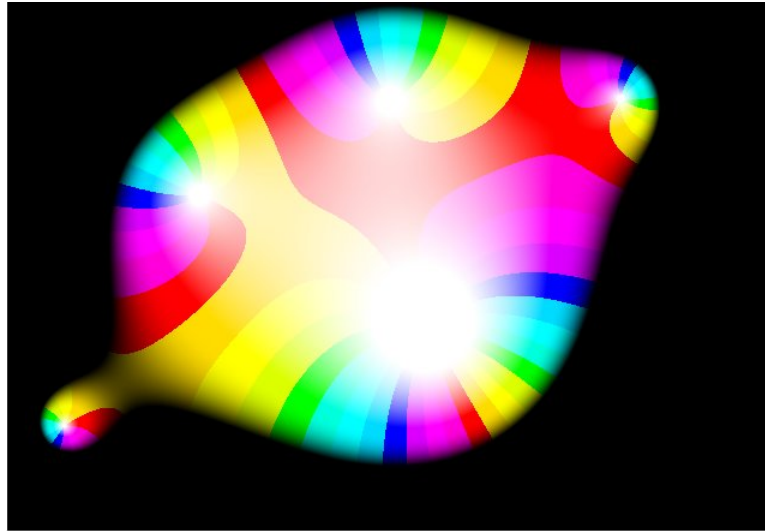


**Figure 3.3:** In the figure, we can see a visualization of a polynomial of degree six. The big white region marks double root of the polynomial function. The smaller white regions represents simple roots of the function [Far00].

1. Color the codomain  $w$ , this may also utilize a random image or a parametric texture.
2. Assign a corresponding color of  $f(z)$  to each point  $z$  of the domain.

Farris used color wheel around the beginning of the coordinate system containing of 12 distinct colors, see Fig. 3.2. The red color is situated around the positive real axis, green and blue are at the other two cube roots of the unity. Unlike the other methods, the visualization does not have continuous blending. Hues are interpolated, giving secondary and tertiary colors. The method uses blend toward the white at the center of the coordinate system and toward black with increasing valued of the modulus of the complex number. Thus, each complex number has a color associated to it.

The first example shows a polynomial function of degree six with four simple zeroes and one double zero. In the Fig. 3.3 you can see five white regions, which depicts zero points of the function. We can spot the double zero point out so, that making a sufficiently small circle around this point, the color scheme is repeating twice. This point can be seen in the middle of the figure.

### 3. VISUALIZATION METHODS

---

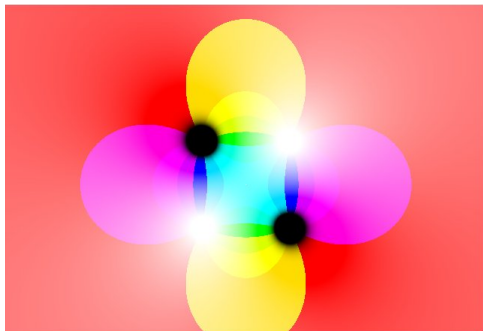


**Figure 3.4:** The figure depicts visualization of the function  $f(z) = (z^2 - i)/(2z^2 + 2i)$  [Far00].

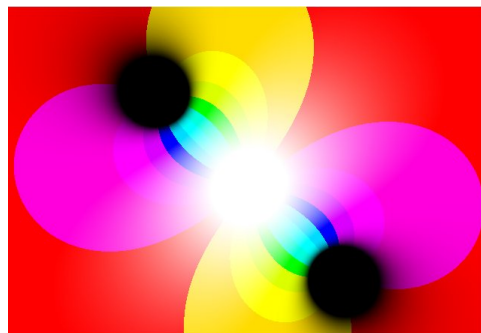


**Figure 3.5:** In the figure, one can see visualization of the function  $f(z) - f(0)$ , where  $f(z) = (z^2 - i)/(2z^2 + 2i)$  [Far00].

In the next visualization, let us observe the visualization of the function  $f(z) = (z^2 - i)/(2z^2 + 2i)$ , see Fig. 3.4. This rational function has two white spots, which depict two zeros and the two black spots depict the poles of the function. Each pole and zero is simple, because by circling each spot by sufficiently small circle, the scheme repeats once. It is interesting, that in the neighborhood of the beginning of the coordinate system only turquoise color appears. This leads to presumption, that the derivation of the function in the point 0 is zero. Our guess affirms the visualization of the function  $f(z) - f(0)$ , see Fig. 3.5. It is visible, that the beginning of the coordinate system has double zero point.

Plots using continuous color scheme created Da Silva [Sil10].

Another variation of domain coloring can be found in [Lun04]. The author picks a continuous radial color scheme with center at the origin of the coordinate system, see Fig. 3.6. This allows us to identify the argument by the color. A discontinues coloring makes it easy to find positive real axis, and in particular to find the point  $w = 0$ . A grayscale mask with the brightness equal to the fractional part of  $\log_2 |w|$  makes it possible to keep track of the absolute value  $|w|$ . With this mask it is easy to see the direction of growth of  $|f(z)|$ . From dark to bright within each ring, the absolute value doubles for each ring. However, the precise value of  $|f(z)|$  cannot be seen without some further reference point. The logarithmic scale counterbalances blow-up effect near multiple zeros. It also puts zeros and poles on an equal footing. Finally, blend the color scheme and

### 3. VISUALIZATION METHODS

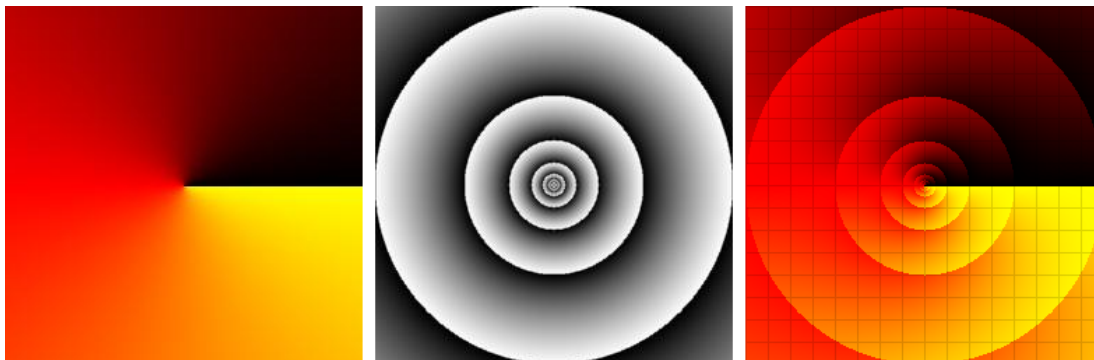


**Figure 3.6:** The figure displays color scheme used by Lundmark in his adaptation of the domain coloring method. The argument is identified with the color and the brightness equals to the fractional part of  $\log_2 |w|$  [Lun04].

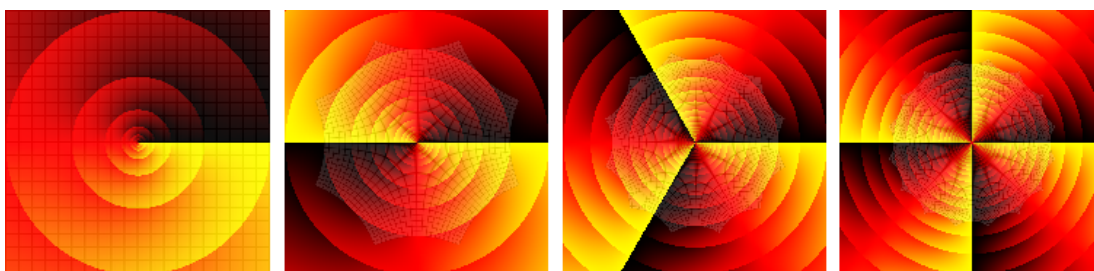


**Figure 3.7:** The visualization of the function  $f(z) = z^k$ , for  $k = 1, 2, 3, 4$ . The functions are restricted on region, where  $R = \{z \in \mathbb{C} : |\Re(z)| \leq 2 \wedge |\Im(z)| \leq 2\}$  [Lun04].

grayscale mask together to get the final coloring of the  $w$  plane, see Fig. 3.6. This method can be combined with orthogonal grid covering some part of the  $w$  plane.

Let us show visualization of a simple function  $f(z) = z^k$ ,  $k \in \mathbb{N}$ . Fig. 3.7 shows the first few  $f(z) = z^k$  for  $k = 1, 2, 3, 4$ . Notice, that the function projected the beginning of the coordinated system into itself. Recall that the complex powers are most easily understood in polar form. Is  $z = re^{i\phi}$ , then  $z^k = r^k e^{ik\phi}$ . This can be seen in the figures as the color scheme repeats  $k$ -times, when we encircle the beginning of the coordinate system by sufficiently small circle, i.e. for  $f(z) = z^2$  the color scheme repeats twice. This means, that for each point from the domain, excluding the point  $z = 0$ , there exist  $k$  points of the codomain, which have the same functional value. The point  $z = 0$  appears only once in the graph. From the



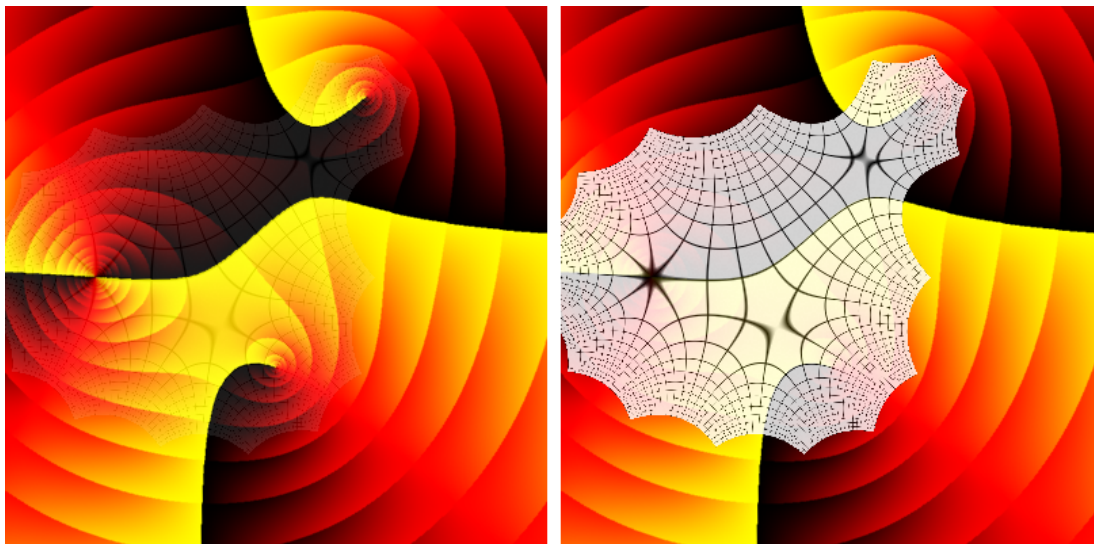


**Figure 3.8:** The visualization of the polynomial function  $f(z) = (z + 2)^2(z - 1 - 2i)(z + i)$ . The function is restricted on region  $R = \{z \in \mathbb{C}: |\Re(z)| \leq 3 \wedge |\Im(z)| \leq 3\}$ . In the left, there is the same visualization with highlighted orthogonal grid [Lun04].

deformation of the orthogonal grid we can assume, that the values of the modulus near the point  $z = 0$  are growing slower. On the other side, the radial circles on the outside of the unit circle are more closely together, therefore the relative growth of the function  $f(z)$  is faster on the outside of the unit circle, then on the inside of the unit circle.

Now, we can apply this method on a polynomial function. Fig. 3.8 left shows the fourth degree polynomial  $f(z) = (z + 2)^2(z - 1 - 2i)(z + i)$ . Its zeros are clearly visible as the endpoints of the yellow-black borders representing the positive real axis, and as the points around which the shaded rings of absolute value accumulate. In the left of the figure notice two yellow-black borders originating from the double zero at  $z = -2$ , i.e.  $f(z) = 0$  and also  $f'(z) = 0$ . The points at  $z = 1 + 2i$  and  $z = -i$  are the simple zeros, because there starts only one yellow-black border. The Fig. 3.8 right shows the same polynomial, but with the grid more clearly visible. This picture illustrates another important feature of analytic functions. They are conformal, which means that the angles are preserved. The conformality breaks down at three points, where the derivative  $f'(z) = 0$  (the  $f'(z)$  is a third degree polynomial).

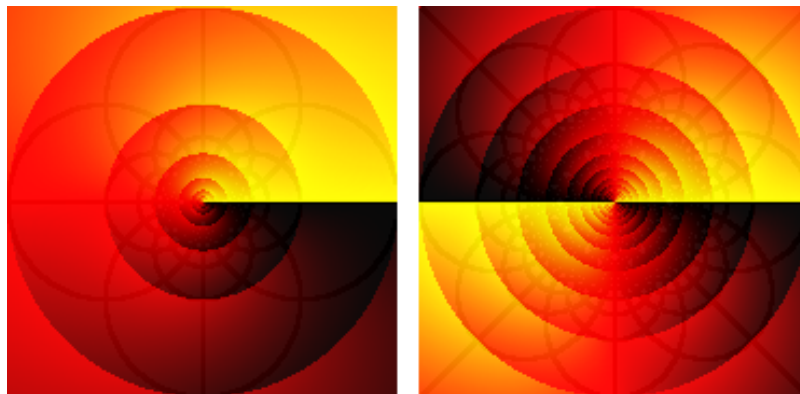


**Figure 3.9:** In the left, we can see the visualization of the function  $f(z) = 1/z$ , which has one simple pole in  $z = 0$ . In the right, the function  $f(z) = 1/z^2$ , which has one double pole in  $z = 0$  is depicted [Lun04].

The next example shows the visualization of rational functions. As well as zeros, there are now also poles. The disadvantage of this method is, that the poles look similar to the zeros. They can be diversified by the following two attributes.

1. The colors cycle in the opposite direction, i.e. we cross from black to yellow if we go counterclockwise.
2. The absolute value grows to infinity as we approach the pole, instead of vanishing, as it does for a zero, see Fig. 3.9.

In case of Möbius transformation the ability of recognition of the poles from the zeros (1.3) is very important. Fig. 3.10 shows the visualization of the Möbius transformation  $f(z) = \frac{z-1}{z+1}$ . From the formula, it is visible that the function has a simple zero at  $z = 1$  and a simple pole at  $z = -1$ . The real axis is mapped to the real axes, since all coefficients  $a, b, c, d$  are real. The imaginary axis is mapped to the unit circle with the center in the beginning of the coordinate system. By continuity of the function, the right half plane  $\Re(z) \geq 0$  is mapped to the interior of the unit circle. Circles containing the point  $z = -1$  are mapped to circles containing  $f(-1) = \infty$ , i.e. to straight lines, as the grid illustrates.

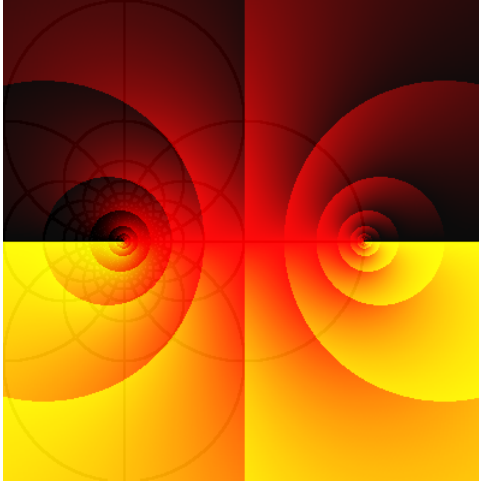


**Figure 3.10:** The visualization of the Möbius transformation  $f(z) = \frac{z-1}{z+1}$ . Notice the simple zero in the right part of the image and a simple pole in the left part of the image [Lun04].

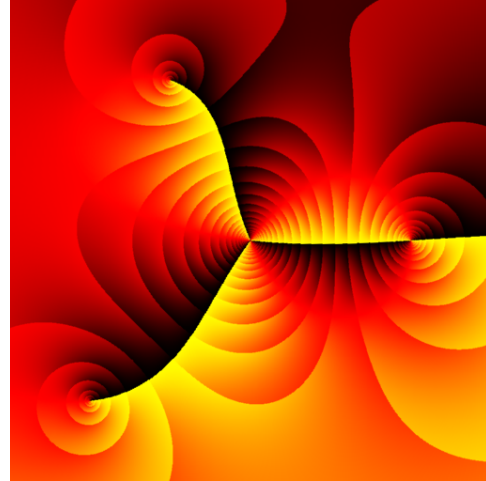


**Figure 3.11:** The figure depicts the visualization of  $f(z) = \frac{(z-2)^2(z+1-2i)(z+2-2i)}{z^3}$  [Lun04].

Fig. 3.11 shows a rational function given by the equation

$$f(z) = \frac{(z-2)^2(z+1-2i)(z+2-2i)}{z^3}. \quad (3.1)$$

with two simple zeros, one double zero and one triple pole.

Visualization of the function  $f(z) = e^z$  is depicted in Fig. 3.12. The period  $2\pi i$  is clearly visible, as well as the exponential growth of absolute value from left to right. Recall, that  $|f|$  doubles for each shades band, so that at the left edge it is very small ( $e^{-10}$ ) and at the right edge it is very large ( $e^{10}$ ).

Since the exponential function is periodic, it is many-to one. Consequently, it is not invertible, but its restriction to a chosen strip, for example  $-\pi < y \leq \pi$  is so. The inverse of that particular restriction is shown in Fig. 3.13. Note the discontinuity at the branch cut along the negative real axis. The singular point  $z = 0$  is the branch point of the logarithm.

The inability to visualize multi-valued functions is the disadvantage of the domain coloring method. The solution is in using Riemann surfaces, as it is shown in next examples and also in our research.

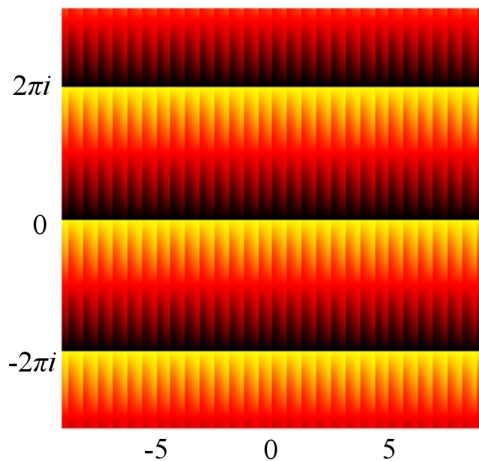


**Figure 3.12:** The visualization of the exponential function  $f(z) = e^z$  on region  $R = \{z \in \mathbb{C} : |\Re(z)| \leq 10 \wedge |\Im(z)| \leq 10\}$ . Notice that the function has imaginary period [Lun04].

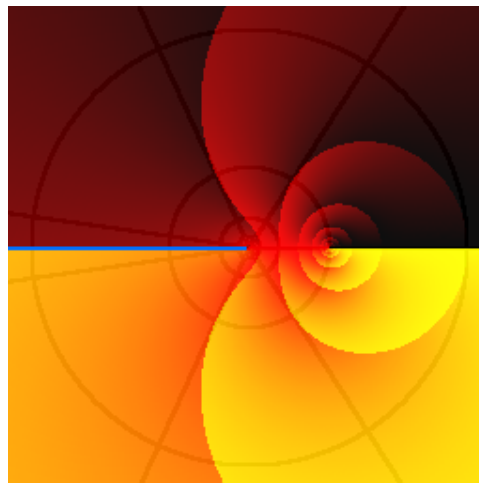


**Figure 3.13:** The visualization of the logarithmic function  $f(z) = \log z$  on region  $R = \{z \in \mathbb{C} : |\Re(z)| \leq 3 \wedge |\Im(z)| \leq 3\}$ . The blue line highlights the branch cut of the function [Lun04].

At the end, let us study Lundmark's visualization of complex sine function  $f(z) = \sin(z)$ . The trigonometric functions are defined for complex arguments through Euler's formulas. For sine function, the equation has form

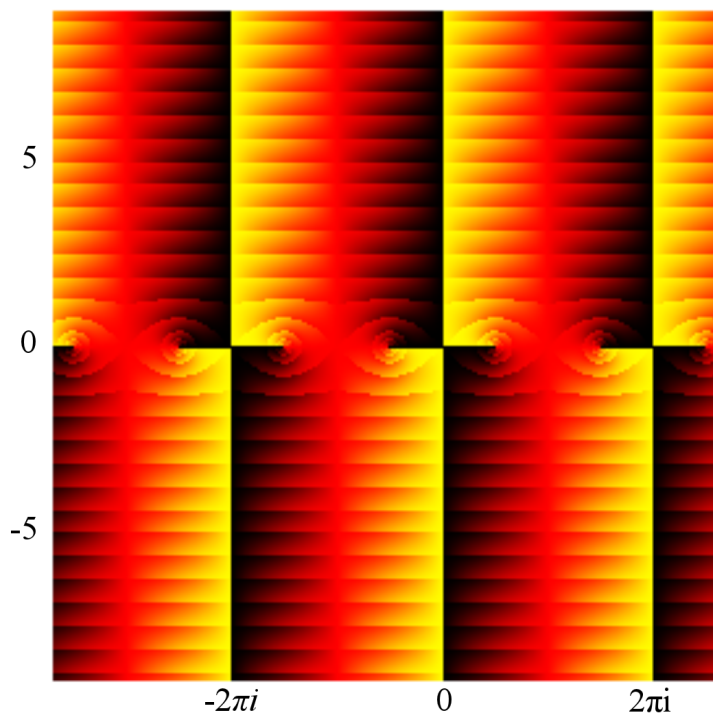
$$\sin(z) = \frac{e^{iz} - e^{-iz}}{2i}. \quad (3.2)$$

Fig. 3.14 shows the visualization of the complex sine function. Note, that the period is  $2\pi$ , the function has simple zeros at  $\pi n$  and the critical points are at  $\pi/2 + \pi n$ , where  $n \in \mathbb{Z}$ . Along the real axis the sine function oscillates between values  $-1$  and  $+1$ , and this agrees with the real number definition of sine function. For the complex values the sine function is no longer bounded within those limits. In fact, according to the formula

$$|\sin(z)|^2 = \sin^2(x) + \sinh^2(y) \quad (3.3)$$

it grows to the infinity exponentially in the vertical directions.

More complex function plots using similar scheme to Lundmark can be find in gallery created by Hlaváček [Hla07].



**Figure 3.14:** On the figure of the function  $f(z) = \sin z$  is visible the period  $2\pi$ , and also the zeros in  $\pi n$  [Lun04].

A comprehensive introduction to phase plots and colored analytic landscapes of single- and multi-valued functions is [Weg12], and publications [WS11], [Weg10]. Some examples of complex function visualizations and color analytic landscapes created in Mathematica software can be found in [Tha98].

One of the latest methods of visualizations of complex functions with domain coloring was published in [PP09] and it works as follows. We work on the unit sphere  $\mathbb{S}^2$  given by a parameterization  $\mathbb{S}^2 = \{(\cos \phi \cos \theta, \cos \phi \sin \theta, \sin \phi) \mid \phi \in [0, \pi], \theta \in [0, 2\pi]\}$ . To define the color scheme, we assign the HSB color scheme as follows: the color tone corresponds to the angle  $\theta$ , the tint to the radius  $r$  and the brightness defines the angle  $\phi$ . We compose the coloring function  $col$  into two functions  $col = c \circ p$ , where  $c: \mathbb{S}^2 \rightarrow HSB$ ,  $p: V \rightarrow \mathbb{S}^2$  and  $V$  being the codomain of the visualized function. The function  $c$  is defined in such a way that the south pole of the sphere  $\mathbb{S}^2$  is black, the equator has color with the maximum tint and brightness and the north pole is white. As the function  $p$  may be chosen e.g. the

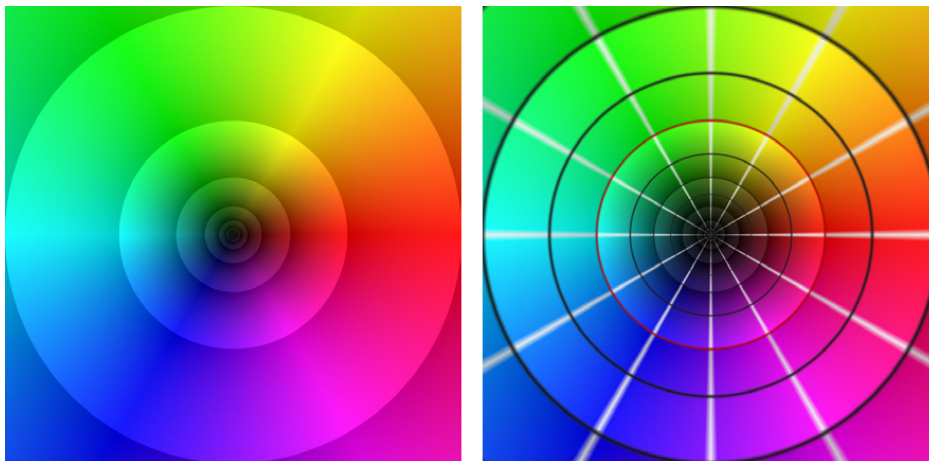


**Figure 3.15:** In the left, we can see the color scheme with the grayscale concentric circles, which denote the growth of the moduli of the function. In the right, the same color scheme overlaid by the radial grid is depicted. The grid highlights the unit circle with red color [PP09].

inverse of the stereographic projection, which in the black color is assigned to the point 0 and the white color to  $\infty$ . Also, we wish the scheme to be continuous and to engage the whole color spectrum, see Fig. 3.15. This work flow can be used to color Riemann surfaces or any other parameterized regular surface, see Fig. 3.16.

Via the coloring, we are able to detect visually zeros and poles of a given function. We can also see the deformation of the domain of the function. So far, we cannot determine the velocity of the value of the absolute value of the function  $f$ . We can only ascertain the direction of the growth from 0 to  $\infty$ . Therefore semitransparent layer with concentric circles and a repeating grayscale scheme is used in [Lun04]. To determine the radius of the circles, the logarithmic function was used. This gives an exponential growth of the radius. In the end,  $k$  half-lines are drawn, starting in 0 and intersecting the  $k$ -th unit roots in order to get a feeling of the distortion induced by the function  $f$ . By doing this, the domain is divided into  $k$  equally sized segments. Therefore, by comparison with the colored range of  $f$ , we get an impression which regions get compressed or stretched by  $f$  and which ones are reasonably maintained. After addition of the radial lines, it is time to add concentric circles. By this process, we get a polar grid blended over the reference coloring. When circling around such a contour line, the modulus is

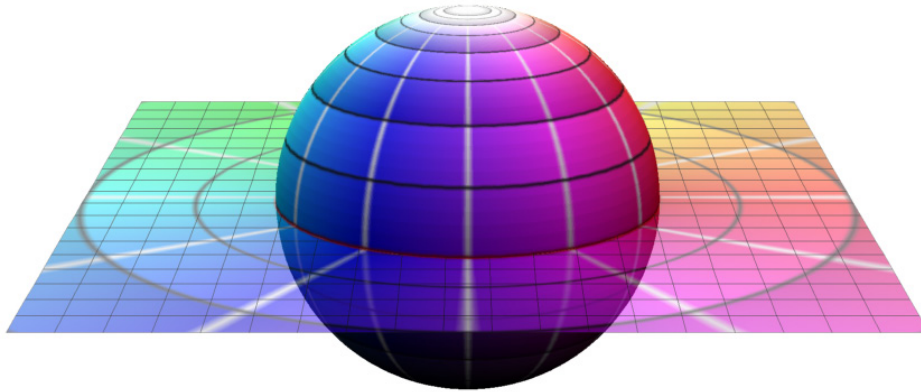


**Figure 3.16:** The figure displays the color scheme on the Riemann sphere used in [PP09]. Notice, that the north pole has white color and the equator has red color.

constant. The contour gives another hint on how to imagine a complex function. If  $f$  is meromorphic, every closed contour line contains at least one zero or pole in its interior. In particular, if many contour lines concentrate around a point  $z_0$ , then  $z_0$  is either a zero or a pole. For a better orientation, the unit circle is highlighted with the red color. Moreover, it is possible e.g. to find out whether the given function preserves angles or not via the obtained grid [PP09].

Let us study the introduced domain coloring on an example. Consider the meromorphic function  $f: R \rightarrow \Sigma$ , where  $R = \{z \in \mathbb{C} : |\Re(z)| \leq 3 \wedge |\Im(z)| \leq 3\}$  defined by

$$f(z) = \frac{(z-1)(z+1)^2}{(z+i)(z-i)^2}, \quad (3.4)$$

inducing the plot in Fig. 3.17. Take a closer look at the colors of the graph. Note that the center of the picture is colored in blue and magenta colors, thus by comparison to the original color map, this region gets mapped somewhere onto the lower left half plane. Now, consider the margin of the plot. Except the upper left corner, it is mostly colored in orange and ginger, so this region gets mapped onto the upper right plane with the real parts of the function values dominating the imaginary parts. This function has two zeros at  $\pm 1$ . Due to the choice of the coloring, zeros are colored as black spots, so they can be easily detected on the plot. Having a multiple zero  $z_0$  means that the scheme emphasizes the almost black regions and as a result, the dark neighborhood of  $z_0$  grows larger. Thus

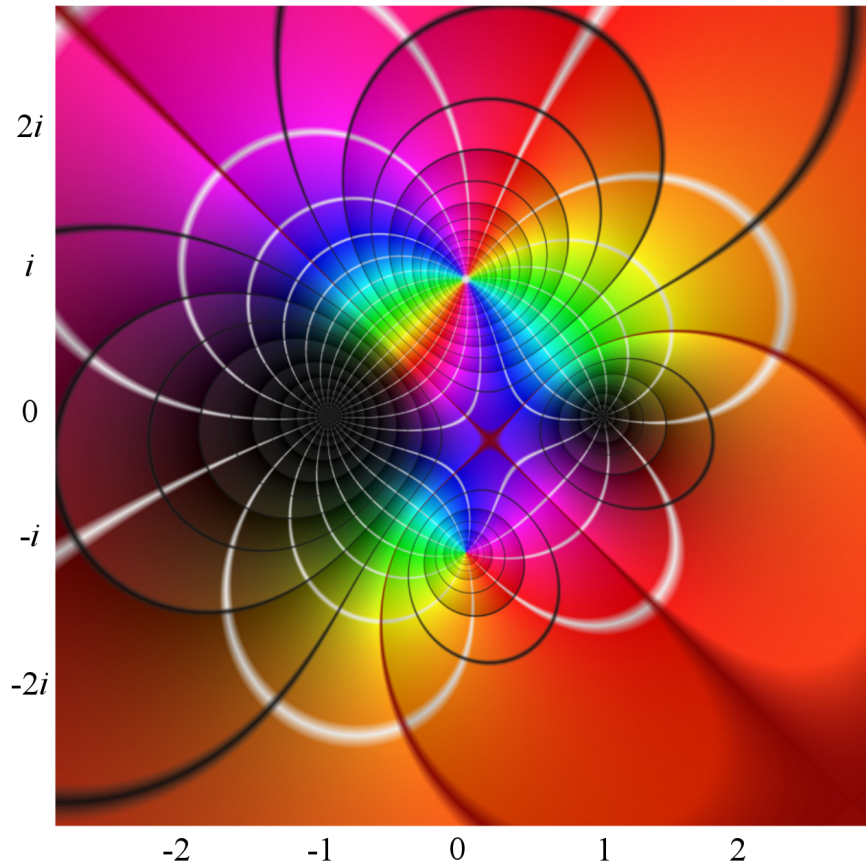


**Figure 3.17:** Visualization of the rational function given by (3.4). The function has a double zero in  $-1$  and a simple zero in  $1$ . There are also visible two poles, a double pole in  $i$  and a single pole in  $-i$  [PP09].

the higher multiplicity of a zero is, the larger is the extension of the black spot. The zero point at  $+1$  is a simple zero, because a sufficiently small circle around it maps to the whole spectrum exactly once. However, the zero point at  $-1$  is a double zero and a sufficiently small circle around  $-1$  maps to the color spectrum exactly twice.

The same observation hold true for poles. Unlike the zero points, poles have white color and the color scheme has different orientation. This means, that if we circle around the pole over a circle clockwise, we pass from the red color to the yellow color, not to the magenta. In the visualization of the function (3.4), a double pole at  $i$  and a single pole at  $-i$  are clearly visible.



### 3. VISUALIZATION METHODS

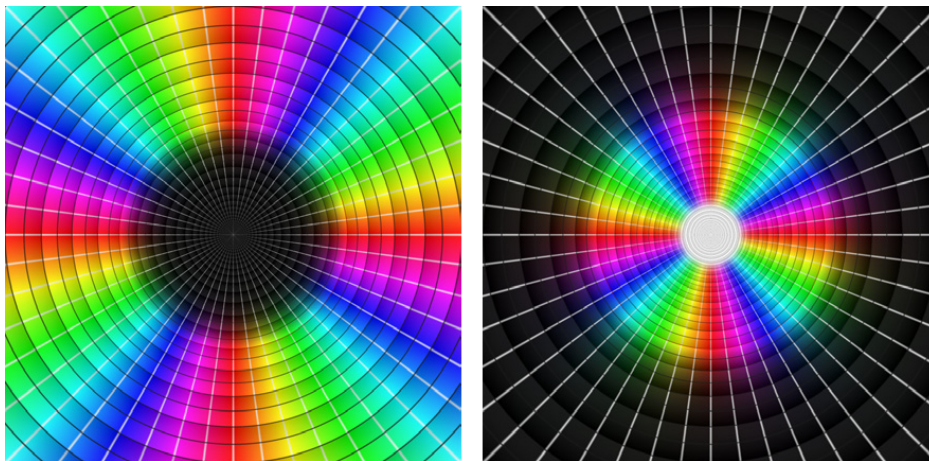


**Figure 3.18:** Left: the visualization of a quadruple zero is shown; right: we can see quadruple pole [PP09].

The points, in which the function (3.4) is conformal are points of the graph, in which the radial rays intersect the contour lines in a right angle both in the domain and in the codomain. For points in which the derivative vanishes, the radial rays and the contour lines do not intersect in a right angle. Non-conformal points can be found by the derivation

$$\frac{d}{dz}f(z) = \frac{(z+1)^2 + 2(z^2-1)}{(z-i)^2(z+i)} - \frac{2(z-1)(z+1)^2}{(z-i)^3(z+i)} - \frac{(z-1)(z+1)^2}{(z-i)^2(z+i)^2}, \quad (3.5)$$

and

$$\frac{d}{dz}f(z) = 0 \leftrightarrow z_{1,2,3} = -1, \frac{3-\sqrt{7}}{2} + \frac{\sqrt{7}-3}{2}i, \frac{3+\sqrt{7}}{2} + \frac{3+\sqrt{7}}{2}i. \quad (3.6)$$

These are the critical points and the function is not conformal there. We can see, that one point is the double zero, for one can easily see that the number of lines leaving the black spot has doubled. The second one is close to the origin and it can be detected in the figure as an intersection of two reddish curves, both of them denoting the unit circle. The same observation holds for the last non-conformal point in the lower left corner.

In the next example, let us consider polynomials of type  $f(z) = z^n - 1$  and  $g(z) = z^{-n} - 1$ , whose zeros are exactly the  $n$ -th unit roots  $e^{2\pi ik/n}$  for  $k = 0, 1, \dots, n-1$ . For  $z$  with  $|z|$  sufficiently large, we expect, that the function  $f$

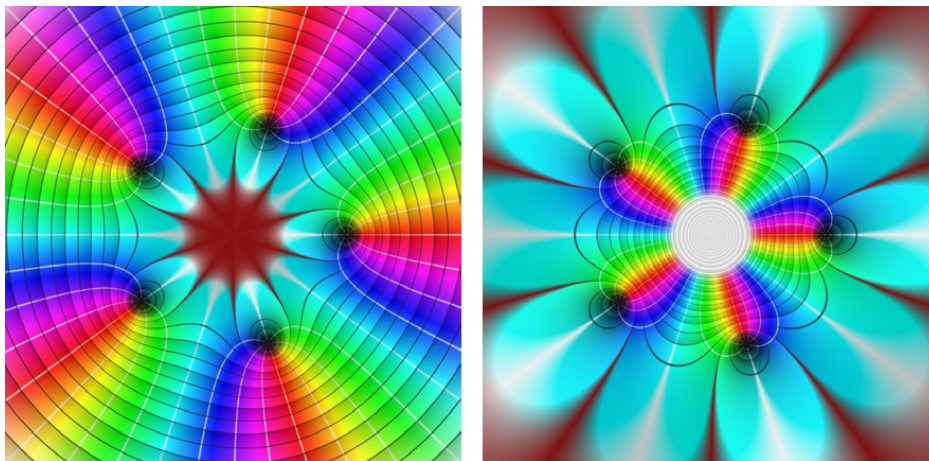


**Figure 3.19:** The left figure shows the visualization of the polynomial function  $f(z) = z^5 - 1$ . Notice, that the zeros are lying on the unit circle. In a bigger distance from the 0, the figure is similar to visualization of  $z \mapsto z^5$ . In the right, we can see the visualization of  $g(z) = z^{-n} - 1$ , which has also zeros on the unit circle [PP09].

behaves similarly to  $z \mapsto z^n$  and the function  $g$  behaves similarly to  $z \mapsto -1$ . This can be seen in Fig. 3.19, using  $n = 5$  on the region  $R = \{z \in \mathbb{C} : |\Re(z)| \leq 2 \wedge |\Im(z)| \leq 2\}$ .

The function  $f$  is colored cyan in the interior of the unit circle, which indicates complex numbers with negative real values and almost zero imaginary part. Furthermore, outside the unit circle, one finds a coloring which more and more resembles the coloring of  $z \mapsto z^5$ , the more you move away from the origin. The curves meeting in the origin all get mapped onto the unit level line with radius 1, indicating a breach of conformality. The white rays pointing outwards in the plot of the function  $g$  depict exactly the negative real axis and the complete region outside the unit circle is colored cyan.

### 3.2 Visualization of multi-valued functions

So far, coloring the domain in  $\mathbb{C}$  has worked properly. A problem arises, if the domain does not correspond with the topology of the complex plane. For instance, consider the function  $f(z) = \sqrt{z}$ ,  $g(z) = \log z$  (the principal branch) and

### 3. VISUALIZATION METHODS

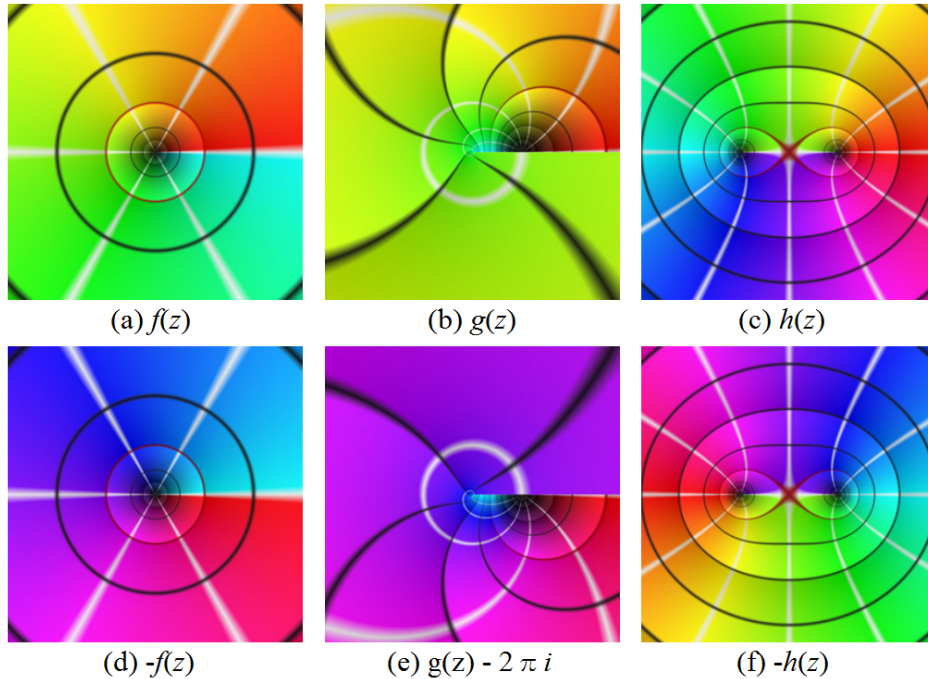


**Figure 3.20:** Figures picture the discontinuity of the domain coloring when used to visualize the roots  $f(z), h(z)$  and the logarithm  $g(z)$  [PP09].

$h(z) = \sqrt{z+1}\sqrt{z-1}$  defined on the region  $R = \{z \in \mathbb{C} : |\Re(z)| \leq 3 \wedge |\Im(z)| \leq 3\}$ . In the first two cases, the color scheme has a discontinuity at the positive real axis, in the third case, it has a discontinuity between points  $-1$  and  $+1$ , see Fig. 3.20. This problem occurs in general when the considered inverse function is of non-injective function. As a consequence, now there are several colors, according to the multiple values, getting assigned to a single point in the pre-image. Hence, the Fig. 3.21 left shows a model of the Riemann surface for the square root function  $f(z)$ . The advantage of having a second layer allows to resolve the discontinuity by switching to the other layer, when passing over the branch cut. The color plot of the function  $g(z) = \log(z)$  looks quite similar to the plot of the square root. But in this case, the discontinuity cannot be resolved by just introducing a second layer. The correct model is an infinite "spiral", see Fig. 3.21 right.

Figure 3.22 shows a more complicated example representing a Riemann surface for  $h(z) = \sqrt{z+1}\sqrt{z-1}$ . This time, the branch points are  $-1$  and  $1$ . By mapping of a sufficiently small circle around one of these points, one ends up on

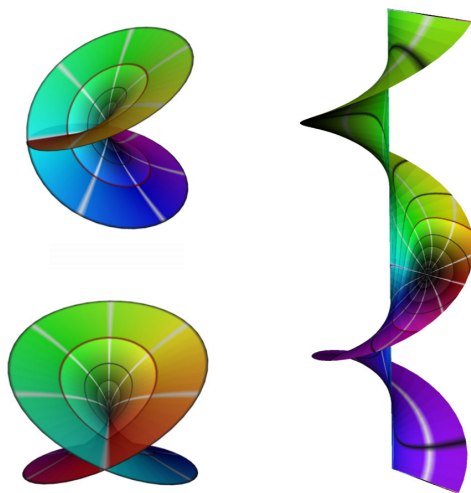


**Figure 3.21:** The left part of the figure depicts the Riemann surface of  $f(z) = \sqrt{z}$  from two different views. In the right the figure shows a part of the Riemann surface of  $g(z) = \log z$  [PP09].

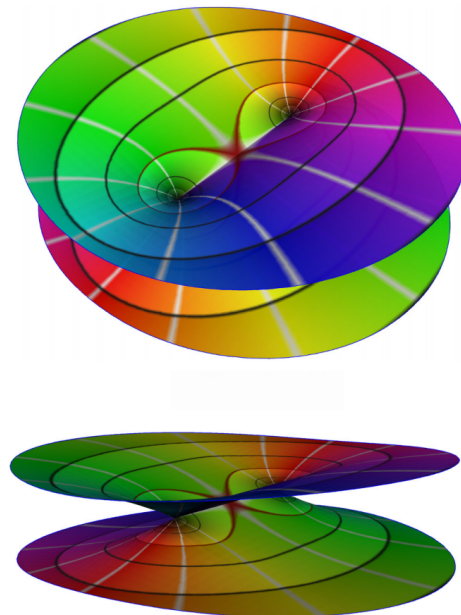


**Figure 3.22:** Riemann surface of  $h(z) = \sqrt{z+1}\sqrt{z-1}$  from two different angles [PP09].

the other layer in order to preserve continuity. The second map of a circle starts on the second layer and ends on the first layer.

The problem of automatic generation of the Riemann surfaces with manual addition of the branch points is discussed in the article [NPP10]. Resulting surfaces were published also in [PP09], more specifically in the figures 3.21 a 3.22.

Real time visualizations of geometric singularities were discussed [Kra12]. The author uses domain coloring to depict the change of the argument and creates the Riemann surface over part of the domain of the function.

An important contribution was made by M. Trott for the Wolfram research [Tro02]. He uses the symbolic derivation and nonlinear equation solver provided by Mathematica and compute 3D plots based on an explicit function definition. Trott also visualizes Riemann surfaces over Riemann sphere. He uses absolute value as a height function that leads to many intersections in the model of the Riemann surface. Also the visualizations do not have transparency, so one can not see all layers at once. An example of the visualization of some sheets of the function  $f(z) = \arcsin(z)$  is depicted in Fig. 3.23. To see the three branch points

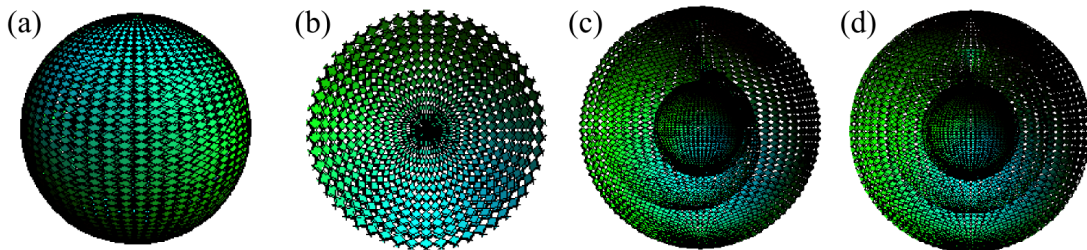


**Figure 3.23:** (a) Visualization of  $f(z) = \arcsin(z)$ , (b) cut along the  $xy$ -plane, (c) cut along the  $xz$ -plane, (d) cut along the  $yz$  plane [Tro02].

more clearly, one has to cut the sphere in half along the  $xy$ -plane, the  $xz$ -plane, and the  $yz$ -plane.

### 3.3 Technical background of CoFiViS

#### Blender

The visualizations were created by the open-source program Blender [Fou14a]. Blender is mostly used in 3D modeling, texturing, animating, rendering, physics simulations and much more. Standalone programs can be created by the built-in Blender Engine [Mul09]. Blender runs under several operating systems – MS Windows, Mac OS X and Linux and contains a scripting built-in tool for Python scripting [Fou14b]. This tool gives an access to most of the Blender functionality, such as mesh tools, materials, textures etc.

#### Representation and modeling of solids

The object representation with a triangular mesh is sort of standard. Unlike a general polygon, a non-degenerated triangle is always convex and its vertices lie on a plane. The popularity of the triangular representation caused that many graphics processing units have fast algorithms to depict triangles [SF04].

Let us take a look on the description of triangles, clusters of triangles and triangular meshes.

**Definition 3.1.** Polygonal mesh  $M$  is defined as a finite collection of vertices  $v$  (i.e. finite set of points), edges  $e$  (i.e. line segment which endpoints are from

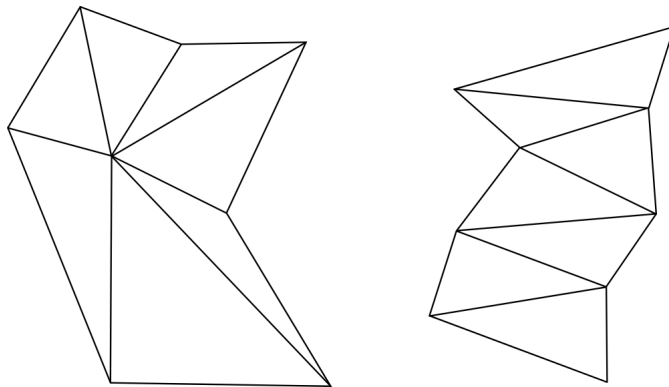


**Figure 3.24:** In the left, an example of a star is depicted. In the right, there is a figure of a chain of triangles.

the set of vertices) and faces  $f$  (i.e. convex planar polygons, which boundary is formed by edges) and the following holds:

1. every vertex is an end point of at least one edge,
2. every edge is a boundary of at least one face,
3. the intersection of two faces is either an empty set, a vertex of both faces or an edge of both faces.

In case all the faces are triangles, the mesh is called triangular mesh [Cha08].

**Definition 3.2.** A boundary  $\partial M$  of a mesh  $M$  is a union of edges of the mesh  $M$  such that every edge  $e \in \partial M$  belongs to a unique face  $f \in M$ . The polygonal mesh is called closed if the boundary  $\partial M$  is empty.

**Definition 3.3.** A polygonal mesh  $M$  is called a manifold, if every point from the interior of  $M$  has a neighborhood isomorphic with a neighborhood of a point in a plane. A point from boundary has a neighborhood isomorphic to an open half-disc.

**Definition 3.4.** The star of a vertex is the set of all triangles and edges from the triangular mesh containing the point.

An ordered list of triangles  $\Delta_1, \dots, \Delta_k$  is called a chain of triangles, if every adjacent triangles  $\Delta_i, \Delta_{i+1}$ ,  $i = 1, \dots, k - 1$  share a bounding edge. We say, that the chain connect the triangles  $\Delta_1, \Delta_k$ .



**Figure 3.25:** Figure depicts the planar and non-planar tetragon rendered by Blender engine. Notice, that the non-planar tetragon was automatically divided by Blender into two triangles.

The data structure, that describes the triangular mesh can be divided into two parts – geometric and topologic. The geometric part contains the coordinates of the vertices of the triangles and the topological part stores information about triplets of vertices of a triangle  $\Delta_i$ , or also the information about adjacent triangles of the triangle  $\Delta_i$ .

In some cases, we need to specify the triangle mesh only by one data structure. Then it is better to minimize the number of operations, which are executed with individual vertices of the mesh. The savings are made, if the triangles are aligned to a sequence that match to the chain of triangles, see Fig. 3.24 (right). This order provides, that every point in the chain is processed only once. In that case, the data structure is made of the sequence of coordinates of vertices, where every consecutive triple form a triangle. Likewise triangles can be aligned in a star, see Fig. 3.24 (left) [SF04]. An algorithm of compression can also be based on the Riemann surface structure [GWY04].

Blender works not only with triangle meshes, but also with polygonal meshes. The problem with planarity of polygons is solved by dividing each polygon into triangles and then the program renders the object. This can be seen on the shading of the rendered object, see Fig. 3.25.

A surface of revolution is frequently used in our visualizations. The surface of revolution is a surface in Euclidean space  $\mathbb{E}^3$  created by rotating a curve, called

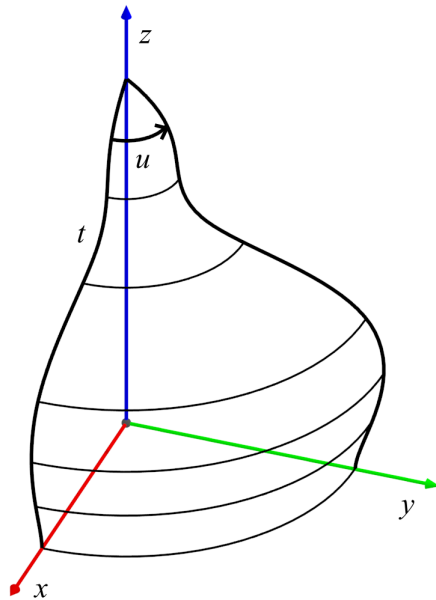


**Figure 3.26:** Example of the surface of revolution, where  $u \in [0, \pi/2]$ .

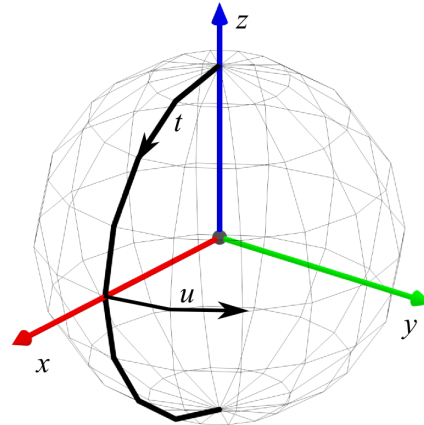


**Figure 3.27:** Interpolation of a unit sphere created by spherical coordinates with center in  $(0, 0, 0)$  with  $n = 9$  parallels (including poles) and  $m = 16$  meridians.

the generatrix around a line called the axis. For sake of simplicity, the axis is chosen to be identical to the  $z$  axis of the three dimensional Euclidean space  $\mathbb{E}^3$  and the generatrix lies in the  $xz$ -plane. Let  $x = f(t)$ ,  $z = g(t)$ , where  $t \in [a, b]$  is the parametrization of the generatrix. By the change of the parameter  $t$  and the parameter of rotation  $u$  one can obtain every point on the surface of revolution. The parametric equations of the surface are:

$$\begin{aligned} x &= f(t) \cos(u), \\ y &= f(t) \sin(u), \\ z &= g(t), \end{aligned} \tag{3.7}$$

where  $t \in [a, b]$  and  $u \in [0, 2\pi]$ , see Fig. 3.26. If the surface of revolution bounds a solid figure, we obtain a closed surface of revolution.



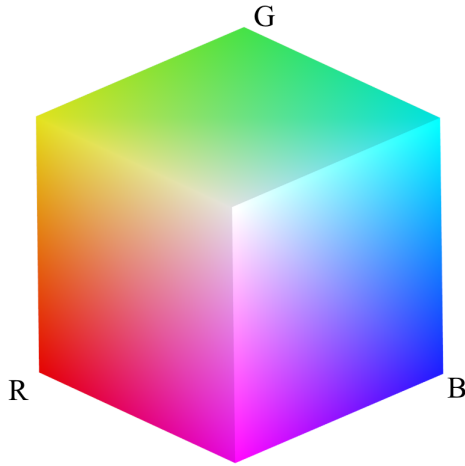


**Figure 3.28:** RGB color space visualized on a cube.

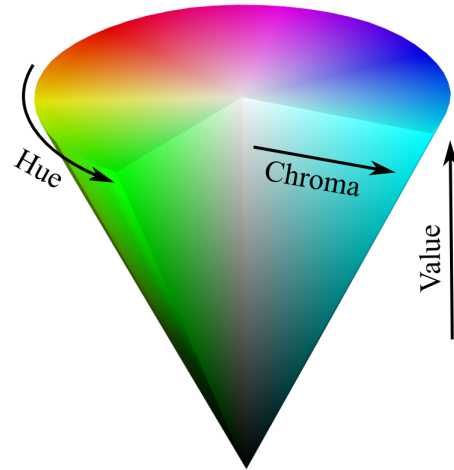


**Figure 3.29:** HSV color space visualized on a cone.

A common example of a closed surface of revolution is a sphere with center in  $(0, 0, 0)$  and radius  $r$  given by following equations:

$$\begin{aligned} x &= r \cos(t) \cos(u), \\ y &= r \cos(t) \sin(u), \\ z &= r \sin(t), \end{aligned} \tag{3.8}$$

where  $t \in [-\pi/2, \pi/2]$  and  $u \in [0, 2\pi]$ . To represent such a solid, one can use interpolation by a polygonal (triangle) mesh. To interpolate generatrix, let us use  $n$  points. For example, choose constant increment  $dt$  for the parameter  $t$ . Then, choose increment  $du$  of the parameter  $u$  for rotation so, that the rotation is approximated by  $m$  turnings from 0 to  $2\pi$ . This method gives us a grid consisting of  $u$  and  $t$  curves interpolating meridians and parallels, see Fig. 3.27.

Different way of creating a solid of a required form is by modifying of the position of the vertices of a basic solid. For example, one can move vertices of a polygonal grid in a chosen direction.

### Color spaces

By a combination of three basic colors from the color spectrum one gets a desired color. One of the most widely used color models is the RGB additive color model.

The colors are obtained by a combination of three colors – Red, Green and Blue (RGB). The colors are determined by a color vector, whose values are from the interval  $[0, 1]$ . In some cases, integers are used to define the color, where the components are integers from 0 to 255. In such case, the zero value means, that the color component is not represented in the final color. The maximal value 255 means, that the color component has maximal intensity. For example, if one chooses the maximal intensity to all three color components, the final color is white. The RGB color space can be visualized on a cube, see Fig. 3.28 [SF04].

Another frequently used color space is the HSV color model. The color is defined by hue, saturation and value of brightness. Hue defines the dominant color from the color spectrum, saturation defines the addition of other colors and value defines the intensity of the white light. The HSV color space is mostly visualized on a cone, see Fig. 3.29 or alternatively on a cylinder. The apex of the cone lies in the beginning of the coordinate system. The values of  $s$  – saturation and  $v$  – value are from the interval  $[0, 1]$ . The  $h$  hue is represented by an angle with values from the interval  $[0, 2\pi)$ . The apex presents the black color. The hue grows towards to the base of the cone and the white color is in the center of the base. The saturation corresponds to the distance from the axis of the cone.

## Coloring of 3D models in Blender

Blender offers multiple ways of coloring of the 3D model. The most common used method is by adding a material to the model. The material can affect not only color, but also the texture, transparency, reflectiveness, refraction etc.

A texture is a pattern, which helps with visual perception of the object. A texture can improve the quality of an object by a relatively low cost. A texture mapping consists of two steps. In the first step one defines the texture as an image. The image can be defined in different formats, e.g. JPEG, BMP, PNG, TGA, etc., or one can use procedural textures or video formats like mpeg, quicktime etc. The second step, when the texture is applied on an object is called texture mapping [SF04]. The texture mapping can be divided into three parts. First, the dimension and the format of the texture is defined. Then one defines the dimension of the texture regarding to the object. In the end, the method of texture mapping is

### 3. VISUALIZATION METHODS

---

determined, e.g. projection from cube or sphere, or UV texture mapping, where a user defines the position of every face in the texture.

# 4

## Results

### 4.1 CoFiViS

We have created CoFiViS, a tool for visualization single- and multi-valued functions. The algorithm can visualize polynomial function, fractional functions, e.g. Möbius function, trigonometric functions [VC10] and multi-valued functions like root functions  $f(z) = \sqrt[n]{z}$ , where  $n \in \mathbb{Z}^+$ , square root from polynomial [VC12], ADE singularities [BVC13] and the deformation between two functions by a sequence of images with use of a one parametric system [VC14].

Our algorithm uses two types of interpolation of a unit sphere, see Fig. 4.1:

1. The surface of revolution created by spherical coordinates with  $n$  meridians and  $m$  parallels. Such a model consists of triangles and quadrangles, therefore the algorithm uses built-in tool for triangularization of the mesh to get only triangles.
2. Interpolation by subdivisions of icosahedron.

The disadvantage of the first method lies in the uneven distribution of vertices, what results from the definition of such a surface. If the root lies outside the region with high number of vertices, the model has greater errors than the model constructed with the icosahedron. The model constructed by the second approach has uniform distribution of vertices and in general cases the final model has smaller errors, see Sec. 4.4.

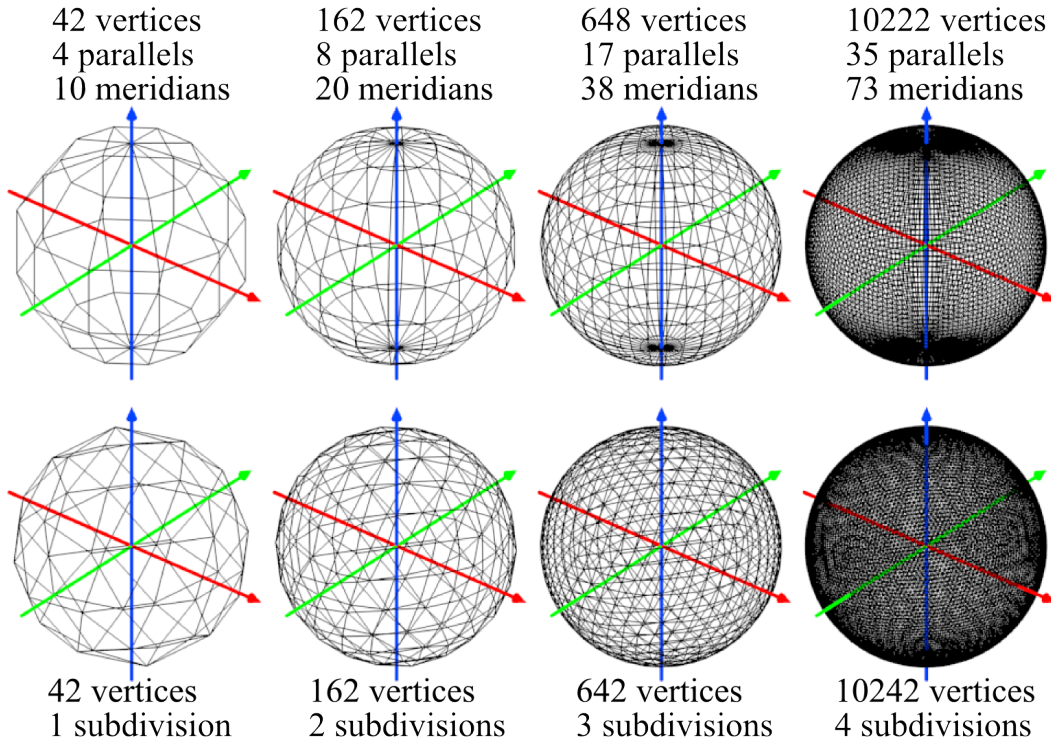


**Figure 4.1:** Polyhedrons constructed by the spherical coordinates with increasing number of meridians and parallels are depicted in the top row. In the bottom row, one can see increasing subdivisions of the icosahedron from left to right.

## Visualization of single-valued function

First, let us take a closer look on the visualization of a single-valued function. The steps are described closer in the following text.

### Algorithm – visualization of a single-valued function:

1. Choose the method of interpolation of the sphere  $\mathbb{S}^2$  with the number of meridians and parallels or the number of subdivisions and create the initial mesh.
2. For each vertex of the initial mesh compute its position in the complex plane  $\mathbb{C}$ .
3. Create the material and assign it to the model.
4. To each vertex of the mesh assign the corresponding color from the chosen color scheme.

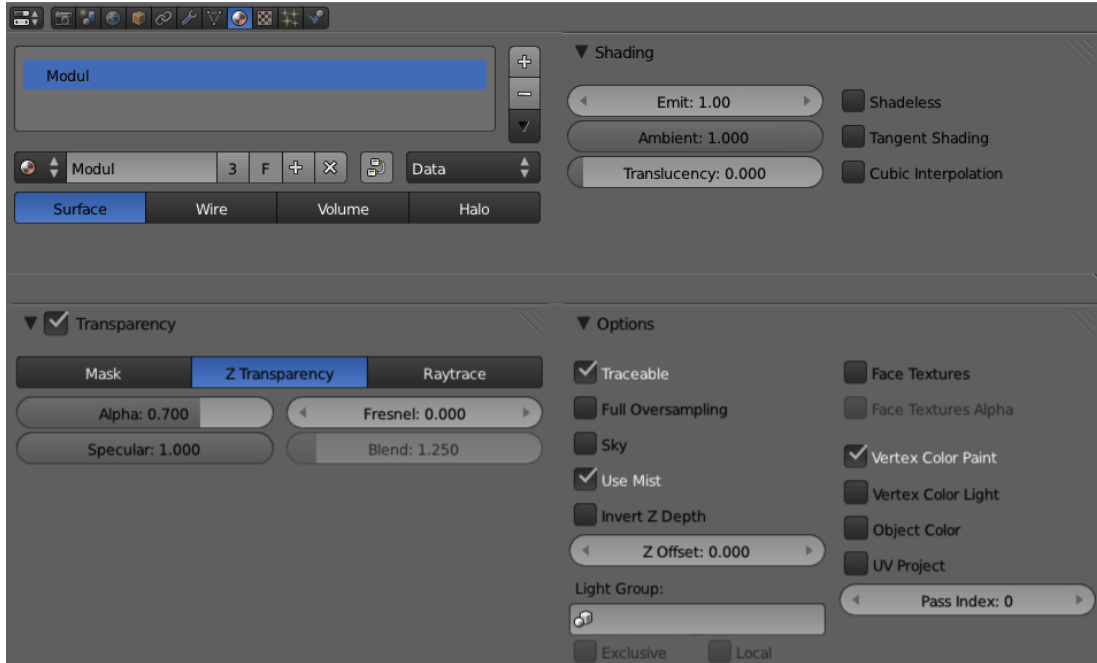


**Figure 4.2:** Notice the values of "Emit", "Alpha" and the "Vertex Color Paint" is checked.

5. For each vertex calculate the height function and translate each vertex by this value along the approximation of the normal in the corresponding vertex.

Our algorithm uses the stereographic projection (Def. 1.2), to compute the position of vertices in the complex plane  $\mathbb{C}$  except the vertex  $N$  with the  $z$ -coordinate equal to 1. This vertex corresponds to the point in infinity in the extended complex plane  $\Sigma$ , it always has red color and the height is equal to the limit  $h(\lim_{z \rightarrow \infty} f(z))$ , if it exists.

The visualizations use a semitransparent material, with value of transparency  $\alpha = 0.7$ . To eliminate the shadows on the model, the emit value is set to the value 1.0. This setting allows us to remove all lights from the scene. For the other options, like color of the material, amount of the reflectiveness etc. see Fig 4.2. The color layer overrides most of material setting and it affects the color

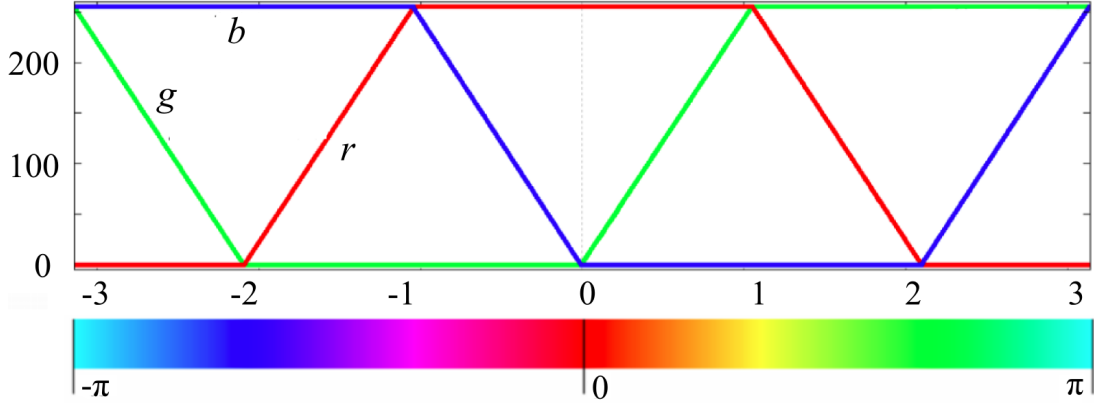


**Figure 4.3:** The color scheme used to visualize the argument of the complex number  $z$ . The components  $r$  (red),  $g$  (green),  $b$  (blue) are graphed. The functions are periodically extended over  $\mathbb{R}$ .

of each vertex. The color of each vertex presents the values of the argument of the function, computed by three color components  $r(\phi)$ ,  $g(\phi)$  and  $b(\phi)$

$$\begin{aligned} r(\phi) &= \min(\max(0, 255(\cos(\phi) + 0.5)), 255), \\ g(\phi) &= \min(\max(0, 255(\cos(\phi - 2\pi/3) + 0.5)), 255), \\ b(\phi) &= \min(\max(0, 255(\cos(\phi + 2\pi/3) + 0.5)), 255), \end{aligned}$$

where  $\phi = \arg(f(z))$  are the function values, see also Fig. 4.3. The color on edges and faces computes Blender by interpolating the color on corresponding vertices.

After our script assigns the material to the model it passes to the next step and it computes the distance of the vertices of the semitransparent layer from the unit sphere  $\mathbb{S}^2$ . The absolute value of the number  $z$  is used to compute its height function. Because the absolute value may have arbitrary large non-negative values including the infinity, a modifying function is used to transform these values into a prescribed compact interval. It is achieved by the real function

$$H(z) = \arctan(|z|), \quad (4.1)$$

which maps the absolute value from the interval  $[0, \infty]$  to the bounded interval  $[0, \frac{\pi}{2}]$ , see Fig. 4.4. In case of a single-valued function, the value  $f(z)$  is represented in this way. For a simple example, how the height function  $H(z)$  affects the modulus of the function  $f(z) = e^z$ , see Fig. 4.5.

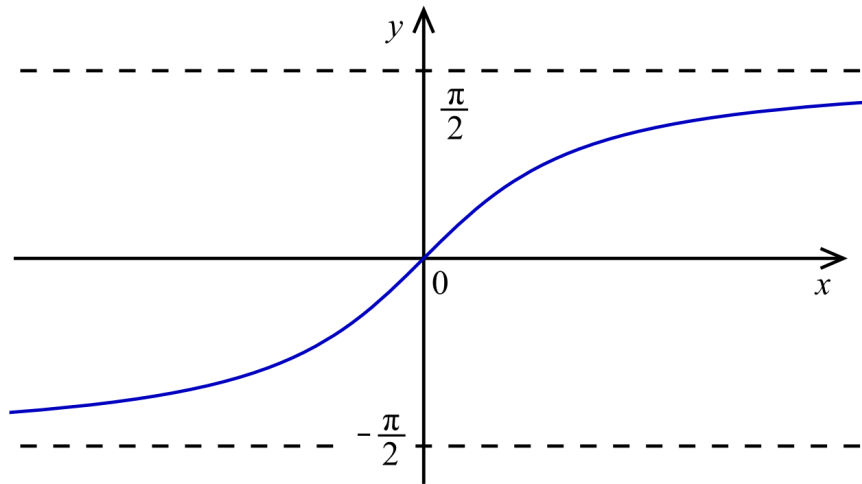


**Figure 4.4:** The graph of the function  $\arctan(z)$ , that was used to transform the values of the modulus of the complex number from the interval  $[0, \infty]$  to the interval  $[0, \pi/2]$ .

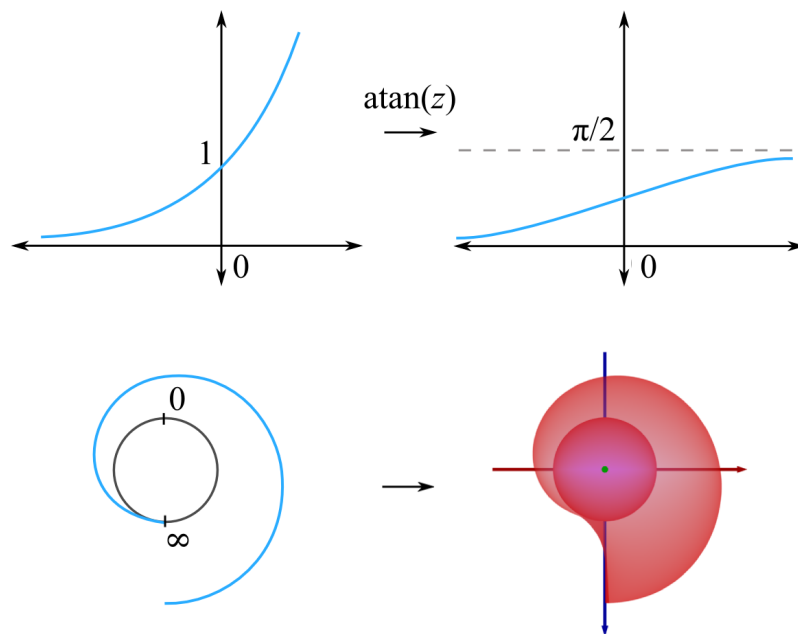


**Figure 4.5:** The figure presents how the height function  $H(z) = \arctan(|z|)$  transforms the absolute value of the single-valued function  $f(z) = e^z$  (top). Then these values are used to determine the normal height of the semitransparent layer (bottom).



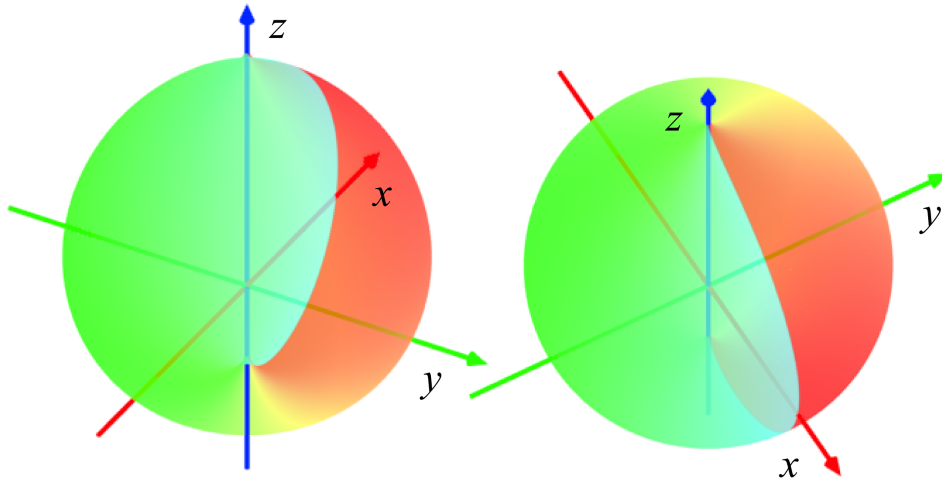


**Figure 4.6:** The graph of the function  $f(z) = \sqrt{z}$  without using its Riemann surface in two different views. There is a visible discontinuity in the color scheme and comparing to Fig. 4.3, there is only half of the color scheme in the graph. Such problems arise because the function  $f(z)$  is double-valued.

## Visualization of multi-valued function

A problem in the previous method arises when a graph of a multi-valued function is constructed. Multi-valued functions associate every input with at least one output. Typically, there are maps one to many. In such case, the domain coloring does not work directly, only a part of the values of the function is displayed as one can see on Fig. 4.6. Using Riemann surface, the domain of the multi-valued function is transformed so, that the function over it behaves as a single-valued function.

The following algorithm describes the visualization of a multi-valued function.

### Algorithm – visualization of a multi-valued function:

1. Choose method of interpolation of the sphere  $\mathbb{S}^2$  with the number of meridians and parallels or the number of subdivisions and create the initial mesh.
2. For each vertex compute its position in the complex plane  $\mathbb{C}$ .
3. Add vertices lying on the branch cut of the function, see Sec. 2.1.
4. Create the material and assign it to the model.
5. To each vertex of the mesh assign the corresponding color.

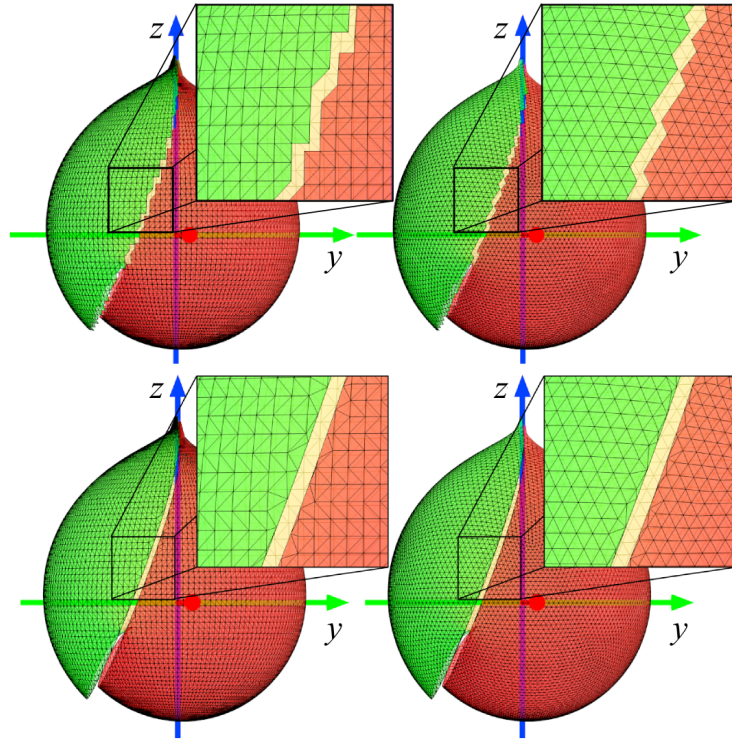


**Figure 4.7:** The top row shows the alias on the edge of the the model without adaptive subdivision of the function  $f(z) = \sqrt[3]{z + 0.6 + 0.4i}$ . In the left, the model is made by spherical coordinates and in the right, the model is made by subdivision of the icosahedron. The bottom row shows the model with implemented branch-cut. The alias is eliminated by adding vertices, which are lying on the branch-cut of the function.

6. For each vertex calculate the height function and translate each vertex by this value along the approximation of the normal in the corresponding vertex.
7. Repeat previous steps for each branch of the function.

The steps 1., 2. are identical to the steps 1., 2. in case of visualizing a single-valued function. In the third step, the vertices corresponding to the branch-points are added, see Fig. 4.7. Then, the script selects edges, which are intersecting the branch-cut of the function, subdivides them and changes the position of the new vertices, so they lie on the branch-cut.

The material used in visualization of multi-valued functions is similar to the one used in visualization of single-valued functions except the value of trans-

parency, where  $\alpha$  varies to the number of layers of the graph. In general, the value of transparency  $\alpha$  is lower when the number of layers is higher.

To visualize a multi-valued complex function, another height function has to be applied. Since the absolute value of the function is a non-injective map, the layers of Riemann surface could have the same height. Therefore, in case of multi-valued functions our algorithm uses the height function

$$H(z) = \arctan(|z|) \cdot \sqrt{1 - \cos(\arg(z)) \cdot e^{-\sqrt{|z|}}}. \quad (4.2)$$

The function  $H(z)$  is continuous at  $z = 0$  and  $z = \infty$  with values  $H(0) = 0$ ,  $H(\infty) = \pi/2$ . Using  $h(z) = H(f(z))$  for a prescribed function  $f(z)$ , its zeros and poles have similar properties. Such an approach separates layers except the points overlapping due to projection from  $\mathbb{E}^4 \rightarrow \mathbb{E}^3$  and the non-injectivity of the function  $\cos(\arg(z))$  on the interval  $[0, 2\pi)$ . The layers intersect, if for two complex numbers  $z_1 = z_2$ , the absolute value of the function is equal  $|f(z_1)| = |f(z_2)|$  and the argument of the complex function satisfies  $\arg(f(z_1)) = 2\pi - \arg(f(z_2))$ .

### Adaptive subdivision method

In our previous work, we used the interpolation of the sphere by creating a polyhedron constructed by an uniform sampling via spherical coordinates [VC10]. An uneven distribution of the vertices on  $\mathbb{S}^2$  is a disadvantage of this method. Therefore, we examined other method – sampling of the sphere using icosahedron and its subdivision. Using the latter approach, one obtains a smaller average error in comparison with a model having similar number of vertices created by the former approach.

Such a way of sampling can be enhanced with adaptive subdivision [HDZ05]. Higher density of sampling is advantage in areas, where the change of the absolute value of the function is high and lower density in places with small change of the absolute value of the function. For adaptive sampling, the CoFiViS uses an algorithm based on the angle between approximations of two normals in adjacent vertices.

**Algorithm – adaptive subdivision:**

1. Create a polygonal graph of the function with low number of vertices and faces.
2. For every edge of the model, compute the angle  $\theta$  of normals in its end vertices.
3. If the angle  $\theta$  is greater than  $\theta_T$ , add the edge to the list of selected edges.
4. Split each selected edge to two by a set of new mid edge vertices and compute the color and the height of the new vertices.
5. Repeat the steps 2. – 4. until the amount of selected edges is equal to zero or the number of iterations is equal to a user selected maximum.
6. Add vertices lying on the branch-cut of the function.

The value  $\theta_T$  is a user predefined threshold. In our algorithm, we have chosen the angle  $\theta_T = 11$  degrees after some experiments. Such a choice gave sufficiently smooth graphs in our examples, where the graphs angularity (angle between two adjacent faces) is not visible for a naked eye. A user may change the angle in case, one needs more or less detailed model. The following visualizations use as an initial polyhedron either the first subdivision of the icosahedron or a polyhedron created from spherical coordinates on a sphere with 4 parallels (plus 2 poles) and 10 meridians.

**Metrics used for comparison of graphs**

We use standard Euclidean metric to compute the distance between two points in  $\mathbb{R}^3$  given by

$$\|x - y\| = \sqrt{(x_1 - y_1)^2 + (x_2 - y_2)^2 + (x_3 - y_3)^2}, \quad (4.3)$$

where  $x, y \in \mathbb{R}^3$  and  $x = (x_1, x_2, x_3)$ ,  $y = (y_1, y_2, y_3)$ .

The mean error of the graph is computed by

$$\epsilon = \frac{1}{N} \sum_{n=1}^N \|m_n - p_n\|, \quad (4.4)$$

where  $N$  equals to the number of edges of the graph,  $m_n$  denotes the middle point of the edge  $e_n$ ,  $P(\frac{m_n}{|m_n|})$  is the corresponding point in the domain of the function  $f$

and  $p_n = h(f(P(\frac{m_n}{|m_n|})))$  is the point on the graph corresponding to its evaluation by  $f$ .

In comparison of graphs, a notion of maximal error

$$\epsilon_{\max} = \max_{n=1\dots N} \|m_n - p_n\| \tag{4.5}$$

is also used.

Hausdorff distance, also called Pompeiu-Hausdorff distance, is defined for two closed and non-empty sets  $X, Y \subset \mathbb{R}^3$  as

$$d_H(X, Y) := \sup_{x \in \mathbb{R}^3} |d_X(x) - d_Y(x)|, \tag{4.6}$$

where the supremum could equally be taken just over  $X \cup Y$ , yielding an alternative formula

$$d_H(X, Y) = \inf\{\epsilon \geq 0 \mid X \subset U_\epsilon(Y), Y \subset U_\epsilon(X)\}, \tag{4.7}$$

where  $U_\epsilon(M) = \{x \in \mathbb{R}^3 \mid \exists y \in M : d(x, y) < \epsilon\}$ .

## 4.2 Visualization of basic functions

### The identity function

First, let us describe the identity function  $f(z) = z$ , to see, how to read the graph of the function. In the visualizations, we use red color to highlight the  $x$  axis, green color to highlight the  $y$  axis and blue color to highlight the  $z$  axis, see Fig 4.8. This is commonly used notion in the 3D modeling community. The visualization uses six subdivision of the icosahedron with 10242 vertices. The resulting polyhedron  $M$  gives us sufficiently smooth result. Higher subdivisions of icosahedron give also smooth results, but the high number of vertices has quite noticeable performance impact. The zero point can be identified as the point with the smallest height. In the case of the identity function, this point has coordinates  $z_0 = (0, 0, -1) = S$  in the  $\mathbb{E}^3$ . This point is a simple zero, because when one goes along a sufficiently small circle around the point  $z_0$  the color scheme repeats once. The point with the biggest distance from the unit sphere corresponds to the pole of the function  $f(z)$ . This is a single pole of the function because the color scheme repeats once.

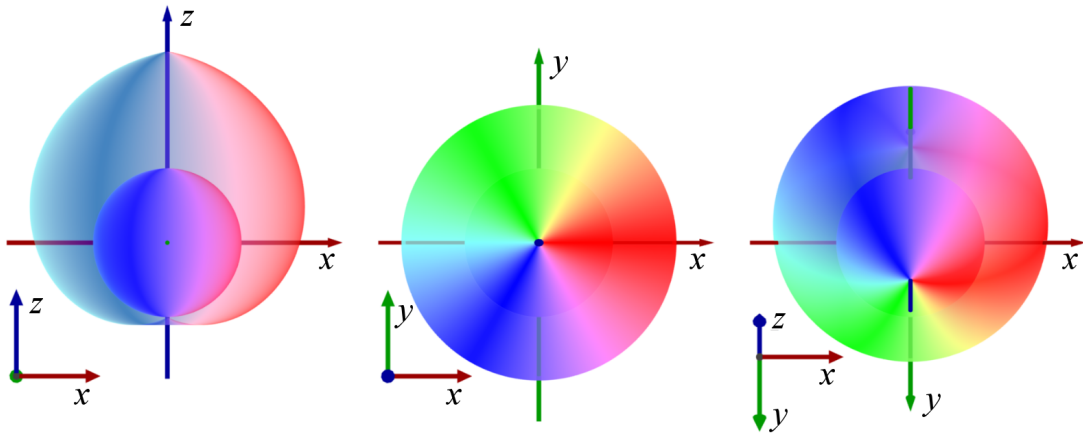


**Figure 4.8:** The figure depicts visualization of identity function  $f(z) = z$  from different viewports. The red axis corresponds to the  $x$ -axis, the green to the  $y$  axis and the blue to the  $z$  axis. The sphere inside the visualization represents the unit sphere  $\mathbb{S}^2$ .

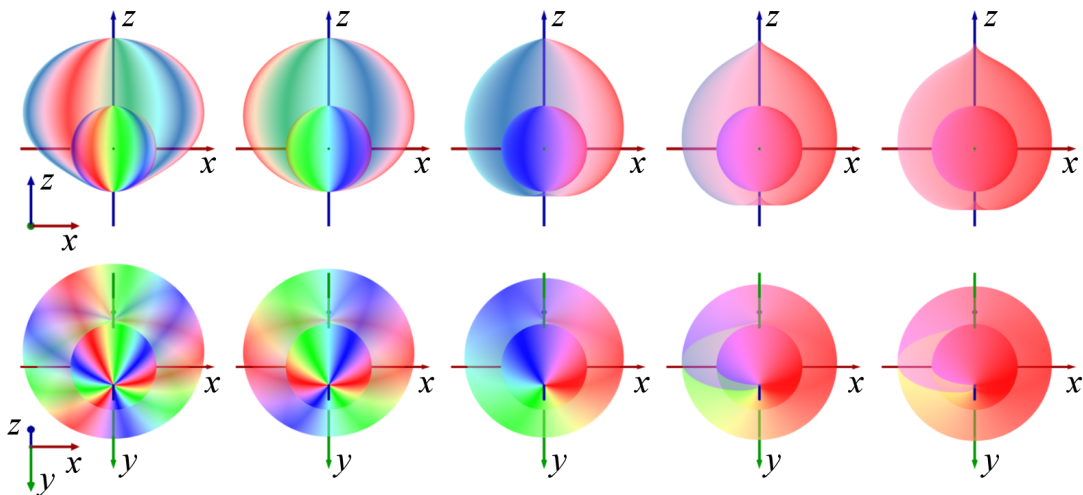


**Figure 4.9:** In the figure, we can see the visualization of a function  $z \mapsto z^n$  for  $n = 3, 2, 1, 1/2, 1/3$ . Notice, that the graph of  $z^{1/2}$  and  $z^{1/3}$  contains only part of the color scheme.

## Monomial function

Let us describe the visualizations of a function  $f(z) = z^k$ , where  $k \in \mathbb{Q}^+$ . In Fig. 4.9 we can see, that the point corresponding to 0 stayed at the same position as in the case of the identity function. Notice, that the color scheme around this point repeats exactly  $k$ -times for  $k \in \mathbb{Z}^+$ . This indicates, that for  $k = 2$ , the function has double zero at point  $z = 0$ , i.e. for every point  $z$  we have  $k$  points, that have the same value  $f(z)$ . The point 0 can be found in the graph only once. From the distance of the semi-transparent layer from the unit sphere, one can see, that the values of the modulus in the neighborhood grow faster for  $k > 1$  and for  $k < 1$  the values grow slower. The highest distance of the semi-transparent layer from the unit sphere is in point, that corresponds to the point in the infinity, so one can assume, that the function has a pole at the infinity. The function has in this point pole of order  $k$ .

For  $k \in \mathbb{Q}^+$  and  $k \notin \mathbb{Z}^+$ , the graph contains a part of the color scheme. This is because such a function is multi-valued. For the visualization of the whole domain of the function, our algorithm uses Riemann surface, see Sec. 4.2.

## Function $f(z) = (z - a)(z - b)$

Let us study function of type  $f(z) = (z - a)(z - b)$ , where  $a, b \in \mathbb{C}$ . The Fig. 4.10 depicts some examples of this function for different constants  $a, b$ . It is obvious, that for  $a = 0, b = 0$ , the visualization is identical to the one of  $z^2$ , see Fig. 4.10. For constants  $a \neq b$  two cone shaped surfaces are visible in the semi-transparent layer, which are situated around points corresponding to the zeros of the function. The color scheme around such a point repeats once, so all zero points are simple zero points of the function. The biggest distance of the semitransparent layer from the unit sphere  $\mathbb{S}^2$  is at point corresponding to infinity. The color scheme around this point repeats twice, so the function has double pole at infinity.

## Polynomial function

The graph of the function  $f(z) = (z - 0.5 + i)^2((0.5 - i)z - 1)$  is shown from several viewpoints, see Fig. 4.11. The function has two roots in points  $z_1 = 0.5 - i$  and  $z_2 = \frac{1}{0.5 - i}$ . These points can be identified by the cone shaped surface around

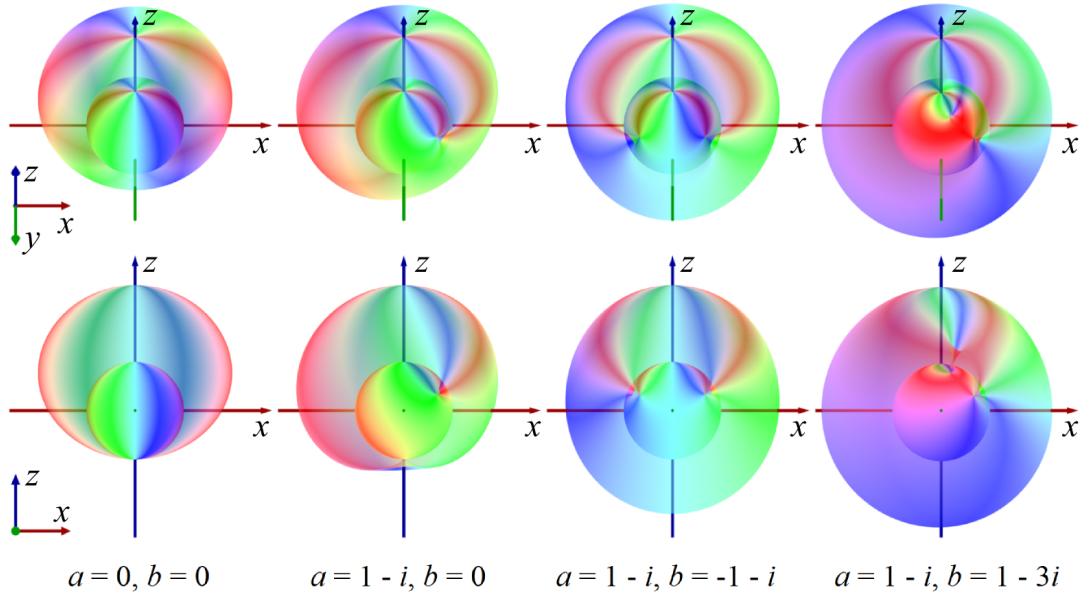


**Figure 4.10:** The figure shows visualization of the function  $f(z) = (z - a)(z - b)$  from two different viewpoints for different constants  $a, b$ .

such point. The root itself is mapped on  $\mathbb{S}^2$ . Clearly, the root  $z_1$  is a double zero point, hence the multiplicity of the color scheme is 2. The second root is a simple zero point. Around the infinity point with coordinates  $(0, 0, H(f(\infty)))$ , the color scheme repeats three times, so the infinity is a triple pole of the function  $f(z)$ .

### Möbius transformation

The ability to find position of the poles is essential in case of visualizing of a Möbius transformation. The Fig. 4.12 shows some examples of this transformation for different constants. It is visible, that the graph has one simple zero and one simple pole situated depending on the chosen constants. The semi-transparent layers form a cone shaped surface around each zero point. The poles can be identified as the points with the highest distance from the unit sphere  $\mathbb{S}^2$ . Unlike previous visualizations, the Möbius function do not always have pole at infinity, see second, fourth and fifth visualization from the left.



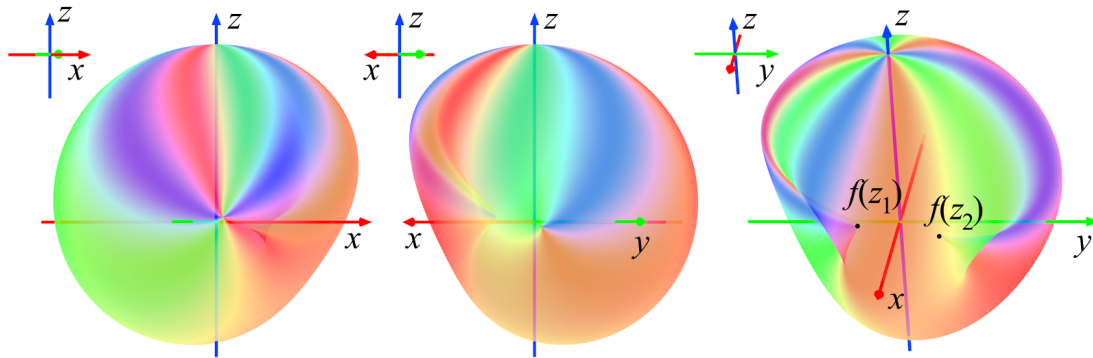


**Figure 4.11:** The graph of the function  $f(z) = (z - 0.5 + i)^2((0.5 - i)z - 1)$  is shown from several views. Images of the double zero point  $z_1 = 0.5 - i$  and single zero point  $z_2 = \frac{1}{0.5 - i}$  are highlighted in the figure (right).

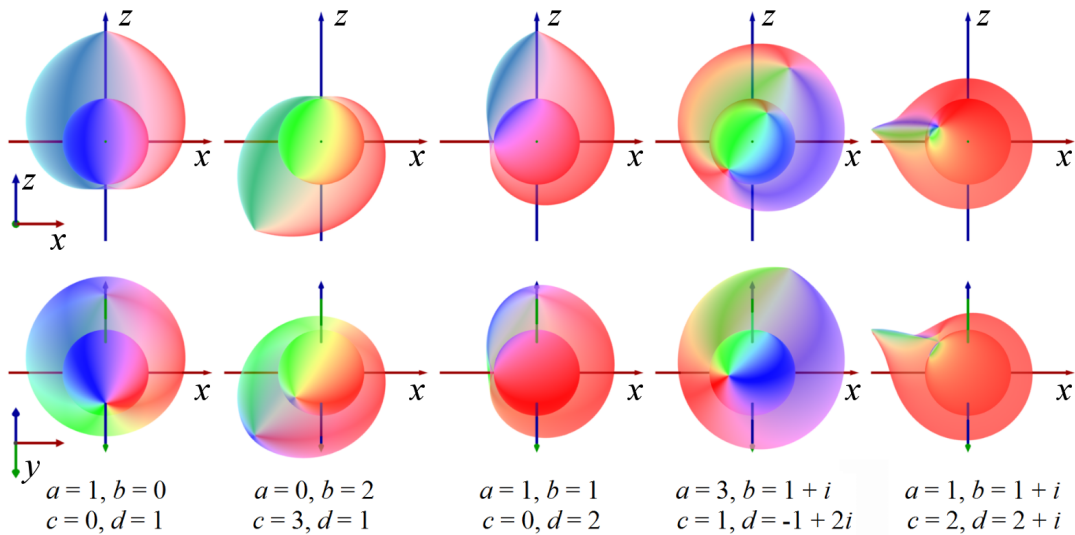


**Figure 4.12:** In the figure, we can see the visualization of Möbius transformation for different constants.

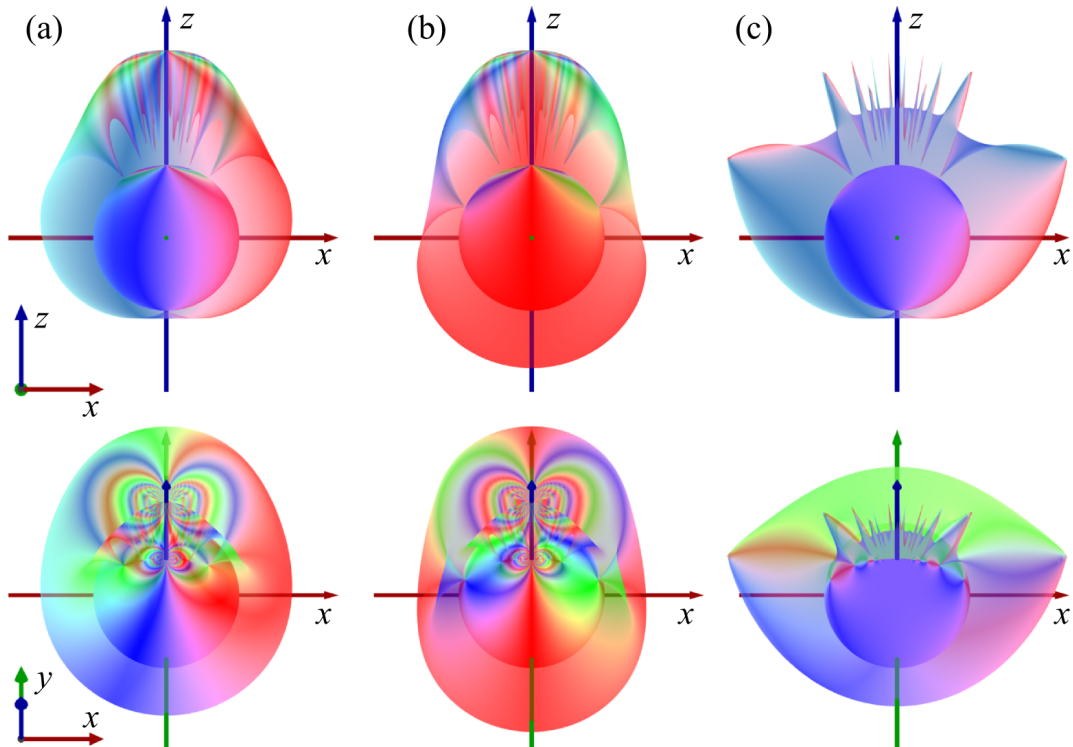


**Figure 4.13:** Visualization of trigonometric functions from two viewpoints (a) sines, (b) cosines, (c) tangent. Notice, that the infinity is an essential singular point.

## Trigonometric functions

Let us take a closer look at the visualization of sine, cosine and tangent function. From the visualization of sine it is visible, that the sine function has a zero point at 0. Other zero points lie on the plane  $xz$ , corresponding to the real axis. In the neighborhood of the infinity, the density of zero points is higher than the density of the mesh sampling. That causes inaccuracy in the visualization. Also the value of the function in the point infinity cannot be computed, because the sine function has an essential singular point at infinity.

The visualization of the cosine function is similar to the one of the sine function. One can see, that the zero points are also lying on the plane  $xz$  and there is no zero point within the unit circle. The cosine also has an essential singular point at infinity.

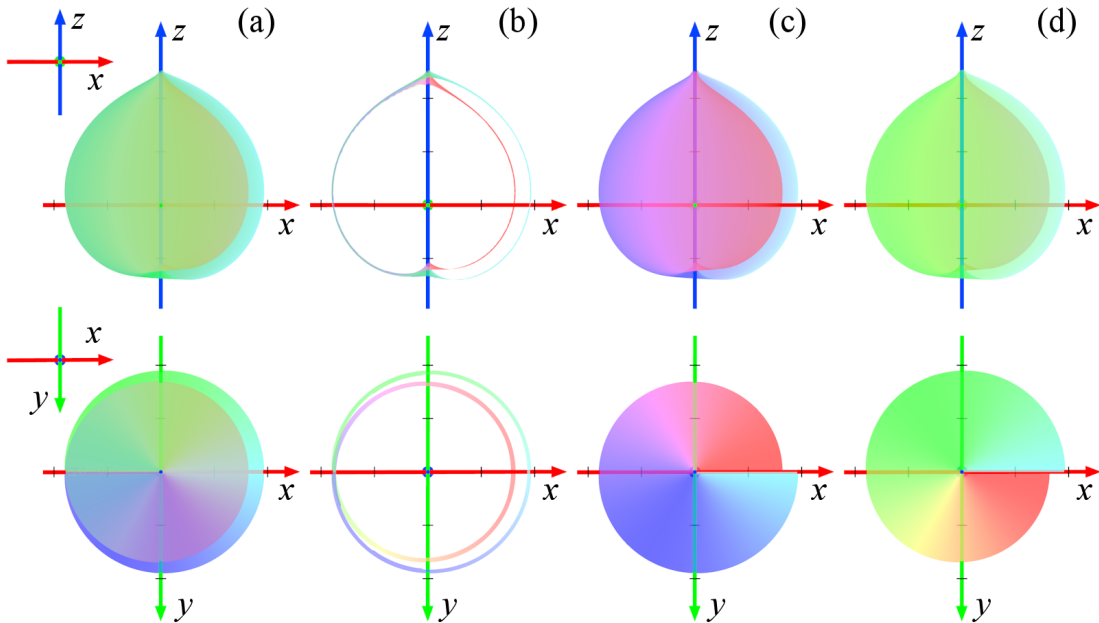


**Figure 4.14:** The figures display the Riemann surface of the square root from the front view (top row) and the top view (bottom row). (a) The whole visualization of the square root, (b) the cutouts of the graph, (c) the first layer and (d) the second layer.

The visualization of the tangent function has zeros and poles at the intersection with plane  $xz$ . One can see, that the zeros and poles form an alternating sequence. There are inaccuracies around the infinity from the same reason as in the previous two visualizations. The infinity is also essentially singular point.

## Root function

As we mentioned earlier in Sec. 4.2, the root function  $f(z) = \sqrt[n]{z}$ ,  $n \in \mathbb{Z}^+$  is a multi-valued function, specifically, it has  $n$  branches. To visualize the graph of such a function, our algorithm uses different height function  $H(z)$  as in case of single-valued function, see (4.2).

Let us describe the square root function  $f(z) = \sqrt{z}$  in detail. The graph of this function has two layers. The data for the vertices of the first layer can be computed from the equation  $f(z) = \sqrt{z}$ , where  $\sqrt{z}$  is the positive branch of the square root function. This gives us layer with the colors of the vertices from the

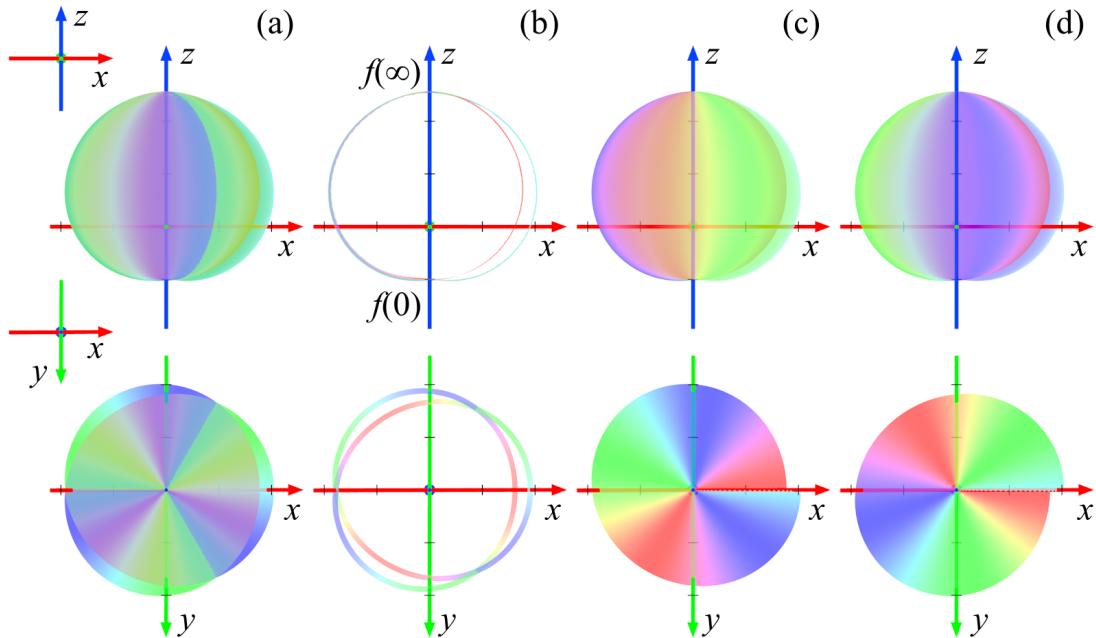


**Figure 4.15:** The graph of the function  $f(z) = \sqrt{z^3}$  from two different points of view: top the front view (the direction of view is the  $y$ -axis), bottom the top view (negative  $z$ -axis direction). The graph has two layers corresponding to the two branches of the square root function, and the color scheme repeats three times due to the 3rd power of  $z$ . (a) composition of all two layers of the graph, (b) cutouts of the graph, (c) first layer, (d) second layer.

first half of the color scheme where  $\phi \in [0, \pi]$ , see Fig. 4.14 (c). The colors and height of the vertices from the second layer are given by the formula  $-f(z)$ , see Fig. 4.14 (d). These two layers intersect in points that correspond to the negative real axis, see Fig. 4.14 (a), (b). The singular points (the root of the polynomial) lie on the domain sphere  $\mathbb{S}^2$ . In this case, it is the point  $z = 0$ . The surface has the form of a helix around points corresponding to 0 and  $\infty$ , what indicates, that these two points are branch points of the function  $f(z)$ . The maximal height at the point  $z = \infty$  indicates that this point is also a pole of the function. The color scheme is continuous over the whole graph, so one can assume, that the argument is continuous over the whole domain of the function. The cutouts are obtained by intersection of the graph with a cuboid.

The following example illustrates a more complicated visualization of the the function  $f(z) = \sqrt{z^3}$ , see Fig. 4.15. The figure shows the graph of the function  $f(z)$  from two different points of view. In the left figure, the direction of the camera corresponds to the  $y$ -axis (front view). In the right one, the direction corresponds to the negative  $z$ -axis (top view). The right figure shows that the resulting function has two layers, each corresponding to one of the two branches  $\sqrt{z}$  and  $-\sqrt{z}$  of the square root function. In a neighborhood of 0, one can see three copies of the color scheme corresponding to  $z^3$  in  $f(z)$ . One can also observe that the graph has minimal height at the point that corresponds to  $f(0)$  and the two layers meet at this point. This is due to the fact that 0 is a branch point of the square root function.

The color scheme is continuous in the entire visualization, indicating that the value of the argument of the function is also continuous. There are no discontinuities or leaps in the semitransparent layer, hence one can expect that the absolute value of the function is also continuous. From the shape of the semitransparent layer, one can ascertain that the absolute value of the function grows from bottom to top.

**Function**  $f(z) = \sqrt{1 + \sqrt{z}}$

The construction of Riemann surface of the function  $f(z) = \sqrt{1 + \sqrt{z}}$  was described in details in Example 2.9. The algorithm takes  $\alpha$  to be the positive value  $+\sqrt{1/2}$  of  $\sqrt{1/2}$  and labels the branches  $h_1, \dots, h_4$  of  $h$  near  $z = 1/2$ , so that they take the distinct values  $\sqrt{1 + \alpha}$ ,  $\sqrt{1 - \alpha}$ ,  $-\sqrt{1 + \alpha}$  and  $-\sqrt{1 - \alpha}$  respectively, to compute the color and the height. The visualization of each layer separately after eight iterations of adaptive subdivision can be seen in Fig. 4.16 (right). For the whole graph composed from these four layers, see Fig. 4.16 (left). Recall, that the function is a four-valued function with two branch points at 0, 1 (the point  $\infty$  belongs to the set of branch points, if the amount of finite branch points is odd). These points are also highlighted in the Fig. 4.16 (bottom left), which depicts the cutouts of the graph of the function. We can see, that the first and second layer intersect in the branch point corresponding to the point  $f(z) = 0$ . In the second branch, the point  $f(z) = 1$  intersects only the second layer and the fourth one,

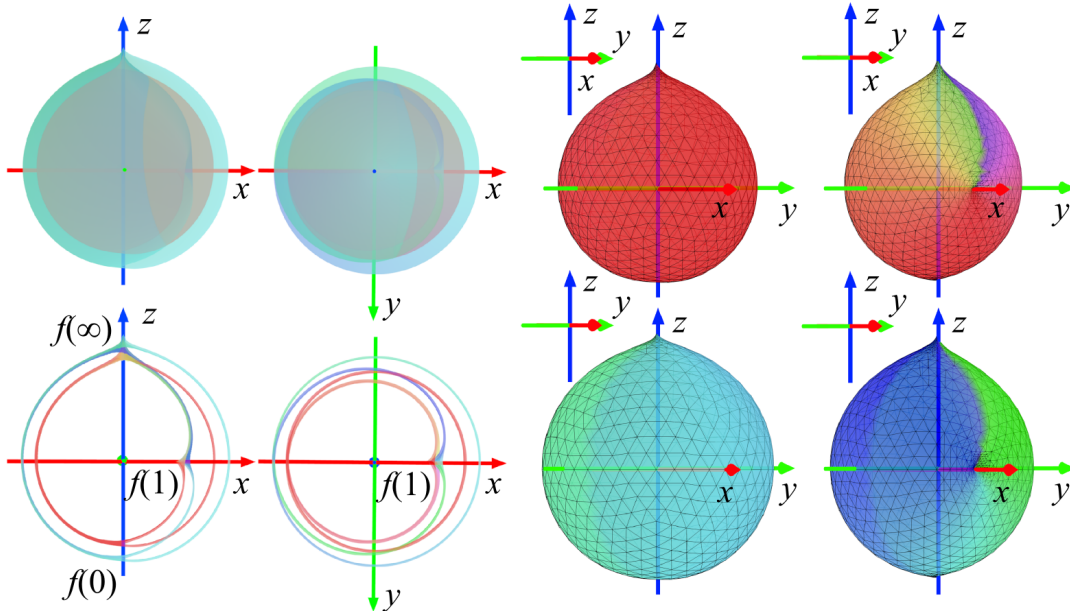


**Figure 4.16:** Visualization of the value of the argument of the function  $f(z) = \sqrt{1 + \sqrt{z}}$  via color scheme. In the two top left figures, we can see the composition of all four layers. In the two bottom left figures, the cutouts of the graph are depicted, so we can see how the layers intersect. In the four figures on the right four separated layers of the graph are depicted.

the first one and the third one are invariant. In the point corresponding to the infinity, all four sheets are joined together in a single branch point, accordingly to the theory of the construction of the Riemann surface introduced in Example 2.9. As we can see in the figure, the second and fourth layer has zero height at the point  $f(1)$ , which is also a zero point for these two branches of the function. The graph has maximal height at the point  $\infty$ .

### Logarithm function

The complex logarithm is a many-valued function with infinitely many branches. The branches are computed from equation  $f(z) = \ln r + i(\theta + 2k\pi)$ , where  $z = re^{i\theta}$  is the polar form of the complex number and  $k \in \mathbb{Z}$ . In our visualization, see Fig. 4.17, the algorithm visualized composition of six branches of the complex logarithm function  $\log(z)$ . From the cutouts it is visible, that the function has

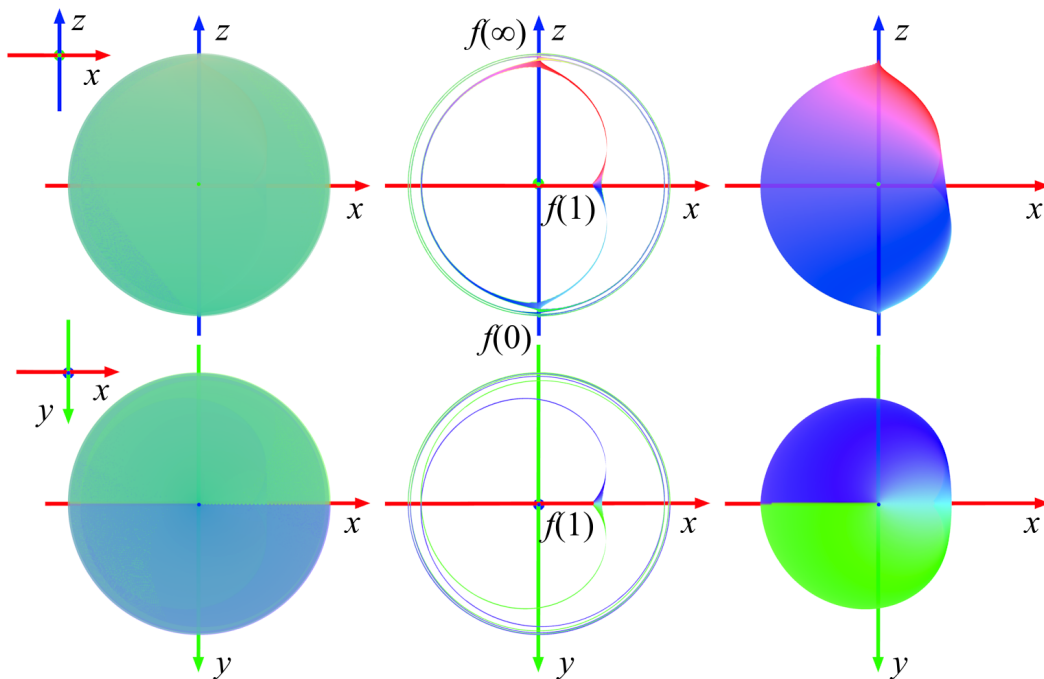


**Figure 4.17:** The composition of six layers of the function  $f(z) = \log(z)$  given by  $\log(z) = \ln r + i(\theta + 2k\pi)$ ,  $k \in \{-3, -2, -1, 0, 1, 2\}$  from two different views (left). The cutouts of the graph (middle) and the principal branch (right).

zero point at  $f(1)$  only for one branch of the function and branch points are at 0 and  $\infty$ . The branch cut  $l = \{z < 0, z \in \mathbb{R}\}$  is visible on the visualization of the principal branch of the logarithm  $\text{Log}(z)$ , see Fig. 4.17(right).

### Inverse trigonometric functions

The inverse trigonometric functions are also many-valued functions with infinitely many branches. To visualize such a function, one has to choose, how many layers should the algorithm visualize. The program visualizes layers of the function given by  $f(z) = \arcsin(z) + k\pi$ , where  $\arcsin(z)$  is the principal branch of the function and  $k \in \mathbb{Z}$ . The composition of six layers from two different views of  $f(z) = \arcsin(z)$  is depicted in Fig. 4.18(left). The cutouts in the middle show the branch points  $-1$  and  $1$ . The function has a simple zero at 0. On the principal

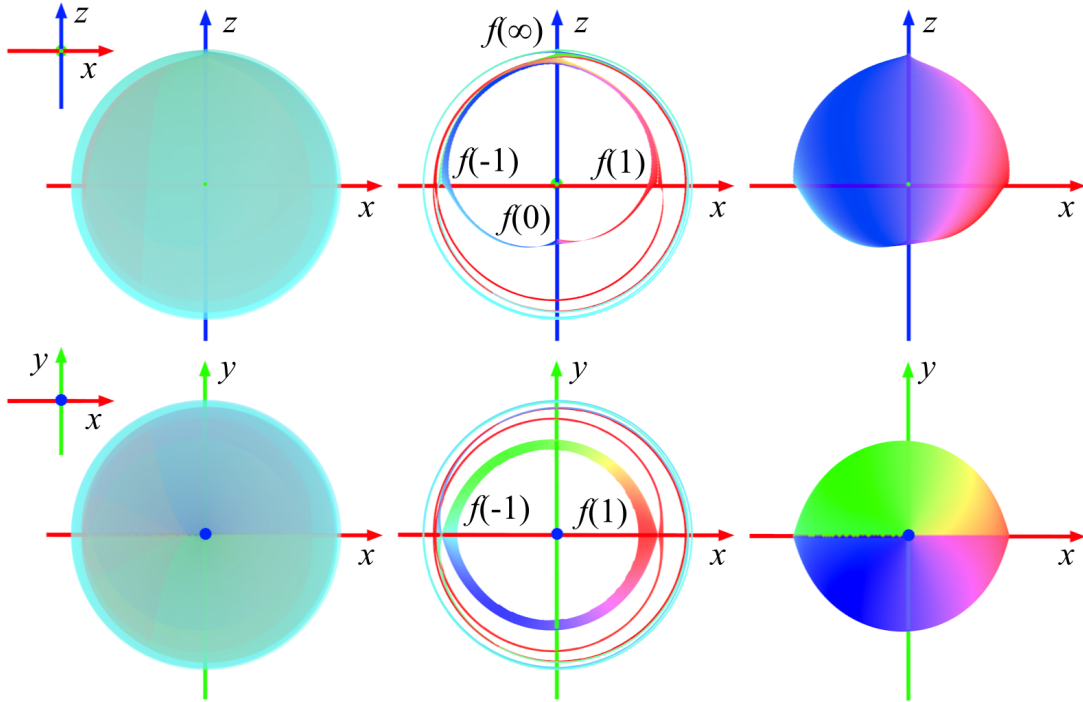


**Figure 4.18:** The figure depicts composition of six layers of the function  $f(z) = \arcsin(z) + k\pi$ , for  $k \in \{-3, -2, -1, 0, 1, 2\}$  from two different angles (left), the cutouts of the graph (middle) and the principal branch of  $\arcsin(z)$  (right).

branch of the  $\arcsin(z)$  Fig. 4.18 (right) the branch cuts  $l_0 = \{z > 1, z \in \mathbb{R}\}$  and  $l_1 = \{z < -1, z \in \mathbb{R}\}$  are visible.

### 4.3 Other examined techniques of visualization

We have experimented with other method of coloring of the graph. This method gives us an advantage of having image of the modulus of the function. But this method is more time consuming in comparison with the one using vertex coloring. Also the texture mapping and adaptive subdivision are more complicated problems to solve.

The previous visualizations of multi-valued function used modulus to compute the color of the graph and argument to compute the height of the graph. These approach seemed to be less intuitive, than the final one.



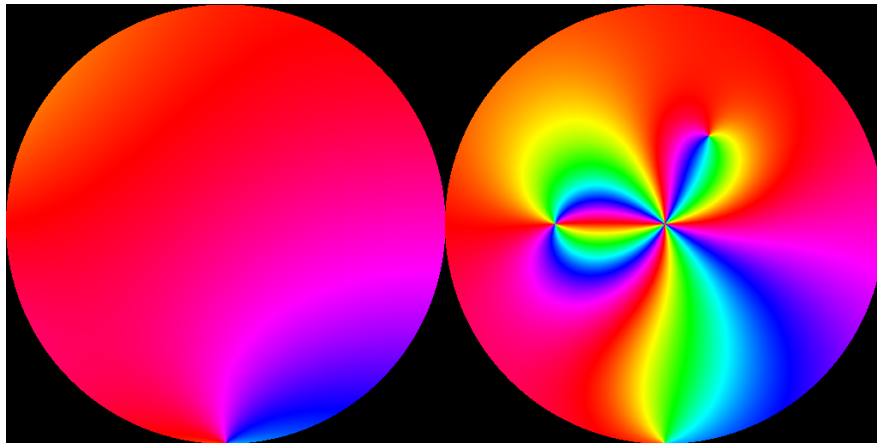


**Figure 4.19:** Texture used to color the visualization of the function  $f(z) = (z + 2)^2(z - 1 - 2i)(z + i)$ . The left circle corresponds to the unit circle in  $\mathbb{C}$ , the values from the exterior of the unit circle are transformed by the function  $J(z) = 1/z$  and the argument  $\arg(w)$  is altered by  $-\arg(w)$  and drawn in the right circle. We can see, that the function has 2 simple and one double zero. The pole in  $\infty$  is a quadruple pole.

The algorithm can also be used with other height functions, than the chosen one. We have come to a conclusion, that the height function  $H(z)$  should be periodic, continuous and bounded for  $H(\infty)$ . One can also use other color schemes, like black and white color scheme, or checkerboard texture.

### Visualization using texture mapping

We have also experimented with a technique of coloring of the 3D model in Blender by a texture [Val10b, Val10a]. First, the algorithm created a texture. The size of the image can be changed by a user requirement. In our visualization, a texture with resolution  $1024 \times 512$  was used, which provides sufficient details. To create the texture, the algorithm used same color scheme, as for coloring vertices, see Fig. 4.3. The image is divided into two circles. The left part depicts the interior of the unit circle. The values from the exterior of the unit circle are transformed by the function  $J(z) = 1/z$  and the argument  $\arg(w)$  is altered by  $-\arg(w)$  drawn in the right part of the picture, see Fig. 4.19.

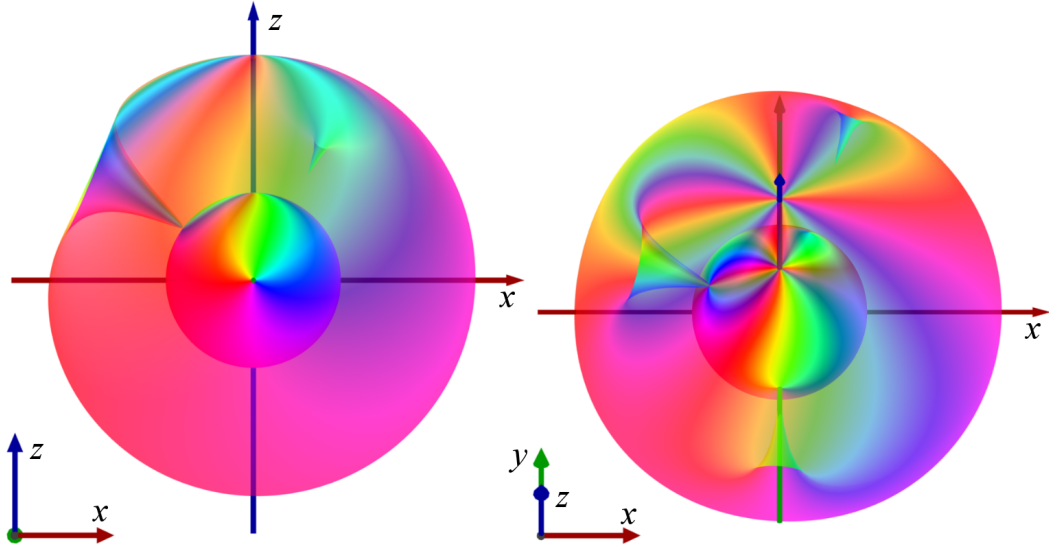


**Figure 4.20:** Visualization of the function  $f(z) = (z + 2)^2(z - 1 - 2i)(z + i)$ .

Such a texture can be mapped on a given mesh object. The visualization uses same mesh  $M$  as the previous method, the sixth subdivision of the icosahedron with 10242 vertices. The material has switched on the texture button. The vertices of the polyhedron  $M$  are divided into two sets. The set  $A$  contains vertices with non-negative  $z$  axis and the set  $B$  contains the remaining vertices. The texture coordinates of vertices from the set  $A$  are computed as follows

$$u = \frac{x}{4(1 + |z|)} + 0.25, \quad (4.8)$$

$$v = \frac{y}{4(1 + |z|)} + 0.25. \quad (4.9)$$

The equations (4.8) and (4.9) are composed from the stereographic projection, scaling and translation. This has to be done, because the texture in Blender has coordinates from interval  $[0, 1]$ , where the point  $(0, 0)$  is situated in the left bottom corner. The computation of the coordinates from the set  $B$  is similar, except the translation uses vector  $p = (0.25, 0.75)$ .

In the last step, the algorithm computes the distance of the vertices from the unit sphere from the absolute value of the function by the height function  $H(z)$ , as



**Figure 4.21:** The color scheme used in reversed method for coloring the graph by the absolute value of the complex function.

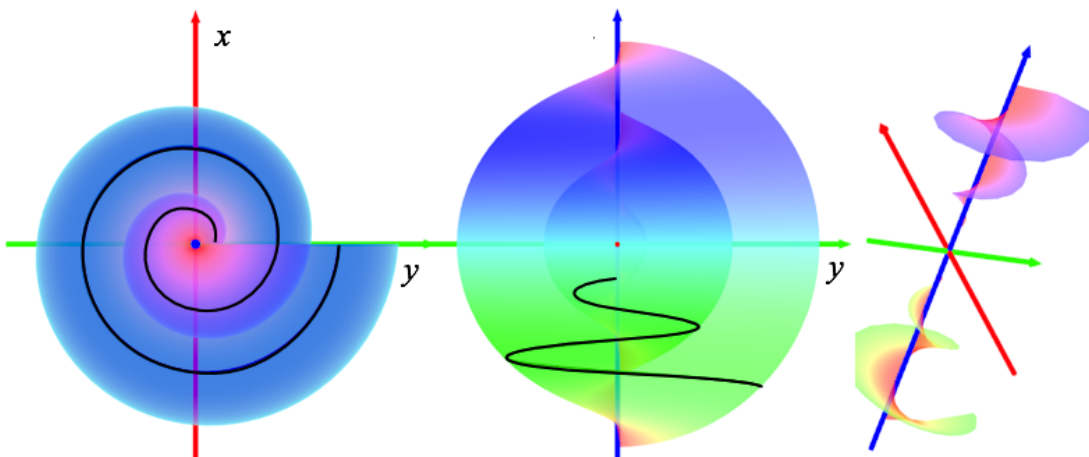


**Figure 4.22:** The figure shows visualization of the function  $f(z) = \sqrt{z}$  created by the reversed method. (Left) top view, (middle) front view, (right) a cone cutout of the graph. In the left and middle figure, the spiral highlight the absolute value for  $r \doteq 0.4$ .

in the previous method. The final visualization corresponds to the visualization created by the coloring of the vertices, see Fig. 4.20. The benefit of this method is in the texture, which depicts the change of the argument.

## Reversed method

Another approach of visualizing the complex function is by calculating the color from the absolute value of the function and using argument to compute the height of the function [VC12]. The absolute value determines the color of the vertex, see Fig. 4.21. The value of the argument of the complex number is used to compute the distance of the vertex from the unit sphere  $\mathbb{S}^2$ . The argument of  $z = 0$  and  $z = \infty$  is not defined, so the value is calculated by limit, if it exists.

Riemann surface of  $f(z) = \sqrt{z}$  created by this method can be seen in Fig. 4.22. In the top view (left figure), the graph forms a spiral. This means, that by

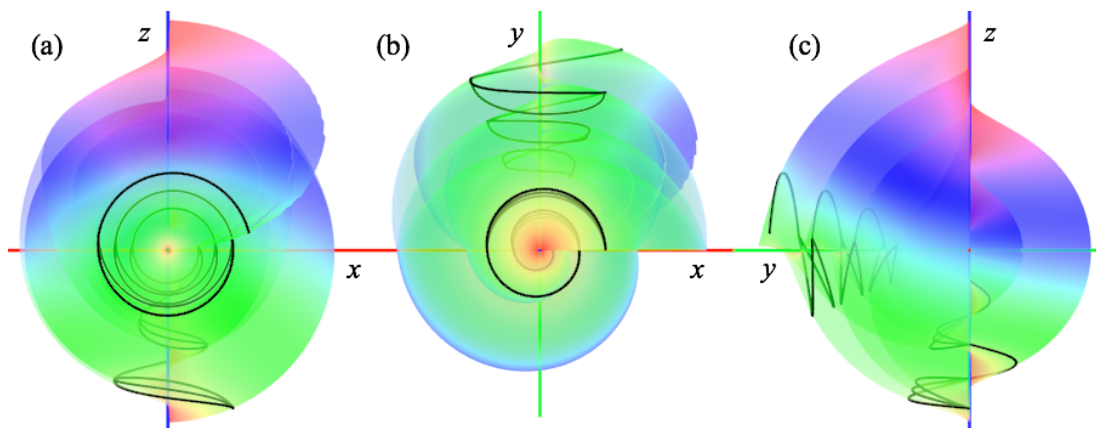


**Figure 4.23:** Visualization of Riemann surface of the function  $f(z) = \sqrt{z} \sqrt[3]{z+i}$  (a) from the front view, (b) from the top view, (c) from the rear view. The spirals highlight images of circles with center in  $0, -i$  and radius  $r \doteq 0.2$ . Notice the intersection of layers in (c) caused by the different roots.

following a circle clockwise around the point 0, the value of the argument will grow. In the middle figure, the orange color can be found in the neighborhood of the point 0. This indicates, that values of the modulus are close to zero. The purple color can be found in the top of the graph, that corresponds to the point in infinity. This means, that the values of the modulus around this point are high and the function has pole in this point. From the front view, it is visible, that the values of the modulus grow from the bottom to top of the graph. The color scheme changes continuously, so one can assume, that the change of the absolute value of the function is also continuous. In the left and the middle figure, a highlighted image of a circle with radius  $r \doteq 0.4$  and center 0 is shown.

In the right figure, cone cutouts of the graph around point 0 and  $\infty$  are depicted. In the neighborhood of this point, the Riemann surface has a shape of a spiral, what indicates, that this two points are branch points of the function  $f(z) = \sqrt{z}$ . To get from the start of the Riemann surface to its end, one has to make two rotations around the branch points, so one can assume, that the function has two sheets.

Let us take a closer look on more complicated example of visualization of the Riemann surface of  $f(z) = \sqrt{z} \sqrt[3]{(z+i)}$ , see Fig. 4.23. The function is a composition of two different roots. Therefore, one has to convert the formula to

a common root with degree computed as least common multiple. In our case, the formula has the following form  $f(z) = \sqrt[6]{z^3(z+i)^2}$ . The visualization depicts the sixth root, so it has six layers. In the figure, one can see, that around 0 is three times double spiral and around  $-i$  is two times triple spiral. This explains the following paragraph.

Consider a circle  $z = re^{i\theta}$  with  $r < 1, \theta \in [0, 2\pi]$  with center in the singular point 0. After the substitution in  $\sqrt[6]{z^3(z+i)^2}$  one gets  $\sqrt[6]{(re^{i\theta})^3(re^{i\theta} + 1e^{i\pi/2})^2} = \sqrt{r}e^{i(\theta/2)}\sqrt[3]{re^{i\theta} + 1e^{i\pi/2}}$ . The circle contains only one singular point of the given function, therefore the change of the layers is affected only by the square root. The cube root causes only a deformation of the given circle. After one turn around the singular point along the circle, one pass from the first layer to the second layer. After the second turn, one pass from the second layer to the first layer. The final surface has six layers, so this procedure can be repeated three times. Thus one gets three times double spiral. The spiral always starts at the point  $r^{1/2}(r+e^{i\pi/2})^{1/3}$ . The spiral around the point  $-i$  is constructed analogously.

Layers intersect between the roots of the function. This is caused by the choice of the projection of the Riemann surface to the three-dimensional space. Notice the two branch cuts, one starts at the branch point 0 and leads along the half-line  $l_0 = \{z \in \mathbb{R}; z \geq 0\}$  and the second one starts at the branch point  $-i$  and leads along half-line  $l_{-i} = \{z \in \mathbb{C}; \Re(z) \geq 0, \Im(z) = -i\}$ .

### Experimenting with various height functions

Before the final selection of the height function  $H(z)$  (4.2), was made, we have experimented with a different height function

$$H(z) = \arctan(|f(z)|) \cdot \arg(f(z)), \tag{4.10}$$

see [Val13, BVC13]. The disadvantage of such a height function was in the disambiguity of the final graphs around the poles, see Fig. 4.24. This technique also

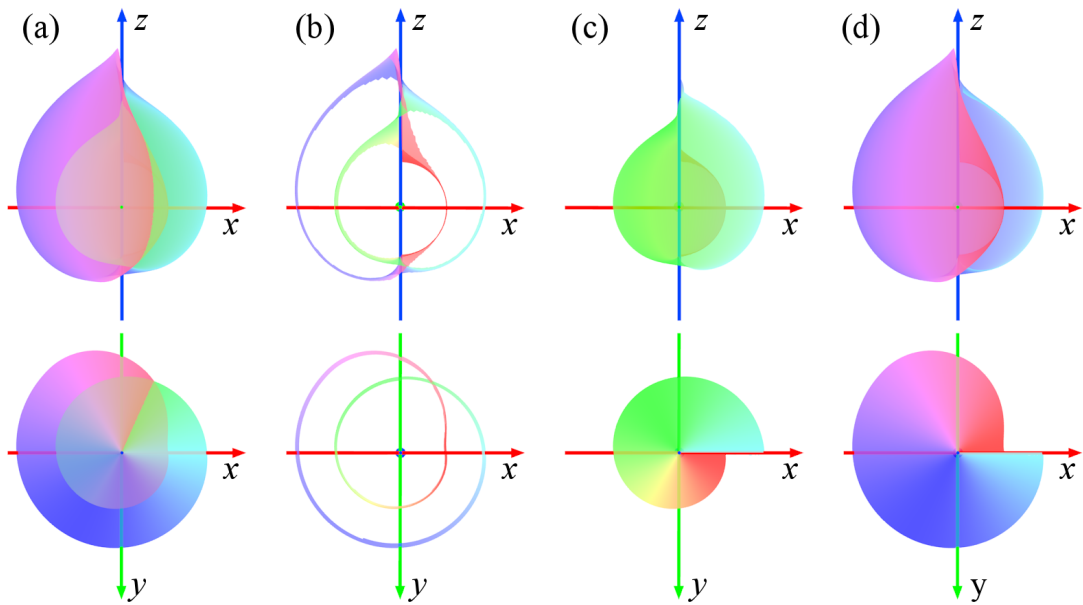


**Figure 4.24:** The figures display the Riemann surface of the square root created by the height function (4.10) from two different points of view – top row the front view, bottom row the top view. (a) the composition of all two layers of the function, (b) the cutout of the graph, (c) the first layer, (d) the second layer.

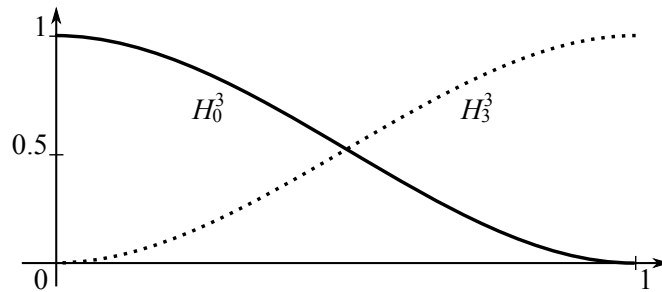


**Figure 4.25:** The figure shows Hermite polynomials  $H_0^3(t) = 2t^3 - 3t^2 + 1$  and  $H_3^3(t) = -2t^3 + 3t^2$  used to eliminate the discontinuity of layers around values of argument close to  $2\pi$  and  $0$ .

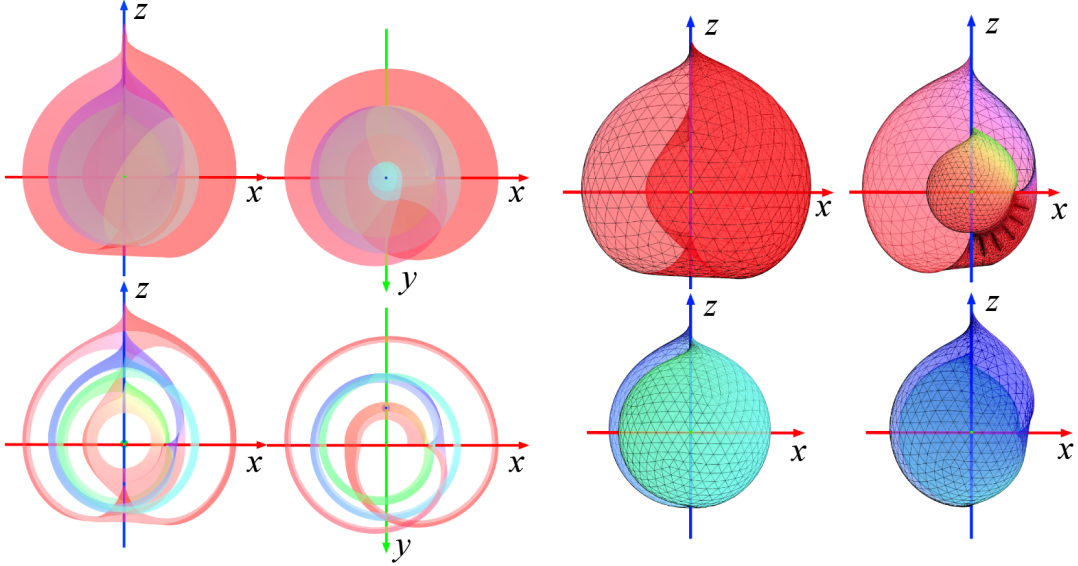


**Figure 4.26:** The figure depicts of the function  $f(z) = \sqrt{1 + \sqrt{z}}$ . The left four figures depict composition of all four layers from two different views and their cutouts. The four figures in the right show four layers separately. The figures are created by the height function given by (4.10).

caused a discontinuity of the layers around values of argument close to  $2\pi$  and 0. To remove the discontinuity a crossing function

$$A_{new}(z, t) = H_0^3(t)A_0(z) + H_3^3(t)A_1(z), \quad (4.11)$$

was used to connect the corresponding layers together, where  $t = 1 - (\pi - \arg(z))/\pi$ ,  $\arg(z) > \pi$  and

$$\begin{aligned} H_0^3(t) &= 2t^3 - 3t^2 + 1 \\ H_3^3(t) &= -2t^3 + 3t^2 \end{aligned} \quad (4.12)$$

are the Hermite basis functions, see Fig. 4.25, and

$$\begin{aligned} A_0(z) &= 2 \arctan(|h(z)|) \arg(h(z) + 2\pi) \\ A_1(z) &= 2 \arctan(|h(z)|) \arg(h(z)) \end{aligned} \quad (4.13)$$

are the heights of the first and last layer.

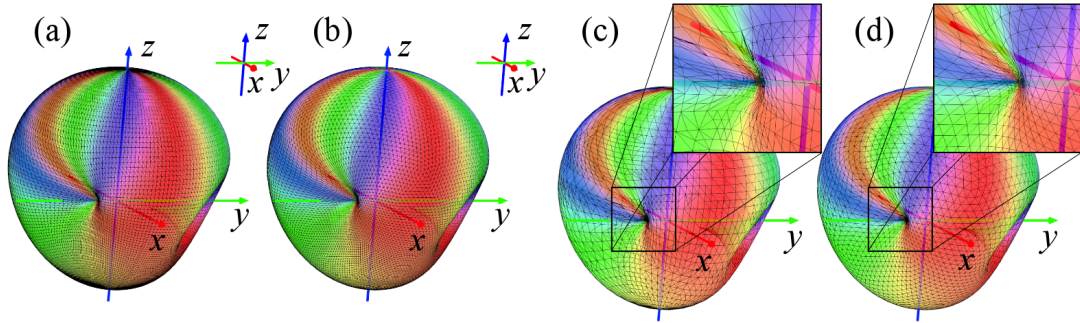


**Figure 4.27:** Model of  $f(z) = (z - 0.5 + i)^2((0.5 - i)z - 1)$  constructed by (a) the spherical coordinates without the adaptive subdivision, (b) the icosahedron without the adaptive subdivision, (c) the spherical coordinates with 10 iterations of the adaptive subdivision method, (d) the icosahedron with 10 iterations of the adaptive subdivision method.

The result for the function  $f(z) = \sqrt{1 + \sqrt{z}}$  can be seen in Fig. 4.26. The clusters of vertices in the top right figure were caused by the high change of the height of the layer. This is caused by the non-periodicity of the former height function and the new height function removed this problem. One can see, that the graph created by the new height function (4.2) is smoother in the neighborhood of the branch cuts, see Fig. 4.16. Also the layer crossing in the branch point 0 is more transparent.

## 4.4 Experimental results

In our work, we used the interpolation of the sphere by creating a polyhedron constructed by uniform sampling via spherical coordinates. An uneven distribution of the vertices on  $\mathbb{S}^2$  is a disadvantage of this method, if the high changes of the absolute value do not correspond to the areas, where the distribution of the vertices is high. Therefore, we examined other method – sampling of the sphere using icosahedron and its subdivision, see Fig. 4.1. An optimization of these two methods can be done by the adaptive subdivision method. To compare these methods our algorithm calculates maximal error, average error and the Hausdorff error [VC14].



---

## 4. RESULTS

$f(z) = (z - 0.5 + i)^2((0.5 - i)z - 1)$	UV	Ico
subdivision	6	6
vertices	13286	10242
max error	0.071	0.0465
average error	0.00096	0.00094
Hausdorff error	0.071	0.0414
	UV adaptive	Ico adaptive
iteration	6	6
vertices	2977	3647
max error	0.14	0.056
average error	0.004	0.0026
Hausdorff error	0.051	0.056
	UV adaptive	Ico adaptive
iteration	10	10
vertices	3985	4352
max error	0.0432	0.056
average error	0.003	0.0023
Hausdorff error	0.043	0.056

**Table 4.1:** Comparison of the errors of the graphs of the function  $f(z) = (z - 0.5 + i)^2((0.5 - i)z - 1)$ . The table compares graphs created by non-adaptive method and graphs created with adaptive subdivision method after 6 and 10 iterations.

### Single-valued function

First, let us see how different approaches influences the graph of a single-valued function. We chose the polynomial function  $f(z) = (z - 0.5 + i)^2((0.5 - i)z - 1)$  from Fig. 4.11. To get smooth results without adaptive subdivision, we used the sixth subdivision of icosahedron with 10242 vertices. In this case, the average error equals 0.00094 and the maximal error was 0.0465. To get a similar average error by using spherical coordinates, one needs to use a graph with 13286 vertices. This visualization has average error 0.00096 and the maximal error was 0.071. The results for the graphs created using adaptive subdivision can be read in Table 4.1. After ten iterations, the maximal error is similar to the maximal error for graphs without adaptive subdivision. The slightly higher values of the average errors are caused by the uneven distribution of the vertices around poles. The graphs created after ten iterations of the adaptive subdivision have 30-40% of the number

$g(z) = \sqrt[3]{z + 0.6 + 0.4i}$	UV	Ico
subdivision	6	6
vertices	31830	31755
max error	0.0592	0.1194
average error	0.000654	0.000361
Hausdorff error	0.0189	0.0216
	UV adaptive	Ico adaptive
iteration	6	6
vertices	5170	3866
max error	0.0957	0.0648
average error	0.0026	0.003
Hausdorff error	0.0957	0.0648
	UV adaptive	Ico adaptive
iteration	9	9
vertices	11001	8135
max error	0.054	0.0408
average error	0.00126	0.00147
Hausdorff error	0.054	0.0408

**Table 4.2:** Average, maximal and Hausdorff errors of the graph of the function  $g(z) = \sqrt[3]{z + 0.6 + 0.4i}$ .

of the vertices of the graphs without adaptive subdivision. Fig. 4.27 shows the graphs with adaptive subdivision, which have higher density of the vertices in a neighborhood of zero point (due to the high change of the absolute value).

### Multi-valued function

We also compared these methods in case of the graphs of multi-valued functions  $g(z) = \sqrt[n]{p(z)}$ , where  $p(z)$  is a polynomial function and  $n \in \mathbb{Z}$ ,  $n > 0$ . Let us take a simple example  $g(z) = \sqrt[3]{z + 0.6 + 0.4i}$ , see Fig. 4.28. The function belongs to triple-valued complex functions and it has two singular points  $z_1 = -0.6 - 0.4i$  and  $z_2 = \infty$ , which are also branch points of this function. The model constructed by subdivision of the icosahedron has slightly lower average error than the model constructed by spherical coordinates, see Table 4.2.

The adaptive subdivision method eliminates the discontinuity around the zeros and the poles. In the figure, there is a higher density of vertices, where the

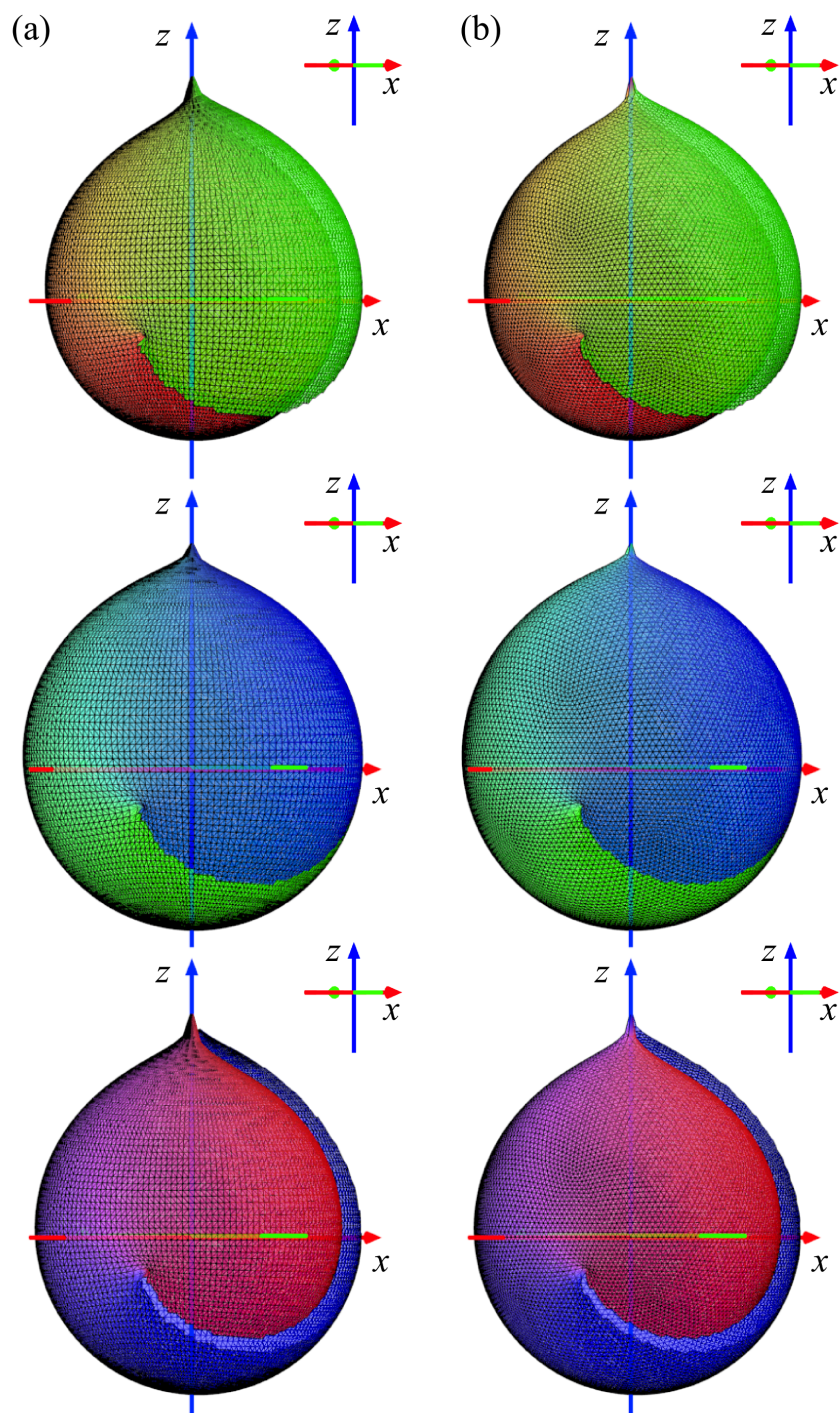


**Figure 4.28:** Model of  $f(z) = \sqrt[3]{z + 0.6 + 0.4i}$  from the front view constructed by (a) the spherical coordinates with 31830 vertices, (b) the icosahedron with 31755 vertices. The final model is composed of the three pictured parts.

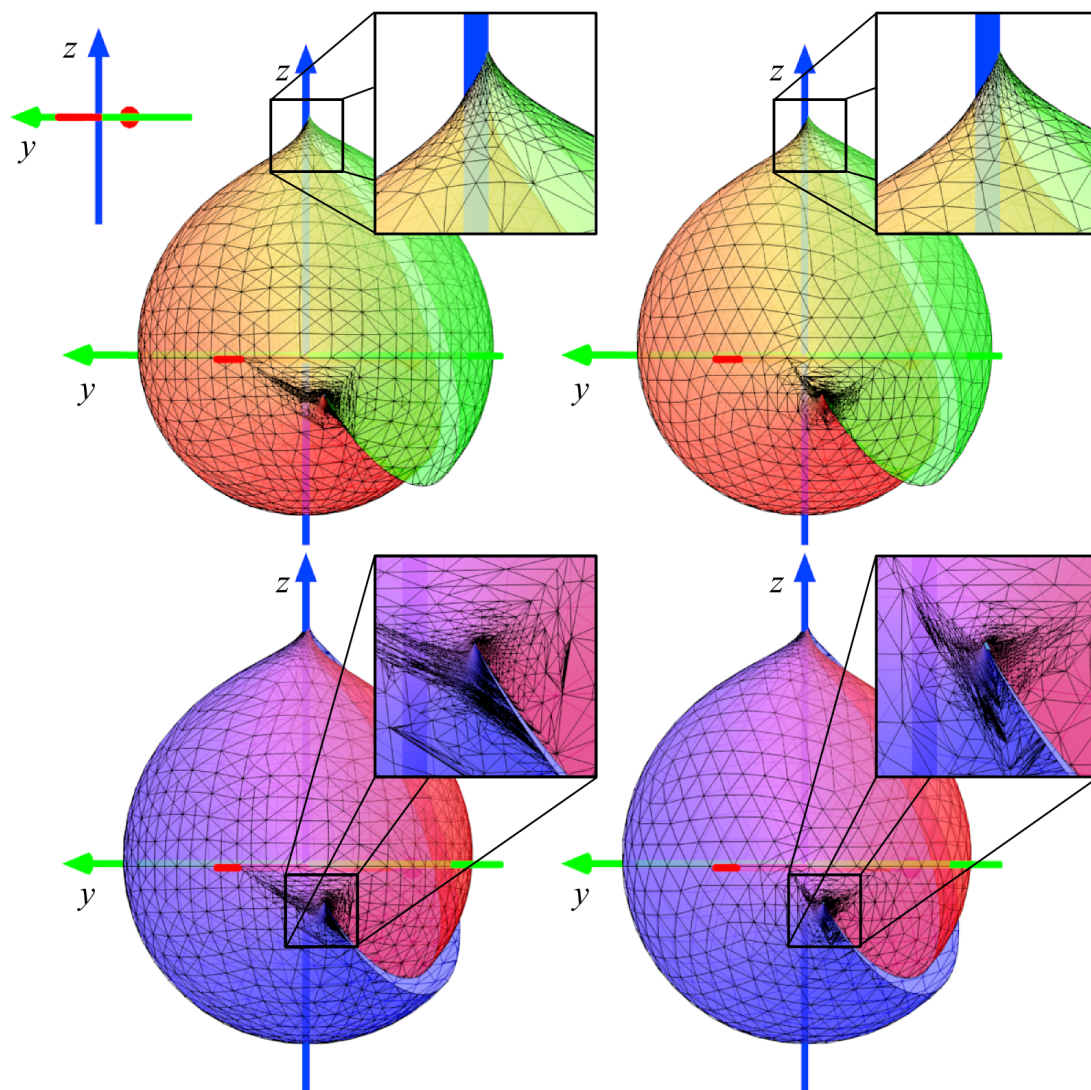


**Figure 4.29:** In the top, we can see the distribution of vertices in the neighborhood of the singular point at infinity. The bottom figure depicts the distribution of vertices near the root of the function, where the curvature is higher.

$h(z) = \sqrt{1 + \sqrt{z}}$	UV	Ico
subdivision	6	6
vertices	40888	40968
max error	0.152	0.1423
average error	0.001	0.0004
Hausdorff error	0.152	0.045
	UV adaptive	Ico adaptive
iteration	6	6
vertices	4757	3615
max error	0.1302	0.1131
average error	0.0037	0.0043
Hausdorff error	0.0748	0.0312
	UV adaptive	Ico adaptive
iteration	8	8
vertices	5118	6723
max error	0.0905	0.0874
average error	0.0034	0.0041
Hausdorff error	0.0905	0.0264

**Table 4.3:** Average, maximal and Hausdorff errors of the graph of the function  $h(z) = \sqrt{1 + \sqrt{z}}$ .

curvature of the mesh is higher, see Fig. 4.29. In the table, we can see the sum of vertices for the first, the second and the third layer. The graphs created after nine iterations of the adaptive subdivision have 25-35% of the number of the vertices of the graphs created without adaptive subdivision. Because the adaptive subdivision is based on the computation of the angle of the normals in the vertices of the model, it is natural, that the layers have different number of vertices. For example, the model created by the adaptive subdivision of the icosahedron after eight iterations has 2202 vertices in the first layer, 2192 vertices in the second and 2329 vertices in the third layer. It also causes difference between the average error and the maximal error in the first, the second and the third layer.

To visualize a more complicated complex function, we have created the Riemann surface of  $h(z) = \sqrt{1 + \sqrt{z}}$  from the Sec. 2.9. The visualization can be seen in Fig. 4.16.

## 4. RESULTS

UV subdivision 6	$f(z)$	$g(z)$	$h(z)$
$\epsilon \in (1, 10^{-1}]$	0 (0%)	0 (0%)	338 (0.29%)
$\epsilon \in (10^{-1}, 10^{-2}]$	223 (0.73%)	491 (0.53%)	256 (0.22%)
$\epsilon \in (10^{-2}, 10^{-3}]$	14955 (48.78%)	2171 (2.33%)	2934 (2.54%)
$\epsilon \in (10^{-3}, 10^{-4}]$	12858 (41.94%)	80458 (86.38%)	105912 (91.69%)
$\epsilon \in (10^{-4}, 10^{-5}]$	1984 (6.47%)	8599 (9.23%)	3827 (3.31%)
$\epsilon \in (10^{-5}, 10^{-6}]$	640 (2.09%)	1386 (1.49%)	2003 (0.21%)
$\epsilon < 10^{-6}$	0 (0%)	42 (0.05%)	244 (0.21%)
Ico subdivision 6	$f(z)$	$g(z)$	$h(z)$
$\epsilon \in (1, 10^{-1}]$	0 (0%)	1 (0%)	11 (0.01%)
$\epsilon \in (10^{-1}, 10^{-2}]$	49 (0.16%)	61 (0.07%)	45 (0.04%)
$\epsilon \in (10^{-2}, 10^{-3}]$	6779 (22.07%)	743 (0.80%)	678 (0.55%)
$\epsilon \in (10^{-3}, 10^{-4}]$	23239 (75.65%)	91494 (98.18%)	121029 (98.48%)
$\epsilon \in (10^{-4}, 10^{-5}]$	581 (1.98%)	805 (0.86%)	1025 (0.83%)
$\epsilon \in (10^{-5}, 10^{-6}]$	72 (0.23%)	80 (0.09%)	92 (0.07%)
$\epsilon < 10^{-6}$	0 (0%)	3 (0%)	14 (0.01%)

**Table 4.4:** Comparison of the distribution of the errors of the graphs of the functions  $f(z) = (z - 0.5 + i)^2((0.5 - i)z - 1)$ ,  $g(z) = \sqrt[3]{z + 0.6 + 0.4i}$  and  $h(z) = \sqrt{1 + \sqrt{z}}$  for non-adaptive subdivision method.

The errors and the number of vertices for the function  $h(z)$  are summarized in Table 4.3. After eight iterations, the visualizations have similar maximal and average error as the visualizations without the adaptive subdivision. The advantage of the graphs constructed using the adaptive subdivision is lower count of vertices of the final graph and higher density in places with the angle between the normals in the adjacent vertices bigger than the chosen threshold, particularly in the neighborhood of the root of the function and the infinity.

Let us take a closer look at the distribution of errors of graphs. In Table 4.4 and Table 4.5, we can see the number of errors in interval  $(10^{-i}, 10^{-(i+1)}]$ ,  $i = 0, \dots, 6$  and the count of points with smaller error. The number of errors, which are close to the maximal error, is low in comparison to the whole amount of errors. The graphs have the most error values around the value of the average error.

The next study was oriented on the dependence of the Hausdorff error and the maximal error. In our algorithm, we have implemented computation of only one

## 4. RESULTS

UV adaptive 8	$f(z)$	$g(z)$	$h(z)$
$\epsilon \in (1, 10^{-1}]$	0 (0%)	0 (0%)	0 (0%)
$\epsilon \in (10^{-1}, 10^{-2}]$	295 (2.76%)	69 (0.26%)	223 (1.45%)
$\epsilon \in (10^{-2}, 10^{-3}]$	7525 (10.30%)	10540 (39.92%)	12175 (79.42%)
$\epsilon \in (10^{-3}, 10^{-4}]$	2658 (24.83%)	10096 (38.24%)	2595 (16.93%)
$\epsilon \in (10^{-4}, 10^{-5}]$	198 (1.85%)	4873 (18.46%)	305 (1.99%)
$\epsilon \in (10^{-5}, 10^{-6}]$	28 (0.26%)	745 (2.82%)	32 (0.21%)
$\epsilon < 10^{-6}$	0 (0%)	80 (0.30%)	0 (0%)
Ico adaptive 8	$f(z)$	$g(z)$	$h(z)$
$\epsilon \in (1, 10^{-1}]$	0 (0%)	0 (0%)	0 (0%)
$\epsilon \in (10^{-1}, 10^{-2}]$	98 (0.81%)	40 (0.20%)	91 (0.78%)
$\epsilon \in (10^{-2}, 10^{-3}]$	8883 (73.46%)	7381 (36.61%)	9253 (79.68%)
$\epsilon \in (10^{-3}, 10^{-4}]$	2702 (22.34%)	8255 (40.94%)	1992 (17.15%)
$\epsilon \in (10^{-4}, 10^{-5}]$	376 (3.11%)	3906 (19.37%)	244 (2.10%)
$\epsilon \in (10^{-5}, 10^{-6}]$	34 (0.28%)	526 (2.61%)	33 (0.28%)
$\epsilon < 10^{-6}$	0 (0%)	55 (0.27%)	0 (0%)

**Table 4.5:** Comparison of the distribution of the errors of the graphs of the functions  $f(z) = (z - 0.5 + i)^2((0.5 - i)z - 1)$ ,  $g(z) = \sqrt[3]{z + 0.6 + 0.4i}$  and  $h(z) = \sqrt{1 + \sqrt{z}}$  for adaptive subdivision method.

side of the Hausdorff error. This means, that we looked for the greatest distance between the mesh and the graph of the function. We used discretely sampled values of the graph – the middle point of each edge of the mesh of the graph. Then, we computed the distance from the middle of the edge to each point on the grid. The minimum of these values represent the approximation of the distance of the middle of the edge from the continuous graph of the function. The maximum of these minimal values is the approximation of Hausdorff error. The Table 4.6 compares the Hausdorff errors with the maximal errors. However, in many cases, the denser is the sampling, the closer is the ratio to 1.

Table 4.7 shows the position of the maximal error. We can see, that the error is always near a singular point of the function. In the case of the chosen single-valued function  $f(z) = (z - 0.5 + i)^2((0.5 - i)z - 1)$ , the maximal error is near the simple singular point in  $z = 0.4 + 0.8i$ . For the chosen many-valued functions  $g(z) = \sqrt[3]{z + 0.6 + 0.4i}$  and  $h(z) = \sqrt{1 + \sqrt{z}}$ , the maximal error is situated in the neighborhood of the infinity or near the singular point.

UV		sub 3	sub 4	sub 5	sub 6
$f(z)$	Hausdorff error	0.251	0.358	0.26	0.087
	Maximal error	0.251	0.358	0.26	0.087
	Ratio	1	1	1	1
$g(z)$	Hausdorff error	0.1671	0.154	0.1284	0.019
	Maximal error	0.1671	0.358	0.1284	0.0592
	Ratio	1	1	1	3.116
$h(z)$	Hausdorff error	0.207	0.2	0.178	0.152
	Maximal error	0.207	0.2	0.178	0.152
	Ratio	1	1	1	1
Ico		sub 3	sub 4	sub 5	sub 6
$f(z)$	Hausdorff error	0.511	0.307	0.116	0.041
	Maximal error	0.543	0.307	0.196	0.047
	Ratio	1.063	1	1.69	1.146
$g(z)$	Hausdorff error	0.052	0.054	0.041	0.0212
	Maximal error	0.125	0.101	0.0805	0.119
	Ratio	2.404	1.87	1.963	5.613
$h(z)$	Hausdorff error	0.144	0.093	0.066	0.045
	Maximal error	0.21	0.192	0.167	0.142
	Ratio	1.46	2.06	2.53	3.16

**Table 4.6:** Comparison of the Hausdorff error and the maximal error for different subdivision of the icosphere and UV sphere.

## 4.5 Visualization of the deformation of ADE singularities

Our technique of visualization of the complex functions was used in visualizations of the deformation of ADE singularities. Very briefly, such a singularity can be deformed only to a finite number of other ADE singularities by a suitable deformation. More precise description is out of the scope of this paper and can be found in [BVC13], [AGZV12, GLS07].

The technique of deformations is a fundamental method in e.g. algebraic geometry and related mathematical disciplines; in Computer Graphics, the deformations are used e.g. in morphing. However, the visualizations of deformations of complex functions are very rare according to the authors knowledge.



---

## 4. RESULTS

---

	UV sub 6	Ico sub 6	root
$f(z)$	$0.398 + 0.779i$	$0.4 + 0.789i$	$0.4 + 0.8i$
$g(z)$	$94.54 - 0i$	$-0.603 - 0.399i$	$-0.6 - 0.4$
$h(z)$	$99.783 - 0i$	$154.196 - 0i$	$\{0, 1\}$
	UV adaptive 8	Ico adaptive 8	root
$f(z)$	$0.942 - 1.359i$	$0.389 + 0.891i$	$0.4 + 0.8i$
$g(z)$	$-0.6 - 0.397i$	$-0.599 - 0.397i$	$-0.6 - 0.4$
$h(z)$	$864.367 - 0i$	$978.207 - 0i$	$\{0, 1\}$

**Table 4.7:** Position of the maximal error in graphs for functions  $f(z) = (z - 0.5 + i)^2((0.5 - i)z - 1)$ ,  $g(z) = \sqrt[3]{z + 0.6 + 0.4i}$  and  $h(z) = \sqrt{1 + \sqrt{z}}$ . It is apparent, that all the maximal error are situated near a singular point of a function.

The complexity of ADE singularity is given by its Milnor number, indicated by the subscript  $k$ . The presented continuous blend  $A_k \rightarrow A_{k-1}$  allows us to decrease this number by one, which is the smallest possible step, up to regularity ( $k = 0$ ). The animation comprehensibly captures the changes in the structure. Although the deformation  $\sqrt{a(f - L) - f}$ , where  $f$  is the original function,  $a \in [0, 1]$  is the parameter and  $L$  a linear (=regular) function, is the most effective deformation in the sense that the singularity is removed in one step, this blend is not demonstrative enough, because the changes in the structure are not sufficiently detailed.

Here, we describe in detail the deformation between the  $A_2$  and  $A_1$  singularities in their normal form given by the equations  $A_k: x^{k+1} + y^2$ ,  $k \geq 1$ . For the sake of simplicity, we choose a 1-parameter deformation given by  $f(z) = \sqrt{a(z^3 - z^2) - z^3}$ , where  $a \in [0, 1]$  is the deformation parameter. This system provides a decrease of the Milnor number by one. By changing the parameter, we get a sequence of images demonstrating the change of the topology between  $A_2$  and  $A_1$  singularity at parameter  $a = 1$ . In Fig. 4.30, we see such a sequence for the sampled values of the parameter  $a = 0, 0.4, 0.8, 1$ .

The Milnor number corresponds to the number of sheets, which is necessarily used in a neighborhood of the singularity. Hence, we go from three sheets to two while one collapses.

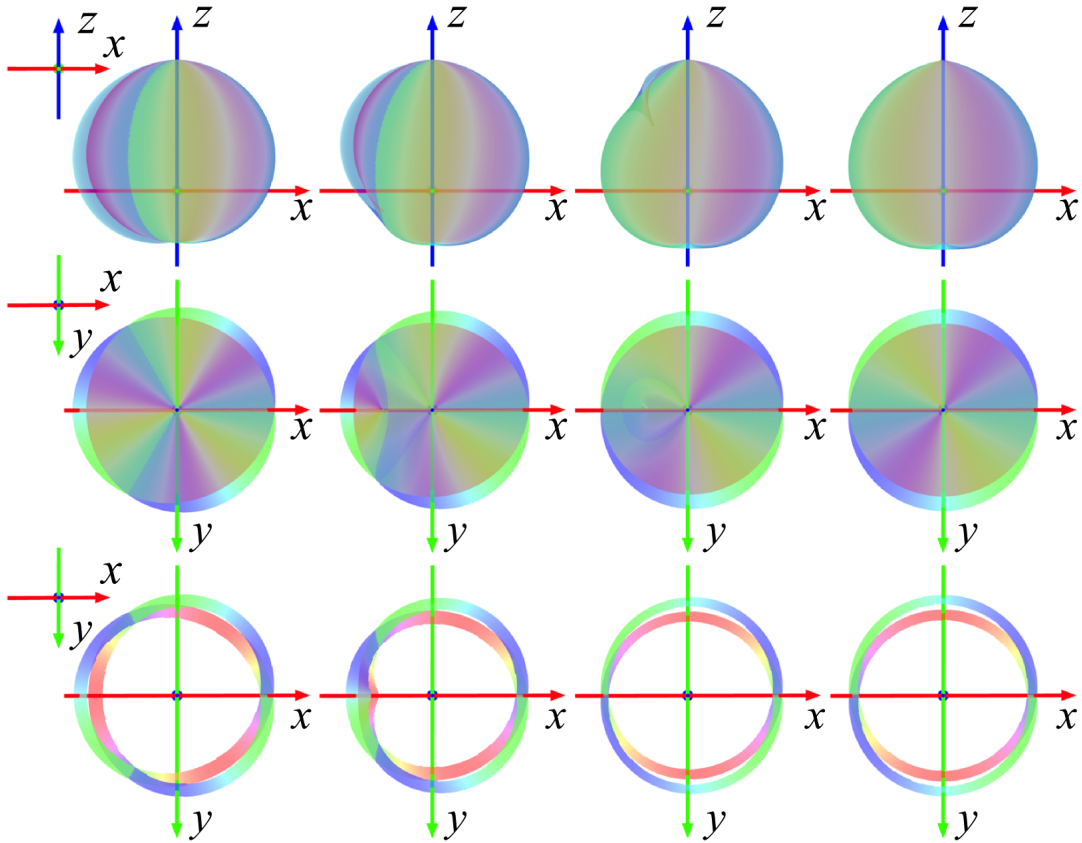


**Figure 4.30:** From left to right, the figure illustrates the changes of the graph of the deformation between the  $A_2$  and the  $A_1$  singularities for the sampled values of the parameter  $a = 0, 0.4, 0.8, 1$ . In the top, the graph is displayed from the top, in the bottom, the graph from the front.

In animations, we used an approximation of a sphere, where meridians are approximated by a polygonal line with 125 vertices and parallel lines approximated by a polygonal line with 250 vertices. To get a continuous final sequence, we changed the values of  $a$  from 0 to 1 by 0.01, getting an animation consisting of 101 different frames.

In Fig. 4.30, the top left figure presents the function  $f(z) = \sqrt{a(z^3 - z^2) - z^3}$  for the parameter  $a = 0$ , i.e.  $f(z) = \sqrt{-z^3}$  which is the cuspidal curve with the  $A_2$  singularity. The next two figures illustrate the change between  $A_2$  and  $A_1$ . We see that one singular point moves along the negative real axis from 0 to  $\infty$ . In the top right figure, we see the Riemann surface of the function  $f(z) = \sqrt{-z^2}$ , i.e. the curve containing the  $A_1$  singularity at origin. Because the exponent is

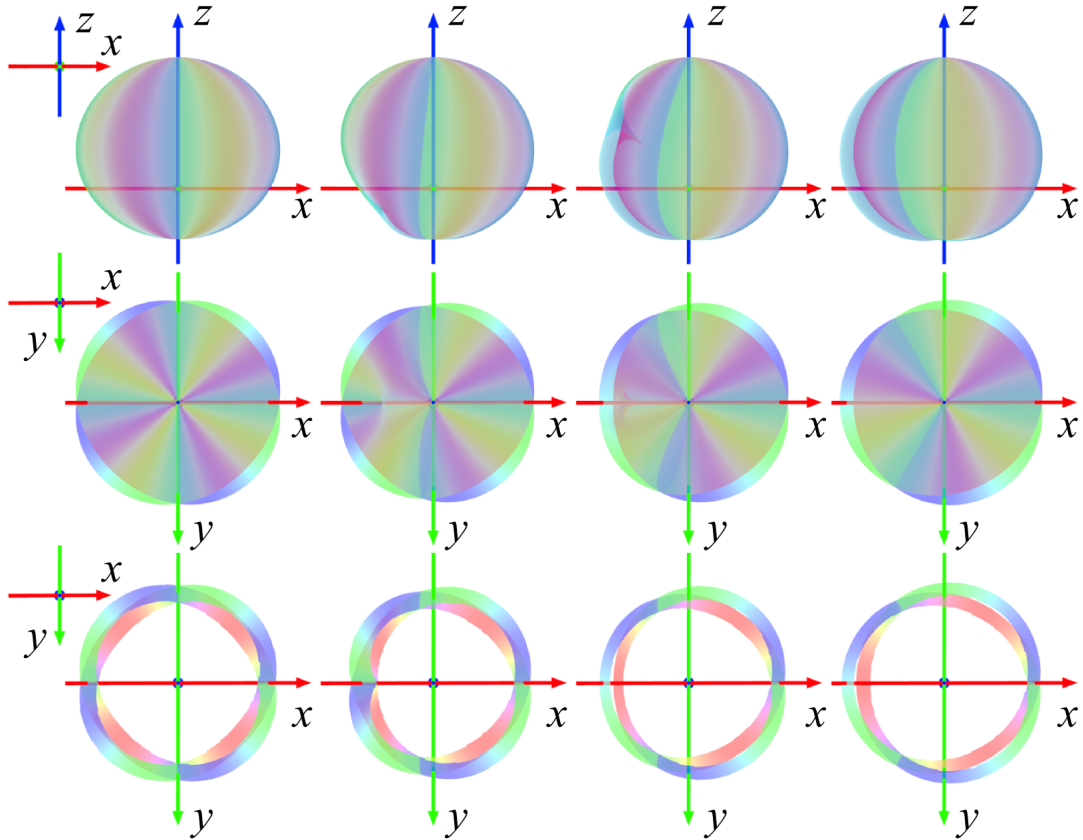


**Figure 4.31:** The figure depicts change between the  $A_3$  and  $A_2$  singularities for the sampled values of the parameter  $a = 0, 0.4, 0.8, 1$ .

even, the surface consists of two separate parts, intersecting in the left side of the right-most figure. The graph has one singular point  $z = 0$  and one singular point at the infinity.

In our work, we have also visualized the deformation between  $A_3$  and  $A_2$  in a similar way, see Fig. 4.31 for a sampled animation.

The 1-parameter system can also be used to visualize change of the graph from one function  $f(z)$  to another complex function  $g(z)$ . We have chosen two functions  $f(z) = \sqrt{1 + \sqrt{z}}$  and  $g(z) = \sqrt{1 + \sqrt[3]{z}}$ . As in the previous example, we used a simple 1-parametric deformation given by equation

$$d(z) = \sqrt{1 + \sqrt{z} + a(\sqrt[3]{z} - \sqrt{z})}, \quad (4.14)$$

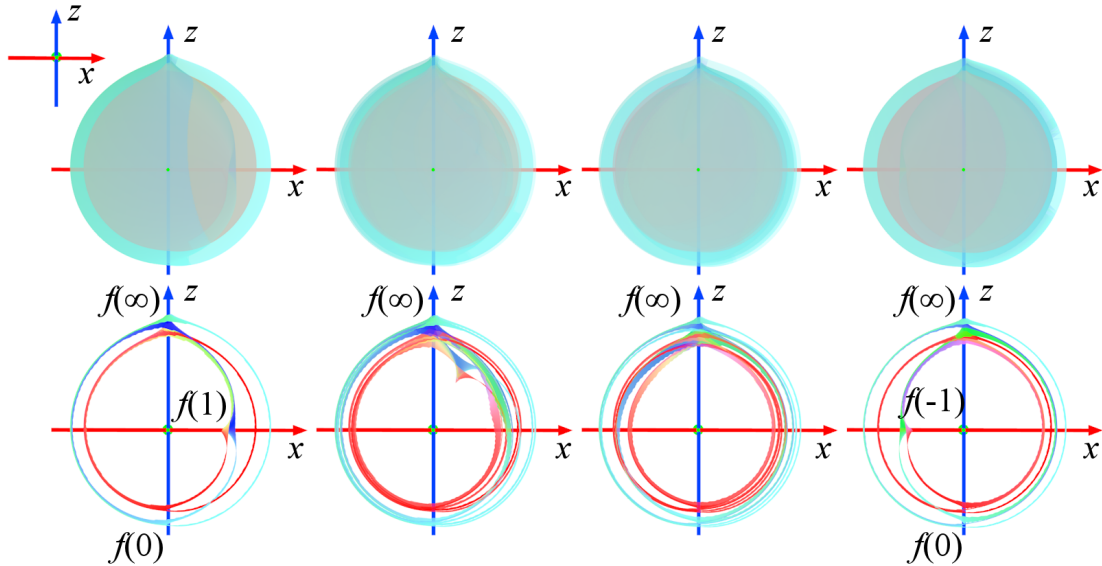


**Figure 4.32:** The change of the graph of the function (4.14) for values of the parameter  $a = 0, 0.3, 0.7, 1.0$  from the front view is demonstrated. In the top row, the figure depicts the composition of all layers and in the bottom row the cut-out of the graph can be seen. We can see, that for the value  $a = 0$  (left) the graph has four layers, for the value  $a = 1$  (right) the graph has six layers and for the remaining values of the parameter  $a$  the graph has twelve layers.

where  $a \in [0, 1]$ . For visualization of the sampled values  $a = 0, 0.3, 0.7, 1$ , see Fig. 4.32. When the parameter  $a = 0$ , the graph has four layers. On the other side, the graph has six layers, when the parameter  $a$  equals to the value 1. All visualizations with the parameter  $a \in (0, 1)$  have twelve layers. It is caused by the presence of the square and the cube root under the square root. We can also see, that the branch point  $z = 1$  in the graph with  $a = 0$  disappears and the graph for  $a = 1$  has a branch point in value  $z = -1$ .

## 4.6 Discussion

The first goal was to visualize single-valued complex functions such as polynomial functions, rational functions and trigonometric functions.

The second goal was to visualize multi-valued complex functions such as root functions and their multiple.

The third goal was to optimize the mesh and to evaluate the results.

We have created a method for visualization of single-valued functions and tested it on functions from these classes. The algorithm creates a visualization of a function over the whole domain, if possible. The point in infinity is visualized as the limit of the function in infinity, if it exists. The zeros and poles are visible in the visualizations with their multiplicities. A user can estimate the behavior of the absolute value and the argument of the function as well. In contrast to the visualizations provided by H. Lundmark [Lun04], K. Poelke [PP09] and others, our method allows a user to study the graph of the complex function over the whole domain of the function.

By introduction of a few changes, the proposed method may be used for visualization of the multi-valued functions. We have tested it on roots of the polynomials and also on the logarithmic function and the inverse trigonometric function. The method visualizes the whole domain of the function with their branch points.

During the implementation a problem how to differ each layer of the graph arose. This problem was solved by vertex groups, that are provided by Blender. Our algorithm creates set of vertex groups corresponding to the amount of layers of the visualized function. Each vertex is assigned to appropriate vertex group. Then the algorithm can calculate correct argument of the complex number. The branch points of the function are handled separately with no vertex group assigned.

An contribution on visualizations of multi-valued functions over the Riemann sphere was made by M. Trott for the Wolfram research [Tro02]. He uses the symbolic derivation and nonlinear equation solver provided by Mathematica and computes 3D plots based on an explicit function definition. M. Trott also visualizes Riemann surfaces over Riemann sphere. He uses the real or imaginary part of the complex number as a height function. This technique leads to many intersections in the model of the Riemann surface. Also the visualizations do not have transparency, so one can not see all layers simultaneously.

The CoFiViS tool is available as a compilation of scripts [Val14] and they are distributed under GNU General Public License [Fou07]. Each script can visualize one class of complex functions. To use the tool, a user has to have basic knowledge about Blender. Some tutorials and documentation can be found in

[Fou14a]. After running the script, a graph of complex function appears in the 3D window. If the chosen amount of vertices is too high, the process can take some time. When the model is created, the user interface provided by Blender allows us to create renders of the graphs, animations, cutouts or separate layers of visualized multi-valued functions. A user can interact with the visualization, what gives a user better idea of the graph of the function.

The algorithm allows us to change the density of vertices of the graph by changing the amount of meridians and parallels of the spherical model or the number of subdivisions of the icosahedron. To improve the mesh and reduce the amount of vertices needed to get a visualization with a small error, we have implemented an adaptive grid method. The methods were compared by the maximal, average and Hausdorff error on chosen types of functions.

# Conclusion

The visualization of a complex valued function is a complicated process, because of the real dimension of the ambient space in which its graph is naturally considered. To visualize a real function  $f: \mathbb{R} \rightarrow \mathbb{R}$ , we draw a graph  $y = f(x)$  in a two dimensional Cartesian coordinate system in  $\mathbb{R}^2$  via identifying one axis with the domain of the function and the other axis with its codomain. This method meets with some difficulties when we want to extend it to a complex function  $g: \mathbb{C} \rightarrow \mathbb{C}$ . The main problem arising is that  $\mathbb{C}$  has a real dimension two, thus we need a four-dimensional real space to depict the graph of a complex function  $w = g(z)$ .

We have presented an overview of methods of the visualization of complex functions. The techniques like domain coloring and visualization using Riemann surfaces mostly depict only part of the domain of the complex function. In our work, we have created a workflow for the visualization of chosen classes of complex functions over the Riemann sphere. This approach lets us visualize functions over the whole domain. To create the graph of the complex valued function, we used icosahedron and its subdivisions or a polyhedron constructed by the spherical coordinates.

Our visualizations depict the change of the modulus and the argument of a complex function. The zero points and poles are clearly visible in the graph together with their multiplicity. In case of multi-valued functions, a user can study the behavior of the graph, structure of Riemann surface in the neighborhood of the branch points of the function and the branch cuts of the function. For better understanding a user can study the graph from different views and create cutouts of the graph and animations.

## CONCLUSION

---

An enhancement of this approach was made by adaptive subdivision, which gave us smooth graph of the complex function with lower number of vertices. To compare this procedures, we have computed maximal error, Hausdorff error and average error of the graph.

Our developed method can be used for visual inspection of complex functions and their deformations. The results were published in the international journal of computer graphics – *The Visual Compute* [VC14] and in conferences SCCG 2013 [BVC13] and SCG 2010, 2012 [VC10, VC12].

In future work, we aim to expand the set of visualized functions, for example by elliptic functions, fractals etc. We want to try different height functions to eliminate the number of intersections of the layers to a minimum and test different methods of adaptive subdivision, e.g. based on maximal error. It would be also interesting to visualize the functions over surfaces with same genus. An implementation of the algorithms in a virtual reality environment could make the visualizations easier to understand to a user.



# References

- [AGZV12] V. I. Arnold, S. M. Gusein Zade, and A. N. Varchenko. *Singularities of Differentiable Maps: Classification of Critical Points, Caustics and Wave Fronts (reprint of the 1985 edition)*. Modern Birkhäuser Classics. Birkhäuser Boston, Inc., 2012.
- [BVC13] M. Bátorová, M. Valíková, and P. Chalmovianský. Desingularization of ade singularities via deformation. *Spring conference on Computer Graphics*, pages 44–51, 2013.
- [Cha08] J. Chalmovianská. Modelovanie a reprezentácia trojrozmerných objektov. [http://fractal.dam.fmph.uniba.sk/~pilnikova/pg/modelovanie\\_reprezentacie.pdf](http://fractal.dam.fmph.uniba.sk/~pilnikova/pg/modelovanie_reprezentacie.pdf), 2008.
- [CL02] C.-C. Chen and C.-S. Lin. Sharp estimates for solutions of multi-bubbles in compact Riemann surfaces. *Comm. Pure Appl. Math.*, 55:728 – 771, 2002.
- [Coh67] H. Cohn. *Conformal Mapping on Riemann Surfaces*. Dover books on advanced mathematics. McGraw-Hill, 1967.
- [Far99] G. Farin. *NURBS for Curve & Surface Design: From Projective Geometry to Practical Use*. A K Peters/CRC Press, 1999.
- [Far00] F. A. Farris. Visualizing complex-valued functions in the plane. [http://www.maa.org/pubs/amm\\_complements/complex.html](http://www.maa.org/pubs/amm_complements/complex.html), 2000.
- [For81] O. Forster. *Lectures on Riemann Surfaces (Graduate Texts in Mathematics)*. Springer, 1981.

- [Fou07] Free Software Foundation. Gnu general public license. <https://www.gnu.org/copyleft/gpl.html>, 2007.
- [Fou14a] Blender Foundation. Blender. <http://www.blender.org/>, 2014.
- [Fou14b] Python Software Foundation. Python. <http://www.python.org/>, 2014.
- [Fre11] E. Freitag. *Complex Analysis 2: Riemann Surfaces, Several Complex Variables, Abelian Functions, Higher Modular Functions*. Universitext. Springer, 2011.
- [GLS07] G. M. Greuel, Ch. Lossen, and E. Shustin. *Introduction to Singularities and Deformations*. Springer-Verlag New York Inc., New York, 2007.
- [GWY04] X. Gu, Y. Wang, and S.-T. Yau. Geometric compression using Riemann surfaces structure. *Communications in information and system*, 3(3):171–182, 2004.
- [HDZ05] G.A. Hansen, R.W. Douglass, and A. Zardecki. *Mesh Enhancement: Selected Elliptic Methods, Foundations and Applications*. World Scientific Publishing Company, Incorporated, 2005.
- [Hla07] J. Hlaváček. Complex domain coloring. [http://www6.svsu.edu/~jhlavace/Complex\\_Domain\\_Coloring/index.html](http://www6.svsu.edu/~jhlavace/Complex_Domain_Coloring/index.html), 2007.
- [HS92] J. Hoschek and G. Seemann. Spherical splines. [http://archive.numdam.org/ARCHIVE/M2AN/M2AN\\_1992\\_\\_26\\_1/M2AN\\_1992\\_\\_26\\_1\\_1\\_0/M2AN\\_1992\\_\\_26\\_1\\_1\\_0.pdf](http://archive.numdam.org/ARCHIVE/M2AN/M2AN_1992__26_1/M2AN_1992__26_1_1_0/M2AN_1992__26_1_1_0.pdf), 1992.
- [JS87] G. A. Jones and D. Singerman. *Complex functions: an algebraic and geometric viewpoint*. Press Syndicate of the University of Cambridge, Great Britain, 1987.
- [KNP07] F. Kalberer, M. Nieser, and K. Polthier. Quadcover - surface parameterization using branched coverings. *Comput. Graph. Forum*, 26(3):375–384, 2007.

- [Kra12] S. Kranich. Real-time visualization of geometric singularities. Master's thesis, Technische Universität München, Department of Mathematics, 2012.
- [Lan99] S. Lang. *Complex Analysis, Fourth Edition*. Springer, New York, USA, 1999.
- [Lun04] H. Lundmark. Visualizing complex analytic functions using domain coloring. [http://www.mai.liu.se/~halun/complex/domain\\_coloring-unicode.html](http://www.mai.liu.se/~halun/complex/domain_coloring-unicode.html), 2004.
- [Mas67] W. S. Massey. *Algebraic Topology: An Introduction*. Harcourt, Brace and World, Inc, New York, 1967.
- [Mul09] T. Mullen. *Mastering Blender*. Sybex, Indianapolis, Indiana, USA, 2009.
- [Nee00] T. Needham. *Visual Complex Analysis*. Oxford University Press Inc., New York, USA, 2000.
- [NPP10] M. Nieser, K. Poelke, and K. Polthier. Automatic generation of Riemann surface meshes. In Bernard Mourrain, Scott Schaefer, and Guoliang Xu, editors, *Advances in Geometric Modeling and Processing*, volume 6130 of *Lecture Notes in Computer Science*, pages 161–178. Springer Berlin / Heidelberg, 2010.
- [OoSU10] F.W.J. Olver, National Institute of Standards, and Technology (U.S.). *NIST Handbook of Mathematical Functions*. Cambridge University Press, 2010.
- [PP09] K. Poelke and K. Polthier. Lifted domain coloring. *Computer Graphics Forum*, 28(3):735–742, 2009.
- [Sha03] B. V. Shabat. Introduction to complex analysis - excerpts. <http://www.math.uchicago.edu/~ryzhik/shabat-all.pdf>, 2003.

- [Sil10] E. L. Da Silva. Reviews of functions of one complex variable graphical representation from software development for learning support. <http://sorzal-df.fc.unesp.br/~edvaldo/imagens.htm>, 2010.
- [Spr57] G. Springer. *Introduction to Riemann surfaces*. Addison-Wesley Publisher Company, Inc., New York, USA, 1957.
- [Tha98] B. Thaller. Visualization of complex functions. *The Mathematica Journal*, 7, 1998.
- [Tro02] M. Trott. Visualization of Riemann surfaces IId. <http://www.mathematica-journal.com/issue/v8i4/columns/trott/contents/RiemannIId.pdf>, 2002.
- [Val10a] M. Valíková. Vizualizácia komplexných funkcií na Riemannovej sfére. In *Geometria a jej aplikácie*, Bratislava, 2010. Slovenská technická univerzita v Bratislave v Nakladateľstve STU v Bratislave. [available online:] <http://www.math.sk/gaja/abstract/2010/proceedings.html>.
- [Val10b] M. Valíková. Základy vizualizácie komplexných funkcií na Riemannovej sfére. *Študentská vedecká konferencia FMFI UK 2010*, pages 52–60, 2010.
- [Val13] M. Valíková. Vizualizácia komplexných funkcií ako lokálnej parametrizácie algebraických kriviek. In *Geometria a jej aplikácie*, Bratislava, 2013. Slovenská technická univerzita v Bratislave v Nakladateľstve STU v Bratislave. [available online:] <http://www.math.sk/gaja/abstract/2013/proceedings.html>.
- [Val14] M. Valíková. CoFiViS. <http://kandy.visitors.sk/cofivis.zip>, 2014.
- [VC10] M. Valíková and P. Chalmovianský. Visualization of complex functions on the Riemann sphere (in slovak). In *Proceedings of Symposium on Computer Geometry SCG 2010*, 19:87–92, 2010.

## REFERENCES

---

- [VC12] M. Valíková and P. Chalmovianský. Visualization of the multivalued complex functions using the Riemann surfaces (in slovak). *In Proceedings of Symposium on Computer Geometry SCG 2012*, 21:120–125, 2012.
- [VC14] M. Valíková and P. Chalmovianský. Visualisation of complex functions on Riemann sphere (article in press). *The Visual Computer*, 2014. DOI = 10.1007/s00371-014-0928-3.
- [Weg10] E. Wegert. Phase diagrams of meromorphic functions. *Computational Methods and Function Theory*, 10(2):639–661, 2010.
- [Weg12] E. Wegert. *Visual Complex Functions: An Introduction with Phase Portraits*. Number 1 in SpringerLink : Bücher. Springer, 2012.
- [WM13] H. Weyl and G.R. MacLane. *The Concept of a Riemann Surface*. Dover Books on Mathematics. Dover Publications, 2013.
- [WS11] E. Wegert and G. Semmler. Phase plots of complex functions: a journey in illustration. *Notices of the Amer. Math. Soc.*, 58:768–781, 2011.
- [YJG07] X. Yin, M. Jin, and X. Gu. Computing shortest cycles using universal covering space. In *The Visual Computer*, volume 23, page 25. Springer-Verlag New York, Inc., 2007.
- [SF04] J. Žára, B. Beneš, J. Sochor, and P. Felkel. *Moderní počítačová grafika, druhé, přepracované a rozšířené vydání*. Computer Press, 2004.